

University of Warwick institutional repository: <http://go.warwick.ac.uk/wrap>

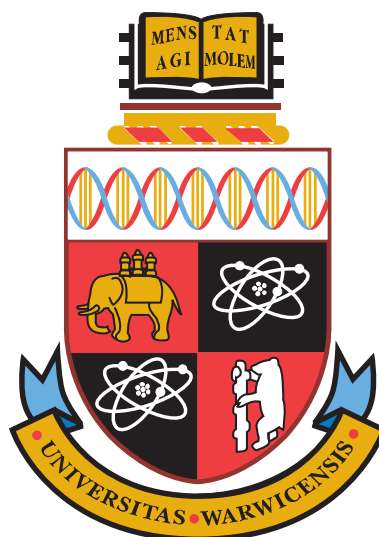
A Thesis Submitted for the Degree of PhD at the University of Warwick

<http://go.warwick.ac.uk/wrap/3184>

This thesis is made available online and is protected by original copyright.

Please scroll down to view the document itself.

Please refer to the repository record for this item for information to help you to cite it. Our policy information is available from the repository home page.



Characterisation of novel antimony (III) oxide-containing glasses

by

Robin George Orman

Thesis

Submitted to the University of Warwick

for the degree of

Doctor of Philosophy

Department of Physics

January 2010

THE UNIVERSITY OF
WARWICK

Contents

Title page	i
Contents	ii
List of Tables	vi
List of Figures	viii
Acknowledgments	xii
Declaration and published work	xiii
Abstract	xiv
Glossary and abbreviations	xv
Chapter 1 An Introduction to Glass	1
1.1 Introduction	1
1.2 Definition and properties	1
1.3 Glass-forming oxides	3
1.4 Simple structural theories of glass formation	3
1.5 Multi-component glasses	5
1.6 Lone-pair cations in glasses	6
1.7 Antimony oxide glasses	7
1.8 Summary	7
References	8
Chapter 2 Literature Review	9
2.1 Antimony oxides	9
2.2 Single-component antimony oxide glass	11
2.3 Antimony oxychloride glass	12
2.4 Antimony borate glasses	15

2.5	Antimony silicate glasses	20
2.6	Summary	22
	References	23
Chapter 3 Experimental Theory and Practice		26
3.1	X-ray diffraction	26
3.2	Energy-dispersive X-ray spectroscopy	28
3.3	Thermal analysis techniques	29
3.4	Raman spectroscopy	31
3.5	Mössbauer spectroscopy	32
3.6	Density measurements	33
3.7	Neutron diffraction	34
3.7.1	Properties of the neutron	34
3.7.2	Neutron scattering theory	36
3.7.2.1	Introduction	36
3.7.2.2	Scattering cross-sections	36
3.7.2.3	Scattering from a single fixed nucleus	37
3.7.2.4	Fermi pseudo-potential	39
3.7.2.5	Total diffraction: elastic scattering	39
3.7.2.6	Total diffraction: coherent and incoherent scattering	40
3.7.2.7	Total diffraction from a disordered sample	41
3.7.3	ISIS: A pulsed neutron source	45
3.7.4	Data analysis	46
3.7.4.1	Extracting the distinct scattering	46
3.7.4.2	The total correlation function	47
3.7.5	Experimental method	48
	References	49
Chapter 4 Antimony Oxide and Oxychloride Glasses		51
4.1	Sample preparation and characterisation	51
4.2	Thermal analysis	54
4.2.1	Antimony oxide glass	54
4.2.2	Antimony oxychloride glass	56

4.3	Density measurements	59
4.4	Neutron diffraction	59
4.4.1	Antimony oxide glass	59
4.4.2	Antimony oxychloride glass	65
4.5	Summary	71
	References	73
Chapter 5	Antimony Borate Glasses	75
5.1	Sample preparation and characterisation	75
5.2	Raman spectroscopy	76
5.3	Density measurements	77
5.4	Neutron diffraction	80
5.4.1	Total correlation functions	80
5.4.2	Peak-fitting	84
5.4.3	Sample compositions and structural trends	89
5.4.4	Simulating the total correlation function	94
5.4.5	Conclusions	97
5.5	Summary	98
	References	100
Chapter 6	Antimony Silicate Glasses	102
6.1	Sample preparation and characterisation	102
6.2	Density measurements	105
6.3	Neutron diffraction	106
6.3.1	Total correlation functions	106
6.3.2	Peak-fitting	109
6.3.3	Sample compositions and structural trends	111
6.3.4	Simulating the total correlation function	117
6.3.5	Conclusions	118
6.4	Summary	118
	References	120
Chapter 7	Conclusions and Future Work	121
7.1	Antimony oxide glass	121

7.2	Antimony oxychloride glass	122
7.3	Antimony borate glasses	122
7.4	Antimony silicate glasses	123
7.5	The behaviour of antimony oxide in a glass network	124
7.6	Future work	125
	References	128

List of Tables

2-1	Sb–O bond lengths in the various structural units found in the crystalline antimony oxides	11
2-2	Densities reported for Sb ₂ O ₃ glass by various authors	13
2-3	Data reported in the literature on two antimony silicate glass samples prepared by a sol-gel method.	21
3-1	Neutron scattering lengths and atomic numbers for the elements present in the samples studied	35
5-1	Measured densities of the antimony borate glasses	78
5-2	B–O values obtained from single-peak fits of $T(r)$ for the antimony borate glasses	85
5-3	B–O values obtained from two-peak fits of $T(r)$ for the antimony borate glasses	87
5-4	B–O two-peak fits of $T(r)$ for the antimony borate glasses using x values from quantitative NMR	87
5-5	Sb–O values obtained from two-peak fits of $T(r)$ for the antimony borate glasses	89
5-6	Comparison of measured Sb–O coordination numbers with two models based on Mössbauer data	90
5-7	Coordination numbers of the nominal $x = 0.6$ antimony borate glass, using x values chosen by ‘trial-and-improvement’ to match the values obtained from NMR	91
6-1	Antimony silicate glass compositions as determined by EDX	103
6-2	Values obtained from peak fits of $T(r)$ for the antimony silicates using nominal compositions	110
6-3	Values obtained from peak fits of $T(r)$ for the antimony silicates using compositions determined from EDX	112

6-4	Values obtained from peak fits of $T(r)$ for the antimony silicates using compositions determined by ‘trial-and-improvement’	113
6-5	Comparison of measured Sb–O coordination numbers with two models based on Mössbauer data	115
7-1	Neutron scattering lengths and atomic numbers for the elements present in the samples studied	127

List of Figures

1-1	An enthalpy vs temperature plot for a glass-forming melt	2
1-2	A schematic comparison the structures of crystals and glasses	5
2-1	The structures of senarmontite, valentinite, cervantite and Sb_2O_5	10
2-2	The Menchetti and Mayerová models of the structure of onoratoite . . .	14
2-3	The basic ladder units of the Menchetti model, with bond lengths	16
2-4	The two types of basic ladder unit of the Mayerová model, with bond lengths	16
2-5	Densities reported for the antimony borate glass system	17
2-6	Values of T_g reported for the antimony borate glass system	18
2-7	Values of N_4 reported for the antimony borate system	19
3-1	The geometry of an X-ray diffractometer	27
3-2	An example of a crystal X-ray diffraction pattern	27
3-3	An example of a glass X-ray diffraction pattern	28
3-4	Example DTA curve with extrapolated T_g and T_c	30
3-5	A schematic diagram of a gas pycnometer	34
3-6	The geometry of a neutron scattering experiment	37
3-7	$I(Q)$ for SiO_2 glass	42
3-8	$T(r)$ for SiO_2 glass	43
3-9	Simulated $T(r)$ compared with a local network structure	44
3-10	The layout of the detector banks in the GEM diffractometer	46
3-11	The flux of neutrons on GEM after moderation at ISIS	47
4-1	The XRD pattern of synthesised crystalline onoratoite, $\text{Sb}_8\text{O}_{11}\text{Cl}_2$. . .	52
4-2	The XRD patterns of the Sb_2O_3 and $\text{Sb}_8\text{O}_{11}\text{Cl}_2$ glasses	53
4-3	Comparison of the polarised Raman spectrum of the Sb_2O_3 glass with those of the crystalline Sb_2O_3 polymorphs	54
4-4	Comparison of the unpolarised oxychloride glass and crystal Raman spectra	55

4-5	TGA/DSC data for the Sb_2O_3 glass under nitrogen	56
4-6	TGA/DSC data for the $\text{Sb}_8\text{O}_{11}\text{Cl}_2$ glass under nitrogen	57
4-7	Comparison of DSC data obtained for the $\text{Sb}_8\text{O}_{11}\text{Cl}_2$ glass and crystal samples under nitrogen	57
4-8	Vitreous Sb_2O_3 $T(r)$ compared with simulated crystalline Sb_2O_3 corre- lation functions	60
4-9	Vitreous Sb_2O_3 $T(r)$ compared with simulated crystalline cervantite correlation functions	62
4-10	Vitreous Sb_2O_3 $T(r)$ compared with simulated crystalline Sb_2O_5 corre- lation functions	62
4-11	The residuals of single- and double-peak fits to the first Sb–O correla- tion for the Sb_2O_3 glass	63
4-12	The neutron $T(r)$ of the onoratoite crystal compared with simulated cor- relation functions from the model of Menchetti <i>et al.</i>	66
4-13	The basic ladder units of the Menchetti model, with bond lengths	66
4-14	The neutron $T(r)$ of the onoratoite crystal compared with simulated cor- relation functions from the model of Mayerová <i>et al.</i>	67
4-15	The neutron $T(r)$ of the $\text{Sb}_8\text{O}_{11}\text{Cl}_2$ glass compared with simulated cor- relation functions from the model of Mayerová <i>et al.</i>	68
4-16	The two types of basic ladder unit in the Mayerová model, with bond lengths	69
4-17	A two-peak fit to the first Sb–O correlation in the antimony oxychloride glass	69
4-18	Comparison of the total correlation functions for the $\text{Sb}_8\text{O}_{11}\text{Cl}_2$ and Sb_2O_3 glasses	71
5-1	The percentage of Sb present as Sb^{5+} in the borate glasses, derived from Mössbauer data	76
5-2	Unpolarised Raman spectra for the antimony borate glasses	78
5-3	Comparison of measured antimony borate densities with literature values	79
5-4	Comparison of measured antimony borate densities with literature val- ues using NMR compositions	79
5-5	$T(r)$ for the antimony borate glasses	81

5-6	$T(r)$ for the antimony borate glasses as a stack plot	81
5-7	Interatomic distances of a $[B_3O_6]$ boroxol group	82
5-8	B–O weighted correlation functions for the antimony borate glasses	84
5-9	Sb–O weighted correlation functions for the antimony borate glasses	85
5-10	The residuals of single- and double-peak fits to the first B–O correlation for the $x = 0.4$ antimony borate sample	86
5-11	The residual of a single-peak fit to the first Sb–O correlation for the $x = 0.7$ antimony borate sample	88
5-12	The total Sb–O coordination numbers for the antimony borate samples	92
5-13	The positions of the Sb–O peaks for the antimony borate samples	93
5-14	The total B–O coordination numbers for the antimony borate samples	94
5-15	The $x = 0.5$ antimony borate $T(r)$ compared with one simulated from ν - B_2O_3 and ν - Sb_2O_3 data	95
5-16	Interatomic distances of a $[B_3O_6]$ boroxol group and an attached $[SbO_3]$ unit	96
5-17	The difference between the experimental and simulated $T(r)$ for the an- timony borate glasses	97
6-1	The XRD pattern of the $x = 0.1$ antimony silicate glass	103
6-2	Values of T_g reported for other, contemporary antimony silicate glass samples	104
6-3	The percentage of Sb present as Sb^{5+} , derived from Mössbauer data of contemporary antimony silicate samples	105
6-4	Measured densities for the antimony silicates plotted against composi- tions determined from neutron diffraction	106
6-5	$T(r)$ for the antimony silicates	107
6-6	$T(r)$ for the antimony silicates as a stack plot	108
6-7	Si–O weighted correlation functions for the antimony silicates	109
6-8	Sb–O weighted correlation functions for the antimony silicates	110
6-9	The residuals of single- and double-peak fits to the first Sb–O correla- tion for the $x = 0.55$ antimony silicate sample	111
6-10	The total Si–O and Sb–O coordination numbers obtained from fitting to the $T(r)$ of the antimony silicate samples	114

6-11	The positions of the Si–O and Sb–O peaks fitted to the $T(r)$ of the antimony silicate samples	115
6-12	The shapes of the first two oxygen-oxygen peaks in the $T(r)$ for the antimony silicate glasses	116
6-13	The $x = 0.3$ antimony silicate $T(r)$ compared with one simulated from ν -SiO ₂ and ν -Sb ₂ O ₃ data	117
7-1	A comparison of the Sb–O and O _{Sb} ···O _{Sb} peaks between the samples with the highest Sb ₂ O ₃ -content in the glass systems studied	125
7-2	The Mayerová model of onoratoite (Sb ₈ O ₁₁ Cl ₂)	126

Acknowledgments

It has been my privilege to meet and work with a lot of very smart people over the course of my PhD and, for making it as enjoyable and rewarding as it has been, I'd like to thank each and every one of them. Unfortunately, after many months of thesis-writing, my brain is quite frazzled and I can thus only give special mention to those whom I can immediately remember.

First and foremost among these is my supervisor, Dr Diane Holland, for her wisdom and patience, and for putting up with me for another four years after guiding me through my master's degree; I couldn't have wished for a better mentor. I am also grateful for all the advice and help I've received from Professor Alex Hannon, during numerous experiments and other visits, without whom my knowledge of neutrons would be a mere fraction of what it is today.

I'd like to thank Professor Mike Thomas at the University of Liverpool for taking the Mössbauer measurements reported in this work, and Professor Steve Feller for hosting my trip to Coe College in 2007. I am grateful to the Warwick Diamond Group for the use of their Raman spectrometer, to Mr Keith Briggs and Mr David Hammond for their technical support in numerous areas, and to Dr Gavin Mountjoy for his assistance with RMC (which I'm convinced will yet bear fruit, if not in time for this thesis). My thanks also to EPSRC for funding my research, and to ASSEC at Warwick for partially funding my trip to the USA.

To Dean, Dan, Martin, Aoife, Ben and Emma, I owe my thanks for sharing an office with me for various lengths of time: without you all, life would've been far less interesting. I am also especially indebted to Emma for her endless patience with my questions on neutron diffraction. Thank you also to my other friends at Warwick, particularly Donna, Phil, Gareth and house mate Andy. I'm also grateful to Jodie for being a calming influence in the lead-up to my viva.

Finally, there's one person who has offered unstinting love and support throughout my time at university, for which I am grateful beyond words, and to whom this thesis is dedicated—thanks, Mum.

Declaration and published work

I declare that the work presented in this thesis is my own except where stated otherwise, and was carried out entirely at the University of Warwick, during the period of September 2005 to November 2009, under the supervision of Dr Diane Holland. The research reported here has not been submitted, either wholly or in part, in this or any other academic institution for admission to a higher degree.

Some parts of the work reported and other work not reported in this thesis have been published, or are in preparation for publication, as listed below. It is anticipated that further parts of this work will be submitted for publication in due course.

- [1] R. G. Orman, D. Holland and A. C. Hannon, “Antimony oxychloride glass and its relation to crystalline onoratoite, $\text{Sb}_8\text{O}_{11}\text{Cl}_2$ ”, *Phys. Chem. Glasses-B* **49** (1), (2008), 15–18.
- [2] M. Mee, B. C. Davies, R. G. Orman, M. F. Thomas and D. Holland, “Antimony and silicon environments in antimony silcate glasses”, (in preparation).
- [3] R. G. Orman, D. Holland and A. C. Hannon, “Preparation and structural characterisation of Sb_2O_3 glass”, (in preparation).
- [4] R. G. Orman, D. Holland and A. C. Hannon, “The structure of Sb_2O_3 – B_2O_3 binary glasses”, (in preparation).
- [5] R. G. Orman, M. Mee, D. Holland and A. C. Hannon, “The structure of Sb_2O_3 – SiO_2 binary glasses: a neutron diffraction study”, (in preparation).



R. G. Orman

January 2010

Abstract

The structures of several glass systems containing the lone-pair cation Sb^{3+} have been studied using a range of techniques, including neutron diffraction, Mössbauer spectroscopy, Raman spectroscopy, energy-dispersive X-ray (EDX) analysis, X-ray diffraction and density measurements. Comparisons with some related crystals have also been used to identify structural features.

An Sb_2O_3 glass was prepared by roller-quenching and found to be both fully amorphous and free of contaminants, using X-ray diffraction and EDX analysis, respectively. A glass transition temperature, T_g , of $250(2)^\circ\text{C}$ and a crystallisation temperature, T_c , of $303(2)^\circ\text{C}$ were measured using differential scanning calorimetry, whilst the density of the glass was found to be $5.27(2)\text{ g cm}^{-3}$. Analysis of the total correlation function $T(r)$ from neutron diffraction of the sample found two distinct peaks at $1.972(1)\text{ \AA}$ and $2.092(4)\text{ \AA}$, with a total Sb–O coordination number of $3.24(4)$, indicating the presence of some $[\text{Sb}^{3+}\text{O}_4]$ and/or $[\text{Sb}^{5+}\text{O}_6]$ units, in addition to the main $[\text{Sb}^{3+}\text{O}_3]$ network. Several models of the local structure are proposed, based on different possible amounts of Sb^{5+} present in the glass.

An antimony oxychloride glass was prepared from crystalline $\text{Sb}_8\text{O}_{11}\text{Cl}_2$ by splat-quenching, and Mössbauer spectroscopy was used to determine that it contained no Sb^{5+} . The thermal events in the system were characterised, with $T_g = 278(2)^\circ\text{C}$ and $T_c = 318(2)^\circ\text{C}$; the density was found to be $5.10(2)\text{ g cm}^{-3}$. Neutron diffraction of the crystal distinguished between two different structural models in the literature, whilst also indicating that the glass may consist of similar chains of $[\text{Sb}^{3+}\text{O}_3]$ and $[\text{Sb}^{3+}\text{O}_4]$ units.

Glasses of nominal composition $x\text{Sb}_2\text{O}_3 \cdot (1-x)\text{B}_2\text{O}_3$ were studied over the range $x = 0.1$ to $x = 0.7$. Raman spectroscopy and neutron diffraction indicated that the glass network consists of significant amounts of $[\text{B}_3\text{O}_6]$ boroxol rings at low x that are cleaved by the introduction of $[\text{Sb}^{3+}\text{O}_3]$ trigonal pyramids. At higher x , there is some evidence for Sb–O–Sb bonding, resulting in the persistence of the boroxol rings to $x \geq 0.7$. Two Sb–O distances were apparent in the $T(r)$, suggesting similar models of the antimony oxide units to those for the Sb_2O_3 glass.

Five antimony silicate glasses of nominal composition $x\text{Sb}_2\text{O}_3 \cdot (1-x)\text{SiO}_2$ were prepared and found by Mössbauer spectroscopy to contain growing amounts of Sb^{5+} with increasing x , up to $9.9(5)\%$ at $x = 0.8$. Density measurements suggested that the SiO_2 and Sb_2O_3 networks mix in the glass without significantly altering each other, and this is supported by comparison of the measured neutron diffraction $T(r)$ with a weighted sum of the total correlation functions of the two system end-members. The simulation also indicated fewer high-coordination antimony oxide units ($[\text{Sb}^{3+}\text{O}_4]$, $[\text{Sb}^{5+}\text{O}_6]$) than in the Sb_2O_3 glass, although two distinct Sb–O distances were once again apparent in the neutron $T(r)$.

The overall conclusion is that Sb_2O_3 forms a glass network consisting predominantly of $[\text{Sb}^{3+}\text{O}_3]$ trigonal pyramids with a stereochemically-active lone-pair, whilst some more highly-coordinated $[\text{Sb}^{3+}\text{O}_4]$ and $[\text{Sb}^{5+}\text{O}_6]$ units may also be present.

Glossary and abbreviations

DSC	Differential scanning calorimetry
DTA	Differential thermal analysis
EDX	Energy dispersive X-ray (spectroscopy)
EXAFS	Extended X-ray absorption fine structure
FCC	Face-centred cubic
FWHM	Full width at half maximum
IR	Infra-red
MAS NMR	Magic angle spinning nuclear magnetic resonance
N_4	The fraction of boron units that are four-coordinated
NMR	Nuclear magnetic resonance
NNO	Next-nearest oxygen
Q^n	$[\text{SiO}_4]$ tetrahedra with n non-bridging oxygen atoms
RMC	Reverse Monte Carlo (modelling)
SEM	Scanning electron microscope
TGA	Thermogravimetric analysis
T_c	Crystallisation temperature
T_g	Glass transition temperature
$T(r)$	Total correlation function
$t_{ll'}(r)$	Partial correlation function between atoms l and l'
VSEPR	Valence shell electron pair repulsion
XRD	X-ray diffraction

Chapter 1

An Introduction to Glass

1.1 Introduction

Glass has been used by humans since the Stone Age. Obsidian—a natural glass formed from the cooling of silica-rich lava—can be fractured like flint to form extremely sharp edges, a property that was exploited for use in arrowheads and simple cutting tools. The earliest known man-made glasses originated in Egypt and Eastern Mesopotamia circa 3500 B.C. in the form of glass beads (possibly an unintended by-product of other industry) and by c. 1500 B.C. craftsmen were able to produce glass pots and other vessels. The Romans later spread glass-making technology throughout Western Europe and around the Mediterranean, and the use of glass for practical, artistic and architectural purposes grew and developed during the Middle Ages and the Renaissance.

It was not until the late 19th century, however, that scientific studies to relate the properties of a glass to its composition began in earnest; the effects of certain additives—such as oxides of magnesium, calcium and lead—had been known of for centuries, but were discovered empirically. Modern scientific interest in glass includes its applications in the field of laser optics and in the storage of nuclear waste.

1.2 Definition and properties

Silica, in the form of sand, is commonly regarded as a prerequisite for glass-making and many SiO_2 -based glasses do exist; it is not, however, an essential component of a glass. In fact, a diverse array of chemical substances can be vitrified; materials are instead characterised as a glass based on their properties, rather than their composition. A solid is generally classed as a glass if it meets two criteria: it has no long-range order in its atomic arrangement, and it experiences a ‘glass transformation region’ (a time-dependent behaviour over a temperature range).

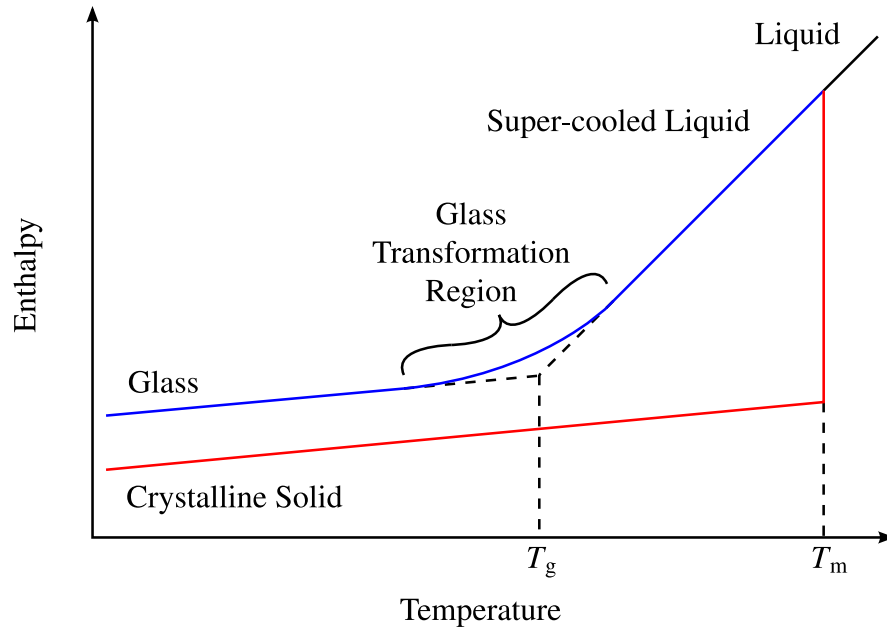


Figure 1-1 Thermodynamic diagram showing the changes in enthalpy of a glass-forming melt with temperature (blue line), as opposed to that of a normal liquid-solid transition (red line).

Consider a liquid at a temperature above its melting point (Fig. 1-1). As the temperature is lowered, the enthalpy of the substance will gradually decrease and its atomic arrangement will slowly change, being at any point characteristic of the temperature of the melt. When the liquid is cooled below its melting point T_m it will usually experience an abrupt shift to a crystalline solid (with long-range atomic order) with a correspondingly sharp decrease in enthalpy.

However, if the liquid can be cooled below the melting point without crystallisation ('super-cooled') it will continue to exhibit a gradual decrease in enthalpy with temperature. As cooling progresses, the viscosity of the liquid will increase; at some point the viscosity will be such that the atomic structure of the liquid will be unable to realign to the equilibrium arrangement for its temperature in the time available. This will cause the enthalpy of the system to lag from the equilibrium line until the point is reached where the viscosity prevents *any* further atomic rearrangement. In essence, the liquid has become an amorphous solid with no long-range order—one of the conditions necessary for a material to be considered as a glass. In addition, the process of super-cooling has also fulfilled the second requirement: the temperature region that lies between the enthalpy being that of the equilibrium liquid and that of the frozen liquid is what is known as the *glass transformation region*.

As indicated in Figure 1-1, the glass transformation region exists over a range of temperatures. However, it is often useful to define a single *glass transition temperature*, T_g , as an indication of the onset of the glass transformation region upon heating the glass. This is defined empirically, and the value obtained for a given glass is dependent on several factors, including the rate at which the melt was originally cooled, the experimental method used to determine T_g and the heating rate applied. Hence, T_g should not be considered a true thermodynamic property, but is a useful indicator of when the transition between glass and supercooled liquid occurs. Another temperature often quoted is the *crystallisation temperature*, T_c , which occurs after T_g and indicates the onset of crystallisation of the devitrified material. The difference in magnitude between T_g and T_c can also be used as an indicator of the stability of the glass.

Finally, it should be noted that, whilst cooling of a melt is the most common method of glass-making, it is by no means the only way of doing so: chemical vapour deposition and sol-gel processing are examples of other such techniques.

1.3 Glass-forming oxides

Silica (SiO_2) is one of a series of oxides known as *glass-formers* (or *network-formers*) that will readily form glasses in isolation—other examples are B_2O_3 , GeO_2 and P_2O_5 . The cations in these oxides tend to form highly covalent bonds with oxygen, which has been shown to be a common property of glass-formers. Oxides with cations whose oxygen bonding is more ionic in nature—such as SeO_2 , WO_3 and Al_2O_3 —will not form a glass individually, but will do so when melted with a suitable quantity of a second oxide; these are termed *intermediates* or *conditional glass-formers*. Finally, oxides with highly ionic bonds never form a glass, but can be used to affect the glass structure created from other glass-formers—these oxides are known as *modifiers*.

1.4 Simple structural theories of glass formation

Different chemical systems require specific cooling rates to be met or exceeded in order to form glasses. This fact has led to several attempts to produce a complete atomic theory of glass formation based on the nature of the chemical bonds and the shape of

the structural units involved. Whilst it may seem strange to propose structural theories for a substance that is defined as having ‘no long-range, periodic atomic ordering’, it has been found to be possible to form reproducibly the same glass from a nominal starting composition, implying that there is some short-range ordering that is sufficient to control the overall properties.

In 1926, Goldschmidt presented a theory of glass formation for the general A_2O_3 system based on the empirical observation that these most readily formed glasses when the cation-oxygen radius ratio was between 0.2 and 0.4 [1]. Since values in this range tend to produce cations surrounded by oxygen atoms in a tetrahedral arrangement, Goldschmidt posited that this atomic structuring was most favourable for glass formation. However, this theory has been subsequently shown to be incomplete, with a variety of systems inadequately explained by it.

Six years later, Zachariasen [2] extended Goldschmidt’s ideas and produced perhaps the most cited paper in glass science. Zachariasen noted that silicate crystals, which readily form glasses, have network structures instead of the close-packed tetrahedral arrangement described by Goldschmidt. By postulating that the oxygen polyhedra found in the oxide crystals would also be present in the glasses, Zachariasen formed the concept of a continuous network structure for a glass, with periodic structural arrangement prevented by random orientations. These can be achieved by variations in bond angles and bond lengths, or by rotation of structural units (Fig. 1-2).

Zachariasen also proposed a set of rules to allow for this structure:

1. No oxygen atom must be linked to more than two cations.
2. The number of oxygen atoms surrounding any given cation must be small (typically three or four).
3. Oxygen polyhedra only share corners, not edges or faces.
4. At least three corners of each oxygen polyhedron must be shared (this ensures that the network will be three-dimensional).

Although some exceptions to these rules do exist (for example, certain glasses can occur in two-dimensional structures), they have nevertheless formed the basis for most widely-used models of glass structure.

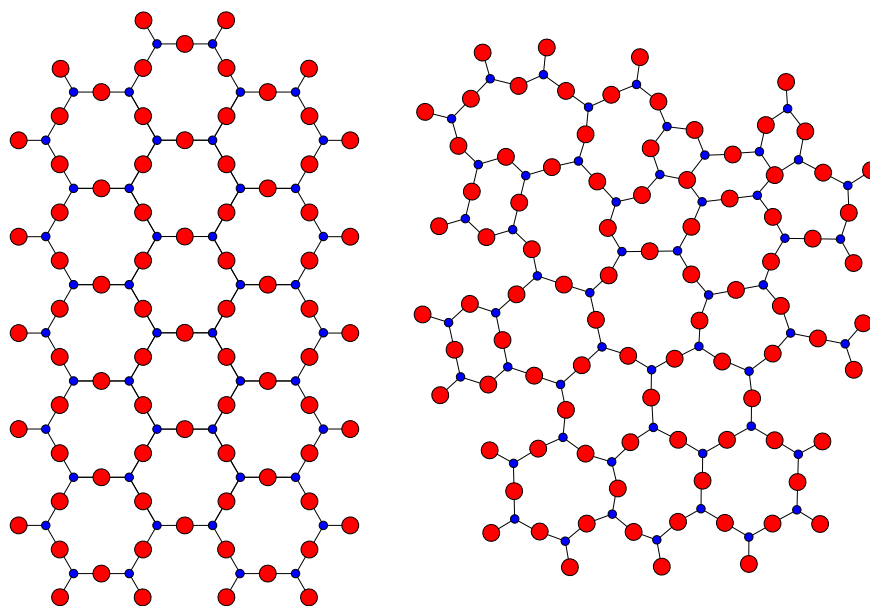


Figure 1-2 A schematic 2D representation of (a) a generic A_2O_3 crystalline compound and (b) a continuous random network of the same substance [3].

1.5 Multi-component glasses

Whilst some substances form vitreous systems with relative ease (e.g. B_2O_3 , P_2O_5), other, poorer glass-formers (e.g. As_2O_3) require more extreme cooling rates for this to occur. As detailed above, glass structural theories require the formation of a continuous random network of atoms, as opposed to the ordered, repeating atomic arrangement in a crystal lattice—this can be made to occur more readily in poor glass-formers by adding a small amount of a contaminant.

In terms of enthalpy, glasses are thermodynamically less-favourable than the available crystalline modifications (*q.v.* Fig. 1-1): however, their random structures are more entropic. The trade-off between reducing the enthalpy and decreasing the entropy during crystallisation is prevented by kinetic factors: once a supercooled liquid drops below T_g the activation energy necessary to re-form the structure is no longer present, and the atoms become locked in an amorphous arrangement. The ease with which a melt forms a crystal lattice is also affected by kinetics, since crystals form by a process of nucleation and growth.

The introduction of a contaminant increases the overall entropy of the system—making it somewhat less thermodynamically favourable to form a crystal structure—and hinders the kinetic realignment by providing more bonds to break and atoms to

rearrange, frustrating crystal formation. Thus, the presence of a contaminant in a melt can substantially improve the glass-forming ability of a system.

However, such impurities can also play a significant role in the properties of the glass formed. This is an important factor since not all contamination is intentional: for example, a melt may react with a certain crucible material and thus introduce impurities to the resultant glass. Another common contaminant is water which is difficult to regulate between preparations and can form hydroxyl groups in the glass structure.

Glass melts are cooled by a variety of techniques, depending on the glass to be formed and its stability; less stable glasses require more extreme cooling techniques. Splat-quenching (pressing the melt between two cooled metal plates), roller-quenching (pouring the melt between two counter-rotating cylinders) and melt-spinning (forcing a thin stream of melt onto a roller to quench, with the aid of high-pressure gas) are some examples, and offer cooling rates of the order of 10^3 , 10^5 and 10^8 °C s⁻¹, respectively.

1.6 Lone-pair cations in glasses

Cations with a *lone-pair* of electrons—that is, a pair of valence electrons that are more strongly bound to the nucleus and as such do not bond as easily with other atoms—have been associated with non-linear optical properties in glasses [4, 5]. Lone-pairs have a strong steric influence that can alter the long-range structure of a material, resulting in voids due to the volume excluded by the electron pair. However, the relationship between the effects of the lone-pair on the medium-range structure and the non-linear optical properties observed in the glass are not well understood.

The lone-pair influences the spatial arrangement of atoms in a molecule in a similar manner to a bonding-pair of electrons, although a model where the two are treated equivalently, such as that of Sidgwick and Powell [6], does not account for the bond angles observed in many lone-pair molecules, such as H₂O [7]. Gillespie and Nyholm [7] instead proposed a different model, where two bonding-pairs repelled each other less than a lone-pair and a bonding-pair, which in turn experienced less repulsion than two lone-pairs. This theory resulted in more accurate predictions of molecular bond angles, and with further refinement resulted in the Valence Shell Electron Pair Repulsion (VSEPR) model [8, 9].

1.7 Antimony oxide glasses

Antimony trioxide (Sb_2O_3) was predicted to be a glass-former by Zachariasen [2] and contains the lone-pair cation Sb^{3+} (antimony can also occur in the oxidation state Sb^{5+}). Whilst it has proven difficult to form $\nu\text{-Sb}_2\text{O}_3$ without the presence of a contaminant (*q.v.* §2.2), antimony trioxide readily forms a glass with only a few mol% of another oxide. The structural role of the Sb_2O_3 in such glasses is not well-understood.

This work will examine $\nu\text{-Sb}_2\text{O}_3$, an antimony oxychloride glass, and the antimony borate and silicate glass systems, with the aim of characterising the structural behaviour of antimony trioxide in a glass network. Neutron diffraction will be the primary tool used for this study, with other complementary techniques providing supporting data.

1.8 Summary

A glass can be considered as the result of lowering the temperature of a supercooled liquid to the point at which it becomes too viscous to reach an equilibrium state for its temperature; in other words, at the point where the energy of the system is insufficient to allow a thermodynamically favourable drop in enthalpy to occur kinetically. The resulting amorphous structure can be modelled as a continuous random network, with no long-range periodic ordering, although short-range atomic alignments characteristic of the material still exist and regulate the properties of the glass.

The ability of a substance to form a glass, either in isolation or when mixed with another compound, allows it to be classified as a glass-former, intermediate or modifier. The ease with which a glass-former can be used to create a vitreous system can be improved by the addition of one or more modifiers (or contaminants), although this can also affect the properties of the resultant glass.

The lone-pair of electrons on certain cations can exert a strong steric influence that affects the structure of a material and, in the case of a glass, can lead to interesting properties. Antimony trioxide contains such lone-pair cations and has been reported to readily form a glass in combination with another oxide. This work will use neutron diffraction and other methods to investigate several Sb_2O_3 -based glasses, with the aim of characterising the behaviour of Sb_2O_3 in a glass network.

References

- [1] V. M. Goldschmidt, *Vid. Akad. Skr. Oslo* **8**, (1926), 137–???
- [2] W. H. Zachariasen, *J. Am. Chem. Soc.* **54** (10), (1932), 3841–3851.
- [3] A. Paul, *Chemistry of Glasses* (Chapman & Hall, New York, 1990).
- [4] S. R. Friberg and P. W. Smith, *IEEE J. Quantum Elect.* **23** (12), (1987), 2089–2094.
- [5] D. W. Hall, M. A. Newhouse, N. F. Borrelli, W. H. Dumbaugh and D. L. Weidman, *Appl. Phys. Lett.* **54** (14), (1989), 1293–1295.
- [6] N. V. Sidgwick and H. M. Powell, *P. Roy. Soc. Lond. A Mat.* **176** (965), (1940), 153–180.
- [7] R. J. Gillespie and R. S. Nyholm, *Q. Rev. Chem. Soc.* **11**, (1957), 339–380.
- [8] R. J. Gillespie and I. Hargittai, *The VSEPR Model of Molecular Geometry* (Prentice Hall International, London, 1991).
- [9] R. J. Gillespie, *Chem. Soc. Rev.* **21** (1), (1992), 59–69.

Chapter 2

Literature Review

2.1 Antimony oxides

Antimony oxide exists in several forms, including antimony trioxide (Sb_2O_3), antimony tetroxide (Sb_2O_4) and antimony pentoxide (Sb_2O_5). Of these, Sb_2O_3 occurs as cubic and orthorhombic polymorphs (*senarmontite* and *valentinite*, respectively), with the latter being the stable form at higher temperatures, whilst Sb_2O_4 can be monoclinic (*clinocervantite*) or, more commonly, orthorhombic (*cervantite*), and Sb_2O_5 has only been reported to have a single, monoclinic structure [1]. Antimony tetroxide is a mixed valency compound, containing both Sb^{3+} and Sb^{5+} ions in equal proportions in its crystal lattice [2].

It is worth noting that the ‘molecular’ structure of *senarmontite* [3] (Fig. 2-1a) does not appear to lend itself to glass formation when compared with the ‘double-chain’ structure of *valentinite* [4] (Fig. 2-1b) which can be expected to form the ‘continuous random network’ outlined by Zachariasen [5] (q.v. §1.4) with greater ease. The structure of Sb_2O_4 (in both polymorphs) is one of alternating layers of $[\text{Sb}^{3+}\text{O}_4]$ pseudo-trigonal bipyramids and $[\text{Sb}^{5+}\text{O}_6]$ octahedra [6, 7] (Fig. 2-1c), whilst Sb_2O_5 consists entirely of the latter [1] (Fig. 2-1d). The bond lengths reported for the crystalline antimony oxide units are given in Table 2-1: of particular note is that the $[\text{Sb}^{3+}\text{O}_4]$ units in *cervantite* have a 2+2 configuration, where the ‘axial’ bonds are longer than the ‘equatorial’ ones, due to the influence of the lone-pair. The $[\text{Sb}^{5+}\text{O}_6]$ octahedra in *cervantite* also have longer axial bonds, whilst those in Sb_2O_5 have the three shortest bonds form one face of the octahedron.

The thermal phase transitions in the crystalline antimony oxides have been reasonably well-studied, although there have been some conflicting reports in the literature. In particular, the exact temperature of the *senarmontite*-*valentinite* transition has been the subject of numerous studies [2, 10–14], with values ranging from 556 °C [15] to

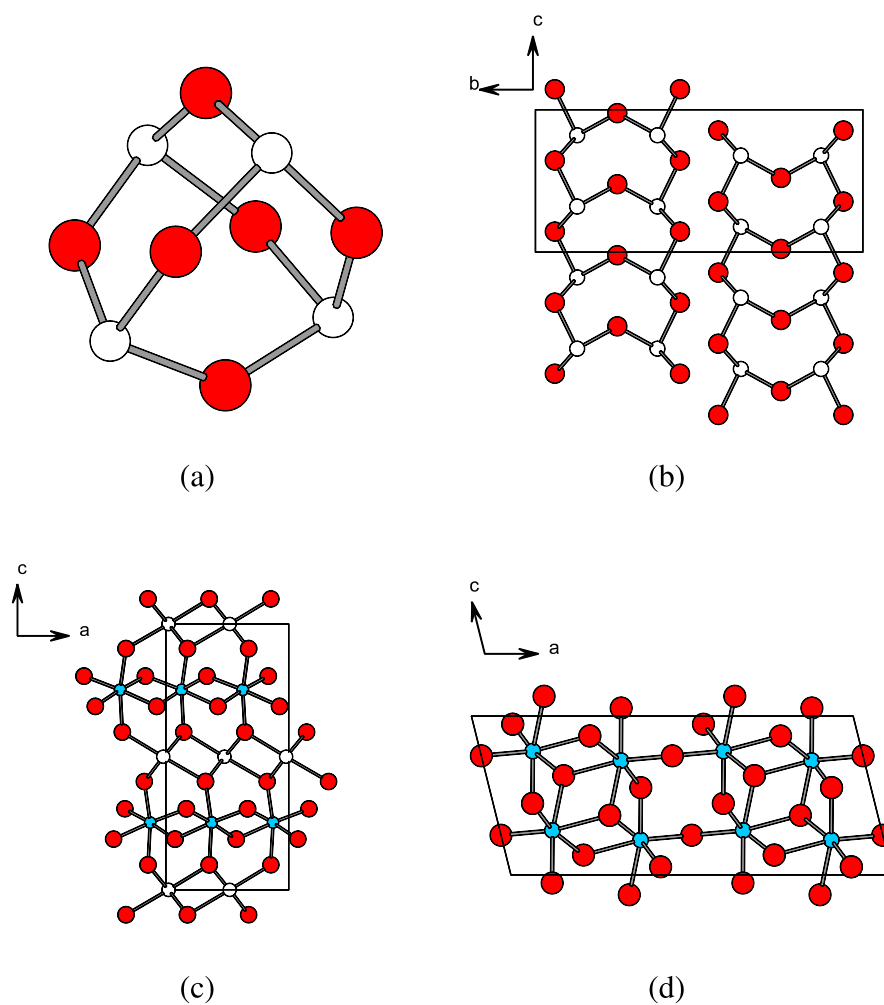


Figure 2-1 The structures of: (a) senarmontite, where the $[\text{Sb}_4\text{O}_6]$ groups shown form a FCC arrangement in the unit cell [3]; (b) valentinite, viewed down the a -axis [4]; (c) cervantite, viewed down the b -axis [6, 7]; and, (d) Sb_2O_5 , also viewed down the b -axis [1]. Oxygen atoms are red, Sb^{3+} are white and Sb^{5+} are cyan.

Table 2-1 Sb–O bond lengths in the various structural units found in the crystalline antimony oxides [1, 3, 4, 7]. Bond-valence calculations give distances of 1.973 Å and 2.079 Å for three- and four-coordinated Sb^{3+} respectively, and 2.009 Å for six-coordinated Sb^{5+} [8, 9].

Antimony oxide	Structural unit	Bond length (Å) & Count
Senarmontite	$[\text{Sb}^{3+}\text{O}_3]$	1.98 (×3)
Valentinite	$[\text{Sb}^{3+}\text{O}_3]$	1.98 (×1) 2.02 (×2)
Cervantite	$[\text{Sb}^{3+}\text{O}_4]$	2.02 (×1) 2.05 (×1) 2.19 (×1) 2.24 (×1)
	$[\text{Sb}^{5+}\text{O}_6]$	1.93 (×1) 1.95 (×1) 1.97 (×2) 1.98 (×1) 2.04 (×1)
Sb_2O_5	$[\text{Sb}^{5+}\text{O}_6]$	1.89 (×1) 1.91 (×2) 2.04 (×1) 2.08 (×1) 2.10 (×1)

655 °C [16]; similar discrepancies can be found for the two oxidation temperatures [12, 13, 17, 18]. A recent work that attempted to address these issues determined the polymorph transition to occur at 643(3) °C [19, 20], although this could be depressed under certain circumstances (it was hypothesised that this could occur due to surface- or bulk-bound water), whilst the reverse transition has been reported as occurring at 600 °C [16]. Senarmontite and valentinite oxidise to form cervantite at 532(3) °C and 410(3) °C, respectively, whilst the melting point of Sb_2O_3 is 652(3) °C [16, 19, 20]. Sb_2O_4 is stable to around 1000 °C [13], the exact value depending upon atmosphere and the method of sample preparation [18].

2.2 Single-component antimony oxide glass

Antimony trioxide was predicted to be a glass-former by Zachariasen in 1932 [5]. In the intervening period, several binary and ternary Sb_2O_3 -based glasses have been studied, including various oxide [21–25] and halide [26–28] systems, and numerous attempts

have been made to form single-component antimony oxide glasses [22, 23, 29–34]. However, these latter efforts have failed to provide conclusive evidence for such a glass, with several methods of glass preparation prone to the introduction of contaminants during melting—principally silica [31, 33] as determined by several authors [26, 32, 34]. Kordes [29] reported preparing an antimony oxide glass by quenching the melt from a platinum crucible, although no further details are given, and this seems unlikely since Masuda *et al.* [23] failed to obtain any pure Sb_2O_3 glass in their study, whilst Hasegawa *et al.* [22] found it necessary to deliberately introduce a small quantity of B_2O_3 to stabilise the material.

The ‘single-component’ Sb_2O_3 glasses prepared to date have generally been determined to possess a structure most similar to that of valentinite [21, 22, 32, 34], the high-temperature crystalline polymorph: for example, Hasegawa *et al.* [22] used X-ray diffraction analysis to obtain an Sb–O interatomic distance of 1.99 Å, an Sb–O coordination of 3.15 and an Sb...Sb distance of 2.8 Å. In addition, a few investigations have also suggested structures based on senarmontite [30] and even vitreous As_2O_3 [33]. Studies of the thermal behaviour of these glasses have generally not been carried out, although Bednarik and Neely [35] obtained T_g and T_c values of 245 °C and 296 °C, respectively, for their silica-contaminated glass using differential scanning calorimetry. Densities reported for various attempted Sb_2O_3 glasses are shown in Table 2-2.

2.3 Antimony oxychloride glass

Whilst investigating Sb_2O_3 – ZnCl_2 glasses, Johnson *et al.* [27, 28] attempted to form an antimony oxychloride glass from 50 mol% Sb_2O_3 and 50 mol% SbCl_3 —however, no chlorine could initially be detected in the resultant glass. Further work by Hannon and Holland [36] has suggested that approximately 8 at.% of the contaminant remained within the glass structure. Orman [19] investigated this chlorine-stabilised glass further, determining that melts of composition $x \text{Sb}_2\text{O}_3 \cdot (1 - x) \text{SbCl}_3$ with $x = 0.5, 0.7$ and 0.85 produced glasses of approximately the same chlorine content, and concluded from thermal and Raman data that the glass structure was similar to that of crystalline *onoratoite*, $\text{Sb}_8\text{O}_{11}\text{Cl}_2$, the structure of which was first reported by Sgarlata [37]. Onoratoite is the only antimony oxychloride that occurs naturally as a mineral; its discovery

Table 2-2 Densities reported for Sb_2O_3 glass by various authors [22, 27, 29, 31, 32]. Also shown are densities for the crystalline Sb_2O_3 polymorphs, senarmontite and valentinite, calculated from crystal structure data [3, 4].

Material	Reference	Density (g cm^{-3})	Notes
Amorphous Sb_2O_3	Kordes [29]	5.179	—
Amorphous Sb_2O_3	Hasegawa <i>et al.</i> [22]	5.07	Made with 5 mol% B_2O_3 .
Amorphous Sb_2O_3	Kutsenko <i>et al.</i> [31]	5.06	Probably contained SiO_2 .
Amorphous Sb_2O_3	Bednarik and Neely [32]	5.105	Contained 1.8 wt.% SiO_2 .
Amorphous Sb_2O_3	Johnson <i>et al.</i> [27]	5.05	Contained 6(2) at.% chlorine [19].
Senarmontite	Svensson [3]	5.5843	Calculated from the crystal structure.
Valentinite	Svensson [4]	5.8447	Calculated from the crystal structure.

was originally announced in 1968 by Belluomini *et al.* [38].

Following a single crystal X-ray diffraction (XRD) study, Menchetti *et al.* [39] proposed a structural model consisting of Sb–O tubes (based on a repeating ladder structure) arranged in layers with the chlorine atoms sandwiched in-between (Fig. 2-2a). This model required four of the six oxygen sites to have a partial occupancy and incorporated unusually long Sb...Cl distances (3.2 Å to 3.8 Å) compared to similar materials (e.g. in SbCl_3 , Sb...Cl is 2.34 Å to 2.37 Å [40]), although a degree of elongation of the Sb...Cl bond is not uncommon in some models of other antimony oxychlorides (2.9 Å in $\text{Sb}_4\text{O}_5\text{Cl}_2$ [41] and 3.0 Å in $\text{Sb}_3\text{O}_4\text{Cl}$ [42]). Mayerová *et al.* [43] later conducted a separate single-crystal XRD study and concluded that the earlier model was a simplification of a more complicated structure. The new model proposed by Mayerová (Fig. 2-2b) consists of forty-two structurally unique atomic positions that resolved the oxygen disorder from the Menchetti model and reduced the range of Sb...Cl distances to between 2.95 Å and 3.20 Å.

Although both models of onoratoite are based on ‘ladder-like’ chains of antimony and oxygen atoms, the ‘ladder’ structures employed by the two models differ slightly:

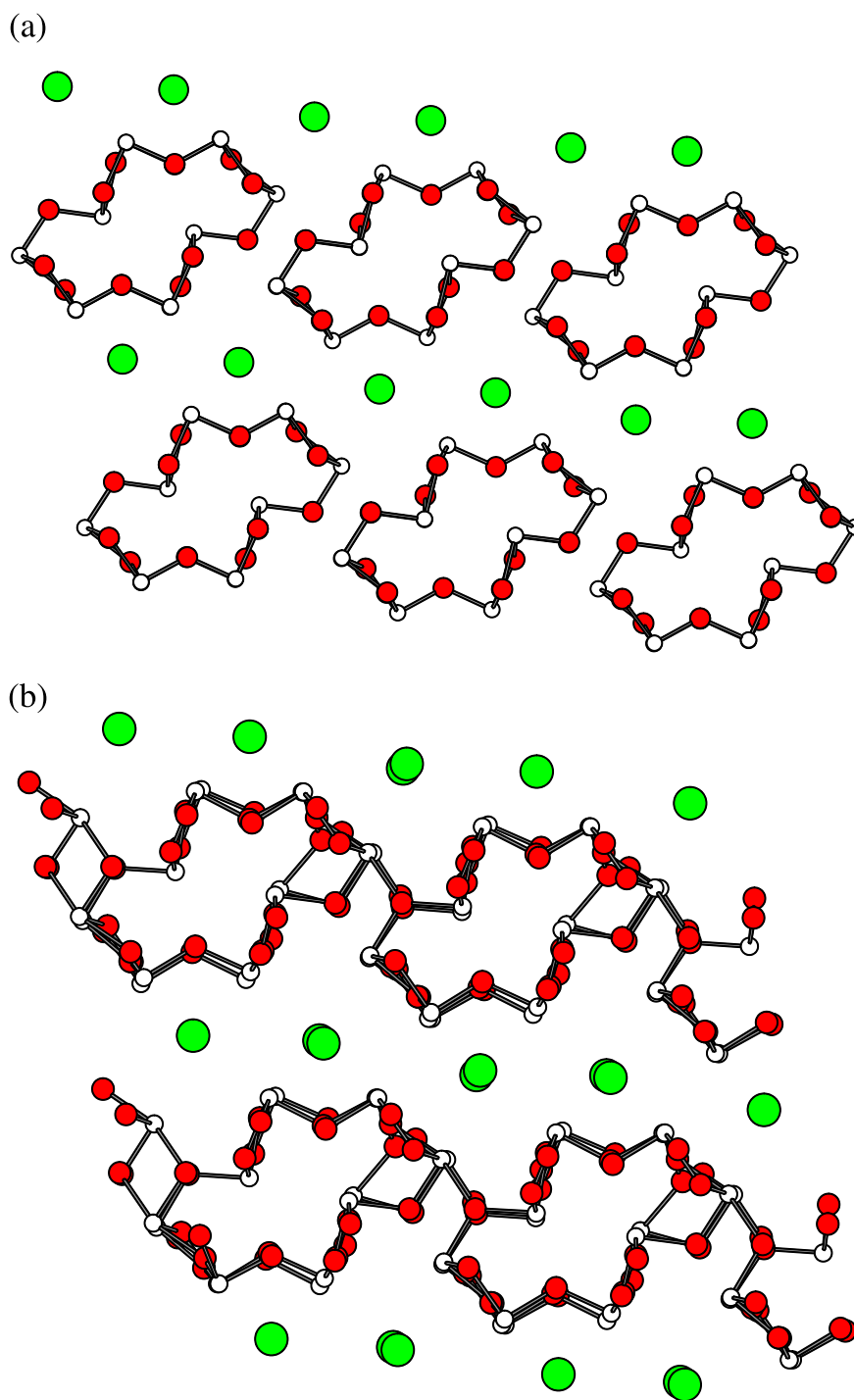


Figure 2-2 The (a) Menchetti [39] and (b) Mayerová [43] models of the structure of crystalline onoratoite. The Menchetti model is viewed down the *b*-axis, whilst the orientation of the Mayerová structure is chosen to aid the comparison. Oxygen atoms are red, chlorine atoms are green, antimony are white. The ‘tubes’ in each model are formed from four, edge-linked ‘ladders’ that extend into the page.

Menchetti *et al.* proposed two very similar chains of infinitely repeating $[\text{SbO}_4]$ units, where each antimony atom is bonded to three oxygen atoms within the chain and one linking to an adjacent ladder (Fig. 2-3), whilst the model proposed by Mayerová *et al.* features two more distinct ladders that consist of smaller numbers of $[\text{SbO}_4]$ groups connected by either two $[\text{SbO}_3]$ units (Fig. 2-4a) or one $[\text{SbO}_3]$ and one $[\text{SbO}_4]$ group (Fig. 2-4b). Both sets have structural peculiarities: the oxygen sites along the ‘rungs’ of the Menchetti ladders are only partially occupied (ranging from 72(3) % to 89(3) % occupancy), resulting in some $[\text{SbO}_3]$ units along the ladder, whilst there are quite a wide range of Sb–O bond lengths in the Mayerová model, to the extent that some of the ‘ $[\text{SbO}_4]$ ’ groups might be more accurately described as $[\text{SbO}_3]$ units with a fourth coordinating oxygen at much greater r (i.e. a 3+1 arrangement; some of the longer Sb–O bonds are highlighted in Figure 2-4). Allowing for the partially occupied oxygen sites in the Menchetti model and treating all of the antimony atoms in the Mayerová model to be coordinated as originally reported [43], the two structural models result in different ratios of four-coordinated to three-coordinated antimony (5:3 and 11:5 in the Menchetti and Mayerová models, respectively)—this may be useful to distinguish between the two possible structures from neutron diffraction data.

Regardless of which model is more accurate, the structure of onoratoite appears to be quite complex, and considerably more ordered than could be expected from a vitreous system. Therefore, it seems likely that if the antimony oxychloride glass does bear structural similarities to onoratoite, these are probably in terms of the types and relative quantities of the various antimony oxide units. It is also conceivable that the ladder-like chains of the two models persist, since either type would appear to lend themselves to producing a disordered network.

2.4 Antimony borate glasses

The antimony borate glass system has been the subject of several studies in the literature, with $x\text{Sb}_2\text{O}_3 \cdot (1-x)\text{B}_2\text{O}_3$ glasses reported to form across the entire compositional range (although note the discussion in §2.2 for $x = 1.0$). This makes the system a desirable one to exploit for non-linear optical applications.

Numerous authors have reported methods of preparing antimony borate glasses [21,

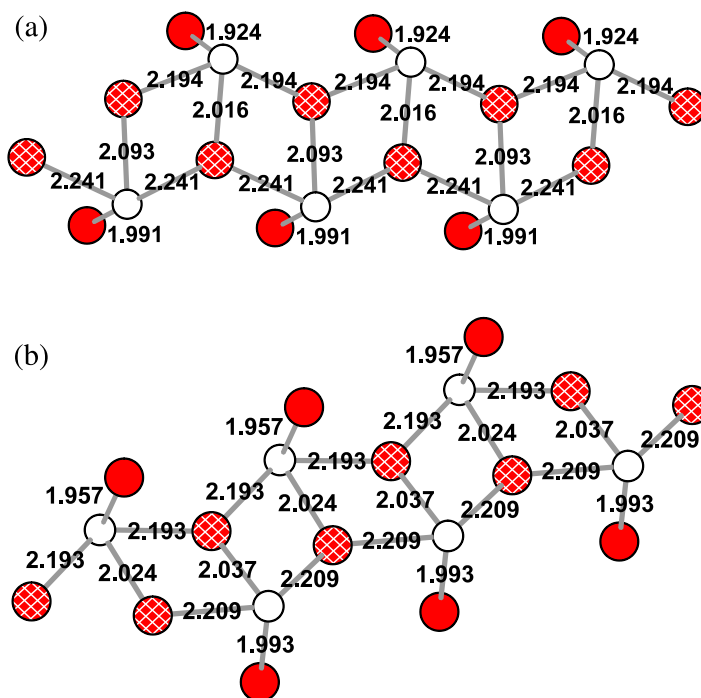


Figure 2-3 The two basic 'ladder' units of the Menchetti model [39]. Oxygen atoms are red, antimony atoms are white. Partially occupied oxygen sites are indicated by white cross-hatching. Sb–O bond lengths are also shown.

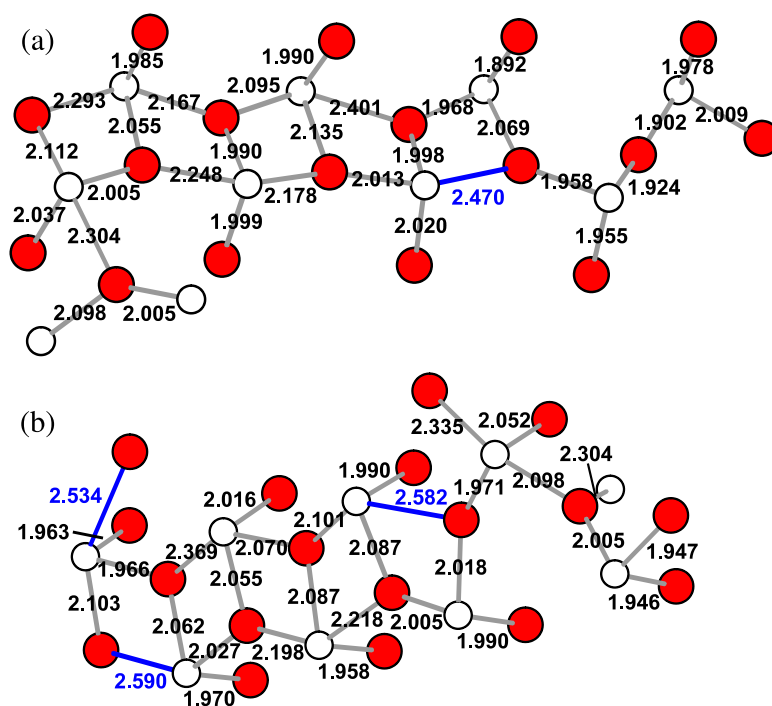


Figure 2-4 The two types of basic 'ladder' unit in the Mayerová model [43]: (a) the ladder is interrupted by two $[\text{SbO}_3]$ groups; (b) the ladder is bridged by one $[\text{SbO}_3]$ and one $[\text{SbO}_4]$ group. Oxygen atoms are red, antimony atoms are white. Sb–O bond lengths are also shown: the four bonds highlighted in blue are those longer than 2.45 Å.

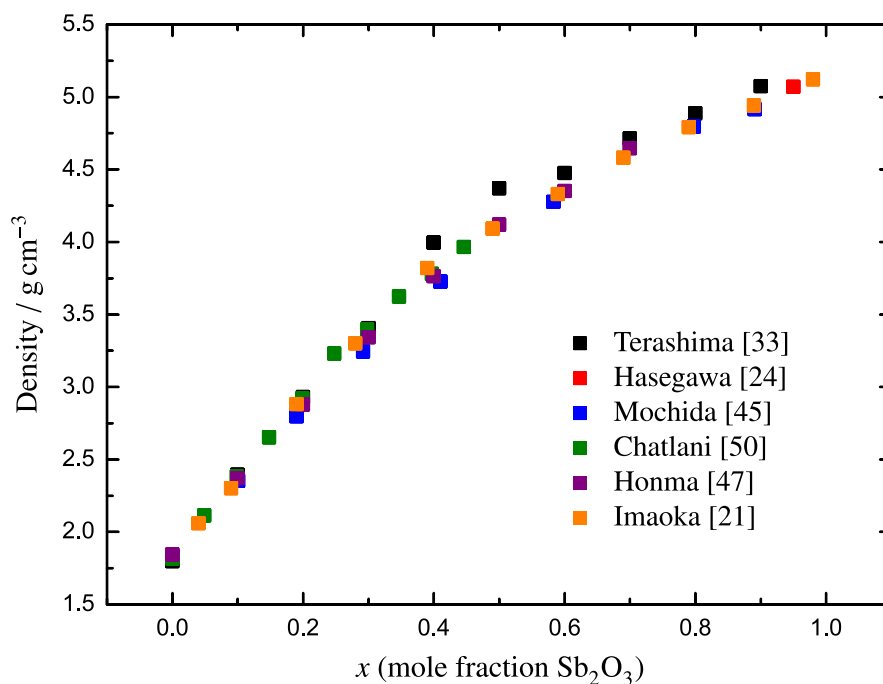


Figure 2-5 The densities reported for the antimony borate glass system, by various authors [21, 22, 34, 44, 45, 50].

22, 34, 44–50]: these typically involve melting at $\sim 800^\circ\text{C}$ in silica or platinum crucibles for ~ 20 minutes before splat-quenching between steel or copper plates; some authors report using higher temperatures [34, 48, 49], or less extreme quenching methods [45, 46]. Youngman *et al.* [48] report SiO_2 contamination which they attribute to the silica crucibles used for the melt—it seems likely that this is also the case for the other authors who reported SiO_2 content [44] or who used such crucibles [47].

There is a general consistency in the densities that have been reported for the various antimony borate glasses (Fig. 2-5)—the only notable exceptions are some of the values reported by Terashima *et al.* [34]. In that work, only the nominal batch compositions are listed for the samples, and so the discrepancies may be due to the quenched glasses having slightly different compositions.

The glass transformation temperatures exhibit much greater disagreement (Fig. 2-6). From the majority of the results reported, there appears to be a maximum T_g at $x \approx 0.3$, although the data of Holland *et al.* [49] appears to indicate that a value at significantly higher x would be appropriate. Nevertheless, the error range reported would include a curve of similar shape to the other authors, suggesting that the data is insufficiently accurate to draw conclusions as to a maximum in T_g . The value of T_g for $x = 0.7$ reported

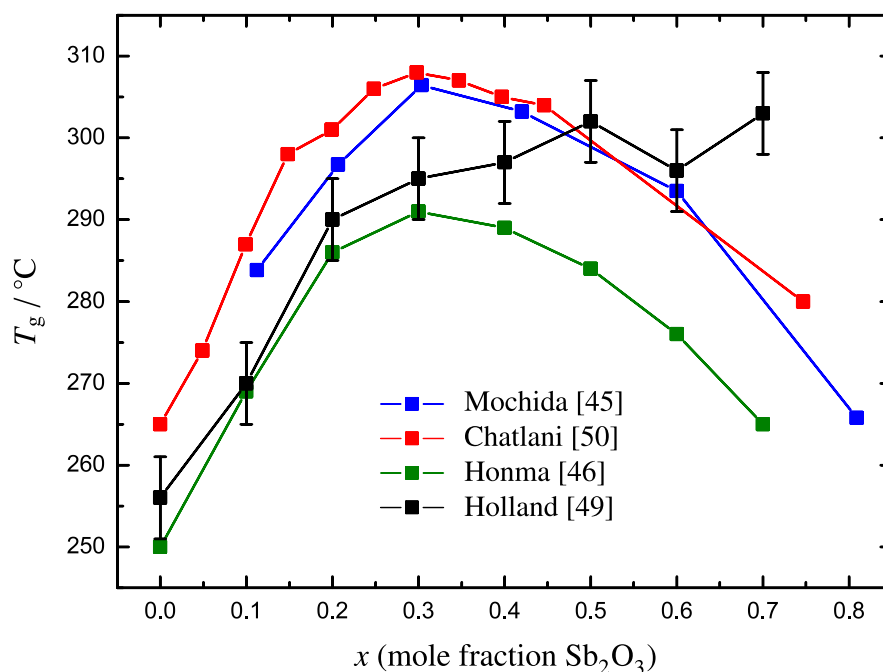


Figure 2-6 Values of T_g for the antimony borate glass system, as measured by various authors [44, 46, 49, 50].

by Holland *et al.* remains anomalous however, as do the lower values of T_g (by 15 °C to 20 °C) reported by Honma *et al.* [46].

Several authors [34, 48, 49] have reported ^{11}B magic angle spinning nuclear magnetic resonance (MAS NMR) data, which they used to estimate the fraction of four-coordinated boron, N_4 , that was present in the glass samples. These estimates (Fig. 2-7) show a good agreement, with the small discrepancies probably attributable to differences in sample preparation, as noted by Holland *et al.* [49]. In a much earlier paper, Mochida and Takahashi [44] had observed from the analysis of Raman spectra that there was evidence of an increase in boron coordination with increasing Sb_2O_3 content, but that this effect was relatively small compared with that in the bismuth borate system also studied (the Raman technique was not able to provide quantitative information): this is consistent with the observation of Holland *et al.* [49] that the values of N_4 for the antimony borate system are unusually low for a binary borate glass.

The consensus in the literature is that the short-range structure of the glass is based on the chains of trigonal $[\text{SbO}_3]$ pyramids found in valentinite. Common justifications are the low viscosity of the glass melt, suggesting a layer- or chain-like structure [21, 22], and the Sb–O bond length of ~ 1.97 together with a coordination of 3 or slightly higher (from X-ray diffraction [22] or EXAFS [48]), implying the basic struc-

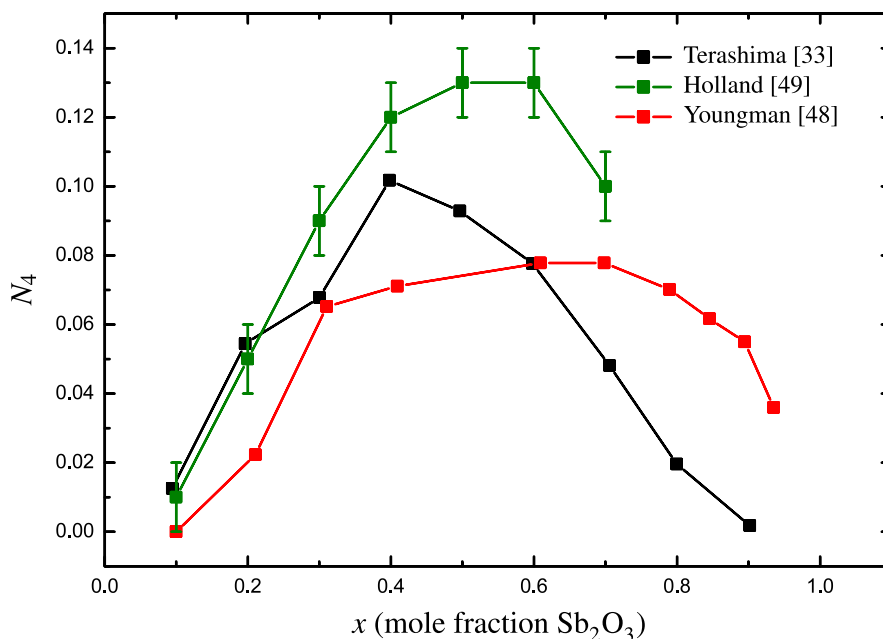


Figure 2-7 Values of N_4 reported in the literature for the antimony borate system [34, 48, 49].

tural unit to be the $[\text{SbO}_3]$ trigonal pyramid. Authors have also published infra-red [21] and Raman data [34] supporting a chain-like structure, as well as reporting the glass crystallising to valentinite [21, 22], and observing quadrupole splitting in Mössbauer spectra that suggests that the $[\text{SbO}_3]$ trigonal pyramid is the basic structural unit [49]. Hasegawa *et al.* [22] also compared the correlation function that they obtained to various models and concluded that the disorder in the structure probably arose from a small number of $[\text{SbO}_3]$ pyramids turned over irregularly within the chains. In addition to the aforementioned EXAFS work, Youngman *et al.* [48] also conducted a Raman study that showed evidence of a number of boroxol rings that decreased with increasing x , appearing to reach zero at $x = 0.6$, together with a small amount of four-coordinated boron (although note that Raman spectroscopy is not quantitative). They concluded that the structure is predominantly a corner-sharing network of $[\text{SbO}_3]$ trigonal pyramids and $[\text{BO}_3]$ planar triangles—the formation of $[\text{BO}_4]$ species then requires the presence of three-fold coordinated oxygen, as noted by Terashima *et al.* [34]. However, Holland *et al.* [49] associated the formation of $[\text{BO}_4]$ with the presence of Sb^{5+} , with experimental data showing good agreement with the amount of the latter present in the samples, at least up to $x \approx 0.5$.

2.5 Antimony silicate glasses

Binary antimony silicate glasses have received little attention in the literature, despite being identified as potential core glasses for low-loss optical waveguides [51, 52] and as a base glass for rare-earth element doping for use in fibre optic amplifiers [53]. The principal work on the structure of the glass system is that of Ellison and Sen [47], where the authors prepared $x \text{ Sb}_2\text{O}_3 \cdot (1 - x) \text{ SiO}_2$ glasses—as well as antimony borates, germanates and arsenates—in silica crucibles at temperatures ranging from 800 °C to 1600 °C, with lower temperatures applying to glasses rich in Sb_2O_3 or B_2O_3 . Silicate samples in the range $x = 0.19$ to $x = 0.82$ were produced, the compositions being determined by “standard wet chemical methods”. From their extended X-ray absorption fine structure (EXAFS) study, the authors concluded that:

- The Sb^{3+} cation is surrounded by three oxygen atoms throughout all four glass systems.
- The oxygen atoms bonded to antimony are only bonded to one other cation.
- The Sb–O bond length changes little between the glass systems at $\sim 1.945 \text{ \AA}$ to $\sim 1.970 \text{ \AA}$, with an r_{SbO} of $1.946(5) \text{ \AA}$ for the antimony silicates at $x < 0.7$, rising to $1.963(5) \text{ \AA}$ for $x \geq 0.7$.

From this, Ellison and Sen deduced that the geometry of the $[\text{SbO}_3]$ coordination polyhedra was well-constrained, with an O–Sb–O angle that is approximately invariant with composition. They also noted that the Sb–O bond length found experimentally is similar to that of senarmontite, and that $[\text{SbO}_3]$ trigonal pyramids, of the form found in the two crystalline polymorphs of Sb_2O_3 , are consistent with the EXAFS data. It was also concluded that, due to the absence of an Sb···Sb peak in glasses with a high Sb_2O_3 concentration, there is considerable disorder in the relative rotational conformations of the corner-sharing $[\text{SbO}_3]$ polyhedra, due to variations in the Sb–O–Sb angle.

In addition to the above work, as part of an investigation of the AC electrical properties of the antimony silicate glass system, Datta *et al.* [54] prepared two antimony silicate glasses by a sol-gel method. Chemical analysis was used to determine the composition of the two samples, as well as the ratio of Sb^{5+} to Sb^{3+} in the glasses before and after heat treatment at 80 °C for 30 minutes, with sample densities also reported;

Table 2-3 Data reported by Datta *et al.* [54] on two antimony silicate glass samples prepared by a sol-gel method.

x	Density (g cm ⁻³)	Sb ⁵⁺ /Sb ³⁺	
		as prepared	after heating at 80 °C for 0.5 h
0.071	2.11	1.12	0.23
0.233	2.69	0.92	0.43

these values are shown in Table 2-3.

Minelly and Ellison [53] also report the preparation of antimony silicate glasses that, under air, must be held above 1000 °C for a time to minimise the formation of cervantite (which contains equal amounts of Sb³⁺ and Sb⁵⁺ [55, 56]); the authors claim that the presence of even traces of Sb⁵⁺ in the glass results in a yellow colouration and high loss in infra-red transmission. Minelly and Ellison also state that the Sb₂O₃ melt is not particularly volatile, resulting in little fuming unless the concentration of Sb⁵⁺ is very high. Unfortunately, the authors do not provide any further details on the preparation or physical properties of the glass system; the remainder of the paper discusses rare-earth-doping and the resultant potential for fibre optic amplifiers.

Most recently, an unpublished ²⁹Si NMR study of antimony silicate glasses by Davies [57] and Mee [58] has suggested that [SiO₄] tetrahedra with four bridging oxygen atoms occur in significant amounts to $x \geq 0.685$. In fact, the observed change in the distribution of Q^n groups ([SiO₄] tetrahedra with n non-bridging oxygen atoms) suggests that a model where the molecular unit added to the network is Sb₂O₃—as opposed to the more standard metal oxide M_{2/z}O (where z is the cation valency)—is more appropriate. This would mean Si–O–Si links being replaced by (Si–O)₂–Sb–O–Sb–(O–Si)₂ or Si–O–Sb=O₂=Sb–O–Si (where the latter indicates edge-sharing of the [SbO₃] polyhedra) and implies that Sb–O–Sb bonds should be present at all concentrations. The authors therefore concluded that the Sb₂O₃ in the glass acts generally as a second network-former.

2.6 Summary

There is little evidence for the production of a single-component antimony oxide glass in the literature: where authors have diligently reported their results, a small quantity of contaminant, often SiO_2 , was evidently present to stabilise the material.

Of the binary antimony glass systems reviewed, only the antimony borates have been studied in detail, with most authors concluding that the structure is based on the chains of trigonal $[\text{SbO}_3]$ pyramids found in valentinite. Antimony silicate glass has been identified as a useful material for optical applications, but little research on the system has been published beyond an initial EXAFS report. The antimony oxychloride system has only recently been discovered, and appears to be based on a crystal with a disputed structure.

There is a dearth of neutron diffraction data on all of these glass systems. This technique could be used to distinguish between the two crystal structures of onoratoite, confirm the N_4 values and structure of the antimony borates, and provide further data on the atomic arrangement in the silicates.

References

- [1] V. M. Jansen, *Acta Crystallogr. B* **35** (3), (1979), 539–542.
- [2] S. E. Golunski and D. Jackson, *Appl. Catal.* **48**, (1989), 123–135.
- [3] C. Svensson, *Acta Crystallogr. B* **31**, (1975), 2016–2018.
- [4] C. Svensson, *Acta Crystallogr. B* **30**, (1974), 458–461.
- [5] W. H. Zachariasen, *J. Am. Chem. Soc.* **54** (10), (1932), 3841–3851.
- [6] P. S. Gopalakrishnan and H. Manohar, *Cryst. Struct. Commun.* **4**, (1975), 203–206.
- [7] J. Amador, E. Gutiérrez Puebla, M. A. Monge, I. Rasines and C. Ruiz Valero, *Inorg. Chem.* **27** (8), (1988), 1367–1370.
- [8] N. E. Brese and M. O’Keeffe, *Acta Crystallogr. B* **47**, (1991), 192–197.
- [9] A. C. Hannon and J. M. Parker, *J. Non-Cryst. Solids* **274**, (2000), 102–109.
- [10] E. J. Roberts and F. Fenwick, *J. Am. Chem. Soc.* **50**, (1928), 2125–2147.
- [11] W. B. White, F. Dacheville and R. Roy, *Z. Kristallogr.* **125**, (1967), 450–458.
- [12] Y. K. Agrawal, A. L. Shashimohan and A. B. Biswas, *J. Therm. Anal.* **7**, (1975), 635–641.
- [13] S. E. Golunski, T. G. Nevell and M. I. Pope, *Thermochim. Acta* **51**, (1981), 153–168.
- [14] I. Barin, *Thermochemical Data of Pure Substances*, vol. 2 (VCH, New York, 1993), 2nd ed.
- [15] P. W. Centers, *J. Solid State Chem.* **72**, (1988), 303–308.
- [16] S. A. Jones, J. Fenerty and J. Pearce, *Thermochim. Acta* **114**, (1987), 61–66.
- [17] V. G. Trofimov, A. I. Sheinkman and G. V. Kleshchev, *Izv. Vuz. Fiz+* **3**, (1973), 135–137.
- [18] C. A. Cody, L. DiCarlo and R. K. Darlington, *Inorg. Chem.* **18** (6), (1979), 1572–1576.
- [19] R. G. Orman, *Phase Transitions in Antimony Oxides and Related Glasses*, MSc Thesis, University of Warwick (2005).
- [20] R. G. Orman and D. Holland, *J. Solid State Chem.* **180** (9), (2007), 2587–2596.

- [21] M. Imaoka, H. Hasegawa and S. Shindo, *J. Ceram. Soc. Jpn.* **77** (8), (1969), 263–271.
- [22] H. Hasegawa, M. Sone and M. Imaoka, *Phys. Chem. Glasses* **19** (2), (1978), 28–33.
- [23] H. Masuda, Y. Ohta and K. Morinaga, *J. Jpn. I. Met.* **59** (1), (1995), 31–36.
- [24] M. Nalin, M. Poulain, M. Poulain, S. J. L. Ribeiro and Y. Messaddeq, *J. Non-Cryst. Solids* **284**, (2001), 110–116.
- [25] P. Charton, P. Thomas and P. Armand, *J. Non-Cryst. Solids* **321**, (2003), 81–88.
- [26] B. Dubois, H. Aomi, J. J. Videau, J. Portier and P. Hagenmuller, *Mater. Res. Bull.* **19**, (1984), 1317–1323.
- [27] J. A. Johnson, D. Holland, J. Bland, C. E. Johnson and M. F. Thomas, *J. Phys. Condens. Mat.* **15**, (2003), 755–764.
- [28] J. A. Johnson, D. Holland, J. Urquidi, I. A. Gee, C. J. Benmore and C. E. Johnson, *J. Phys. Condens. Mat.* **15**, (2003), 4679–4693.
- [29] E. Kordes, *Z. Phys. Chem.* **B43**, (1939), 173–190.
- [30] O. Borgen and J. Krogh-Moe, *Acta Chem. Scand.* **10**, (1956), 265–267.
- [31] Y. P. Kutsenko, I. D. Turyanitsa and D. V. Chepur, *Fiz. Khim. Stekla* **5**, (1979), 395–398.
- [32] J. F. Bednarik and J. A. Neely, *Glastechn. Ber.* **55**, (1980), 126–129.
- [33] P. J. Miller and C. A. Cody, *Spectrochim. Acta A-M.* **38** (5), (1982), 555–559.
- [34] K. Terashima, T. Hashimoto, T. Uchino, S.-H. Kim and T. Yoko, *J. Ceram. Soc. Jpn.* **104** (11), (1996), 1008–1014.
- [35] J. F. Bednarik and J. A. Neely, *Phys. Chem. Glasses* **23** (6), (1982), 204–205.
- [36] A. C. Hannon and D. Holland, (personal communication) (2003).
- [37] F. Sgarlata, *Period. Mineral.* **39**, (1970), 315–328.
- [38] G. Belluomini, M. Fornaseri and M. Nicoletti, *Mineral. Mag.* **36** (284), (1968), 1037–1044.
- [39] S. Menchetti, C. Sabelli and R. Trosti-Ferroni, *Acta Crystallogr. C* **40**, (1984), 1506–1510.

- [40] A. Lipka, *Acta Crystallogr. B* **35**, (1979), 3020–3022.
- [41] M. Edstrand, *Acta Chem. Scand.* **1** (2), (1947), 178–203.
- [42] H. Katzke, Y. Oka, Y. Kanke, K. Kato and T. Yao, *Z. Kristallogr.* **214**, (1999), 284–289.
- [43] Z. Mayerová, M. Johnsson and S. Lidin, *Solid State Sci.* **8**, (2006), 849–854.
- [44] N. Mochida and K. Takahashi, *J. Ceram. Soc. Jpn.* **84** (9), (1976), 413–420.
- [45] T. Honma, R. Sato, Y. Benino, T. Komatsu and V. Dimitrov, *J. Non-Cryst. Solids* **272** (1), (2000), 1–13.
- [46] T. Honma, Y. Benino, T. Komatsu, R. Sato and V. Dimitrov, *J. Chem. Phys.* **115** (15), (2001), 7207–7214.
- [47] A. J. G. Ellison and S. Sen, *Phys. Rev. B* **67**.
- [48] R. E. Youngman, S. Sen, L. K. Cornelius and A. J. G. Ellison, *Phys. Chem. Glasses* **44** (2), (2003), 69–74.
- [49] D. Holland, A. C. Hannon, M. E. Smith, C. E. Johnson, M. F. Thomas and A. M. Beesley, *Solid State Nucl. Mag.* **26**, (2004), 172–179.
- [50] S. Chatlani and J. E. Shelby, *Phys. Chem. Glasses-B* **47** (3), (2006), 288–293.
- [51] M. Shimizu, Y. Ohmori and M. Nakahara, *Electron. Lett.* **21** (19), (1985), 872–873.
- [52] M. Shimizu and Y. Ohmori, *J. Lightwave Technol.* **5** (6), (1987), 763–769.
- [53] J. Minelly and A. Ellison, *Opt. Fiber Technol.* **8**, (2002), 123–138.
- [54] A. Datta, A. K. Giri and D. Chakravorty, *J. Phys. Condens. Mat.* **4**, (1992), 1783–1790.
- [55] P. S. Gopalakrishnan and H. Manohar, *Curr. Sci.* **38**, (1969), 306–307.
- [56] D. J. Stewart, O. Knop, C. Ayasse and F. W. D. Woodhams, *Can. J. Chem.* **50**, (1972), 690–700.
- [57] B. C. Davies, *Antimony Silicate Glasses: Structure and Phase Transitions* (2007), Final Year Project Report, University of Warwick.
- [58] M. Mee, *Antimony Silicate Glasses* (2007), Final Year Project Report, University of Warwick.

Chapter 3

Experimental Theory and Practice

3.1 X-ray diffraction

X-rays incident on a sample will be scattered by the electrons in the atoms of the material. The theoretical treatment is similar to that of neutron scattering, which will be discussed later in some detail (*q.v.* §3.7). However in this work X-ray diffraction (XRD) will only be used for checking the amorphousness of glass samples and for straightforward “finger-printing” of crystalline peaks, and so the theory shall only be touched on briefly.

The typical source of laboratory X-rays is the bombardment of a high-Z metal anode with an electron beam drawn at high voltage from a cathode. Providing that there are incident electrons with enough energy to eject core electrons from the atoms of the anode, X-rays will be released when electrons of a higher shell drop down to fill the vacancy. These X-rays have well-defined energies: copper is a typical anode material, and the drop of an L-shell electron to fill a 1s shell vacancy results in $K_{\alpha 1}$ ($\lambda = 0.15406$ nm) and $K_{\alpha 2}$ ($\lambda = 0.15444$ nm) X-rays being emitted. After monochromating the beam from the anode, these X-rays are then used for diffraction experiments.

After filtering to remove X-rays arising from fluorescence in the sample, the scattered X-rays are counted as a function of 2θ by a detector that sweeps in an arc around the sample, where θ is the angle between the source and the plane of the sample (Fig. 3-1). Periodic ordering in the sample results in narrow Bragg peaks of high intensity (Fig. 3-2) whilst disorder results in broad features of low intensity (Fig. 3-3). This allows the presence of small quantities of crystalline material in a glass matrix to be easily detected, and the Bragg peaks can be matched to data from previous crystal studies to identify the crystalline phase(s) present.

In this work, XRD patterns were obtained using a Bruker D5005 diffractometer with a constant 12 mm footprint on the sample. All runs were over a 2θ range of 10-

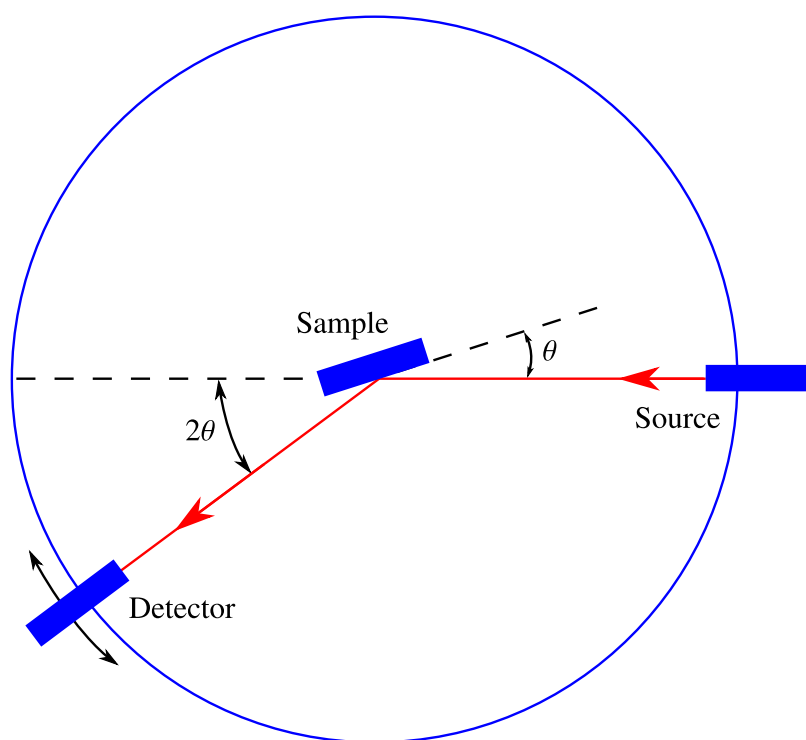


Figure 3-1 The geometry of an X-ray diffractometer.

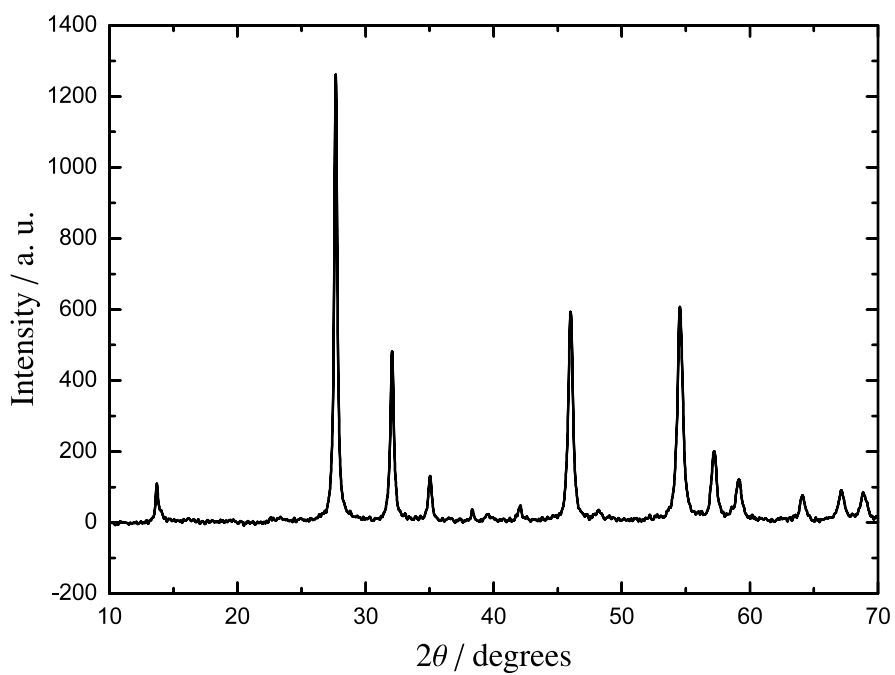


Figure 3-2 An example of the X-ray diffraction pattern of a crystalline material (α - Sb_2O_3 [1]).

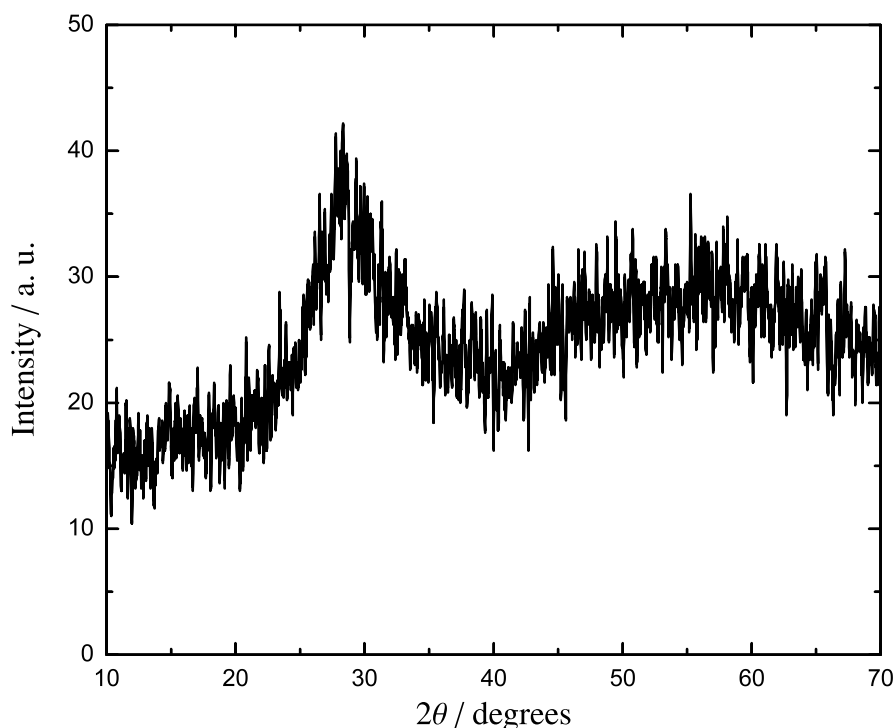


Figure 3-3 An example of the XRD pattern of a glass (“chlorine-stabilised Sb_2O_3 ” [2]).

70° at 0.02° increments using a copper K_α radiation source at 40 kV-30 mA. Circular aluminium holders of diameter 20 mm were used and any diffraction peaks resulting from the holders are labelled. An acquisition time of 5 seconds per angular increment was used for all samples. For clarity, all XRD patterns have been smoothed with a five-point Fast Fourier Transform algorithm, and where crystalline peaks are present they have been matched with patterns generated using crystal data from the Inorganic Crystal Structure Database [3].

3.2 Energy-dispersive X-ray spectroscopy

Energy Dispersive X-ray spectroscopy (EDX) uses a high-energy (~ 10 keV) electron beam to produce X-rays from a sample in the same fashion that a laboratory X-ray diffractometer does from a metal anode. Because the X-rays are characteristic of the elements present in the target, examining a spectrum of the relative counts of the detected X-rays by energy allows the elemental composition of the sample to be determined quantitatively (after suitable standardisation).

The corrections that need to be applied to the measured intensities include:

1. The atomic number (or “Z”) correction, which accounts for differences between the electron scattering and penetration in the sample and the standard.
2. The absorption (“A”) correction, to allow for the absorption of the X-rays as they pass through the sample or standard.
3. The fluorescence (“F”) correction, which compensates for the fluorescence of X-rays by the characteristic and continuum X-rays generated in the sample by the electron beam.

A JEOL 6100 Scanning Electron Microscope (SEM) and a 10 kV accelerating voltage were used for all EDX measurements. ZAF corrections to the recorded X-ray emission spectra were calculated with reference to a set of characterised internal standards. The effect of the limited penetration depth of the electron beam was minimised by measurement of freshly-powdered samples; nevertheless, values obtained from this technique are only accurate to $\pm 2\%$.

3.3 Thermal analysis techniques

Differential Thermal Analysis (DTA) measures the temperature difference between a sample and a reference material (that is usually inert) when both are subjected to the same heating program. An endothermic or exothermic event will cause the sample temperature T_s to either lag behind or precede, respectively, the reference temperature T_r . A graph of $\Delta T (= T_s - T_r)$ versus T_s shows thermal events as peaks with characteristic onset temperatures (Fig. 3-4); the position of the peak maximum is dependent on factors such as heating rate and sample size, and the area under each peak is related to the enthalpy change for the thermal event.

Differential Scanning Calorimetry (DSC) is superficially similar to DTA, but differs in that it records the thermal energy required to maintain the desired heating rate in the sample compared to a reference, instead of the temperature differential. Unlike DTA, the sample and reference are placed in separate furnaces and the temperature program is maintained by varying the power input to the two heating elements. The energy required to do this serves as a direct measure of the enthalpy changes in the sample relative to the reference (usually just an empty pan for DSC).

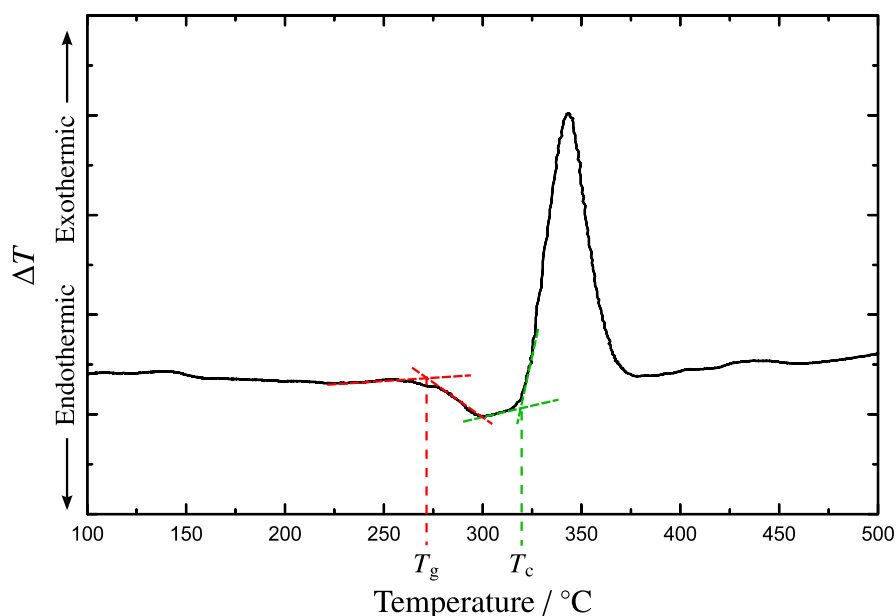


Figure 3-4 An example of a DTA curve with extrapolated glass transition and crystallisation temperatures. Note that extrapolated onset temperatures are quoted throughout this work, unless otherwise stated, since peak temperatures are often dependent on factors such as heating rate and sample size.

Thermogravimetric Analysis (TGA) measures changes in mass with temperature. Although limited to examining thermal events where this occurs (typically desorption, decomposition and oxidation), in these situations TGA can often produce much useful information, particularly regarding stable and meta-stable intermediates formed during a thermal process. TGA can also be combined with DTA or DSC to give concurrent measurements: this makes drawing conclusions about the thermal behaviour significantly easier, whilst avoiding the potential difficulties of preparing identical samples for analysis in parallel experiments.

A Mettler Toledo TGA/DSC 1 system was used for all TGA/DSC measurements, heating samples to 800 °C at a rate of 10 °C min⁻¹ with nitrogen flowing at 50 ml min⁻¹ as a purge gas. Sample masses were typically 10 mg to 20 mg and were held in 70 µl platinum pans with lids (a hole in the lid allowed gas to flow around the sample). An alumina pan was used for the reference, and an empty sample pan (with lid) was run initially to provide a baseline correction for the measured data.

3.4 Raman spectroscopy

Raman spectroscopy exploits the phenomenon of *Raman scattering*, first discovered by Raman and Krishnan [4] in 1928. In this work, the technique is only used for fingerprinting and qualitative analysis of the glass structure, although it can also be utilised for more in-depth structural determination—see, for example, the discussion of its applications to silicate glasses by McMillan [5]. The theory of the technique will therefore only be discussed briefly below: for a more detailed treatment, see the works of Banwell [6] and Nakamoto [7].

When electromagnetic radiation is incident on a surface, a majority of the scattered radiation will be of the same frequency as the incident beam. However, a certain minority of the scattered energy will be at discrete frequencies above and below that of the incident radiation, due to a process known as Raman scattering.

Scattering can be explained in terms of the quantum theory of radiation. The incident radiation of frequency ν will consist of photons of discrete energies $h\nu$ (h is Planck's constant) and, as these photons impact on the molecules of the target surface, scattering will occur. If the scattering is perfectly elastic the energy of the scattered photons will be unchanged, as will their frequency—this is *Rayleigh scattering*.

Should the photon-molecule collision be inelastic however, the energy change ΔE will be the difference between two of the allowed states of the molecule: in other words, ΔE must represent a change in the rotational or vibrational energy. If the molecule is to gain energy, the photon must itself have an energy of $h\nu - \Delta E$ on scattering, and conversely, a $h\nu + \Delta E$ photon will scatter if the molecule loses energy during the collision. The frequency of the scattered radiation will also be $\nu - \Delta E/h$ or $\nu + \Delta E/h$, respectively.

Radiation scattered at a lower frequency in this manner is known as *Stokes' radiation*, whilst higher frequency scattering is called *anti-Stokes' radiation*. Since a decrease in molecular energy (anti-Stokes') can only occur if the molecule is already in an excited state, Stokes' scattering is the more common form—however, both types of Raman scattering are still rare compared to Rayleigh scattering.

Since the Raman scattering process is not very efficient (approximately 1 in 10^7 incident photons will scatter in this way) a laser is required to act as a high-power light source. The laser is also monochromatic so that all of the photons will initially have the same energy and will interact with the target molecules in the same way. Some

molecular vibrations will also scatter polarised light; in general, the more symmetric the vibration the more polarised the associated Raman scattering. Thus by examining either the polarised or unpolarised scattering from a sample, different sets of Raman excitations can be highlighted.

Unpolarised Raman spectra in this work were obtained from a Renishaw Invia Raman spectrometer equipped with a 20 mW argon laser of wavelength 514 nm. Measurements were acquired with 10 mW incident laser power with $\times 50$ magnification at room temperature. 5-10 acquisitions were typically obtained for each sample, and the response was measured over the entire frequency shift range of the equipment (100 cm^{-1} to 3200 cm^{-1}). The percentage power of the laser was also adjusted to prevent peaks being truncated by saturation of the detector: 5 % power was the lowest setting required, and was used for most samples. Some polarised Raman spectra were also obtained using a Jasco NRS-3100 Raman spectrometer with a 20 mW SLM diode laser of wavelength 785 nm, over a frequency shift range of 50 cm^{-1} to 1800 cm^{-1} .

Due to the localised nature of the Raman analysis (the spot targeted is approximately $10\text{ }\mu\text{m}$ in diameter), minor variations in composition and geometry can cause changes in the spectra obtained for a single sample. To minimise this, three measurements were taken at different points on each sample, and the averaged spectrum was used for analysis.

3.5 Mössbauer spectroscopy

The energy levels of a nucleus are affected by the local environment, and Mössbauer spectroscopy is used to investigate these effects. Many elements, when produced by radioactive decay of an isotope, are initially in an excited state and will emit γ -rays of a specific energy as their constituent nuclei revert to the ground state. If an unexcited nucleus of the same element were to be placed in the path of these gamma rays, it would be expected to absorb energy from the beam and itself become excited—this absorption can be measured by a suitable detector (such as a scintillation counter).

For this process to work in practice, the energy of the emitted γ -ray must match that of the nuclear transition very precisely, a condition that is inhibited by the recoil of the nucleus (to conserve momentum; this is also an issue during absorption in the target).

Since the source nucleus is then moving as the γ -ray is emitted, the Doppler effect will also shift the frequency (and hence, energy) of the photon produced. These two effects, whilst relatively small, will change the energy of the emitted γ -ray sufficiently that it no longer matches the value required to excite the sample nucleus.

However, by using source nuclei that are fixed in a solid crystalline lattice, the effect due to recoil can be minimised (since it is the whole lattice, rather than a single nucleus, that recoils). By cooling both source and sample, the effect of lattice vibrations can also be reduced. The only remaining impediment to absorption is then the effect of the local environment on the energy level in the sample: the property that the technique aims to measure. By oscillating the source towards and away from the sample during the measurement (typically at speeds of a few mm s^{-1}), the Doppler effect can be employed beneficially to scan through the range of energies close to that of the nuclear transition. By plotting γ -ray count as a function of source velocity, dips due to absorption will be recorded in proportion to the amounts of different environments experienced by the target element in the sample.

In this work, ^{121}Sb Mössbauer spectra were obtained at 77 K by Dr Mike Thomas at the University of Liverpool. A $\text{Ca}^{121\text{m}}\text{SnO}_3$ source with a constant acceleration drive was used for the measurements, with the velocity scale calibrated using a ^{57}Co source and a ^{57}Fe absorber. The scale was then converted to an InSb reference by adding 8.6 mm s^{-1} . A sample of commercial Sb_2O_4 was also run to check that the correct amounts of Sb^{3+} and Sb^{5+} were being detected by this method.

3.6 Density measurements

Density can be determined for a sample of known mass if the volume can be found accurately, and this can be achieved by measuring the amount of a fluid that the sample displaces. In this work, two models of helium gas pycnometer were used for this purpose: a Quantachrome micropycnometer and a Micromeritics AccuPyc 1330 pycnometer—most samples were run on both instruments. Sample masses were measured on a Precisa 125A balance to the nearest tenth of a milligram.

A gas pycnometer consists of two cells connected by a valve, with a further valve on each cell to permit gas flow into or out of the system (Fig. 3-5). Only the sample

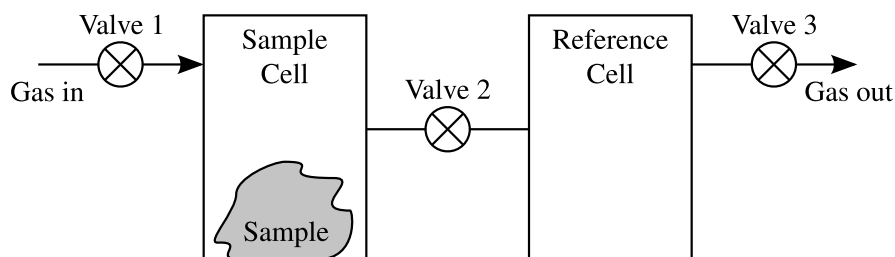


Figure 3-5 A schematic diagram of a gas pycnometer.

cell is accessible to the user. The pycnometer measures the change in pressure when the volume of gas in the sample chamber expands into the reference cell, and hence determines the volume of the sample. To reduce error, the measurement is repeated until the pressure readings stabilise to within a given tolerance (± 0.034 kPa or ± 0.005 psi in this work) and the volume is then calculated from a mean average of the last five readings. After loading the sample and prior to commencing the measurement, the system was purged with helium for ~ 10 min to remove moisture and air from the sample surface.

3.7 Neutron diffraction

3.7.1 Properties of the neutron

The neutron, first discovered by Chadwick [8] in 1932, is a neutral subatomic particle with mass m_n of 1.0087 u. These properties have allowed *thermal neutrons*—that is, those neutrons with an energy E of ~ 25 meV, and so called because this is the most probable energy at room temperature—to become a valuable tool for investigating the structure of condensed matter. The velocity of a thermal neutron (~ 2.20 km s $^{-1}$) results in a de Broglie wavelength of ~ 1.8 Å (Eqn. (3-1))—this is the order of magnitude of interatomic distances in solids and liquids, and therefore causes interference effects that can be interpreted to yield structural information.

$$\lambda = \frac{h}{mv} \quad (3-1)$$

Furthermore, the uncharged nature of a neutron allows it to penetrate deeply into the target, and so to approach the nuclei close enough to be scattered by nuclear forces. This is important when considered in comparison to X-ray diffraction (q.v. §3.1) where

Table 3-1 Neutron scattering lengths and atomic numbers for the elements present in the samples studied in this work. Where not listed as a specific isotope, the scattering length for the element at natural abundance is given.

Element or isotope	Neutron scattering length (fm)	Atomic number
^{11}B	6.65	5
O	5.803	8
Si	4.1491	14
Cl	9.577	17
^{37}Cl	3.08	
Sb	5.57	51

scattering is proportional to atomic number—hydrogen, for example, scatters neutrons very strongly, but is almost transparent to X-rays. The strength of neutron scattering exhibited by an atom—represented by the *scattering length*, b —is currently determined empirically, and varies with both the element and the isotope. This often results in neutron scattering providing complementary data to that of X-ray diffraction, with each technique weighting the scattering contribution of each element differently (Table 3-1), as well as allowing further structural information to be obtained from the measurement of otherwise identical samples with different isotopic distributions.

The energy of a thermal neutron is also of the order of many excitation energies in condensed matter. This means that the change in energy of a neutron that is scattered inelastically by the creation or destruction of an excitation is a large fraction of its initial energy, and measurement of this change gives accurate information on the energy of the excitation. In comparison, X-rays of a similar wavelength have energies many orders of magnitude higher, resulting in a very small change in relative energy from the excitation.

Finally, the neutron possesses a magnetic moment that allows it to interact with the unpaired electrons in magnetic atoms, and the elastic and inelastic scattering that results can be used to obtain information on the magnetic structure of the sample.

3.7.2 Neutron scattering theory

3.7.2.1 Introduction

For the convenience of the reader, this section will briefly introduce the theory of neutron scattering, drawing heavily from the works of Squires [9] and Hannon [10]—in places the latter has been quoted nearly *verbatim*, with changes only for clarity and to improve the relevance to this work. The practical aspects of the neutron experiments conducted in this work follow after this section; for the reader seeking a more detailed treatment of the theory, the discussions by Wright [11] and Sköld and Price [12] are recommended.

3.7.2.2 Scattering cross-sections

Consider a beam of thermal neutrons, each with energy E_i , incident on a target—the *scattering system*—with flux Φ . A detector exists in the direction (θ, ϕ) where it will record the number of neutrons scattered into the solid angle $d\Omega$ as a function of their energy after scattering E_f (Fig. 3-6). The *double differential cross-section* is then defined by

$$\frac{d^2\sigma}{d\Omega dE} = \frac{R_{\text{inel}}}{\Phi d\Omega dE} \quad (3-2)$$

where R_{inel} is the number of neutrons inelastically scattered per unit time into the solid angle $d\Omega$ in the direction (θ, ϕ) with final energy E_f in the range $E_i - E$ to $E_i - (E + dE)$. The energy $E (= E_i - E_f)$ is that transferred to the sample from the neutron. By considering only the neutrons that are scattered elastically ($E = 0$) we can obtain the definition of the *differential cross-section*

$$\frac{d\sigma}{d\Omega} = \frac{R_{\text{el}}}{\Phi d\Omega} \quad (3-3)$$

where R_{el} is the number of neutrons scattered per unit time into the solid angle $d\Omega$ in the direction (θ, ϕ) . Finally, the *total scattering cross-section* is defined by

$$\sigma_{\text{tot}} = \frac{R_{\text{tot}}}{\Phi} \quad (3-4)$$

where R_{tot} is the total number of neutrons scattered per unit time in all directions. The three cross-sections are therefore related by

$$\frac{d\sigma}{d\Omega} = \int_{-\infty}^{\infty} \left(\frac{d^2\sigma}{d\Omega dE} \right) dE \quad (3-5)$$

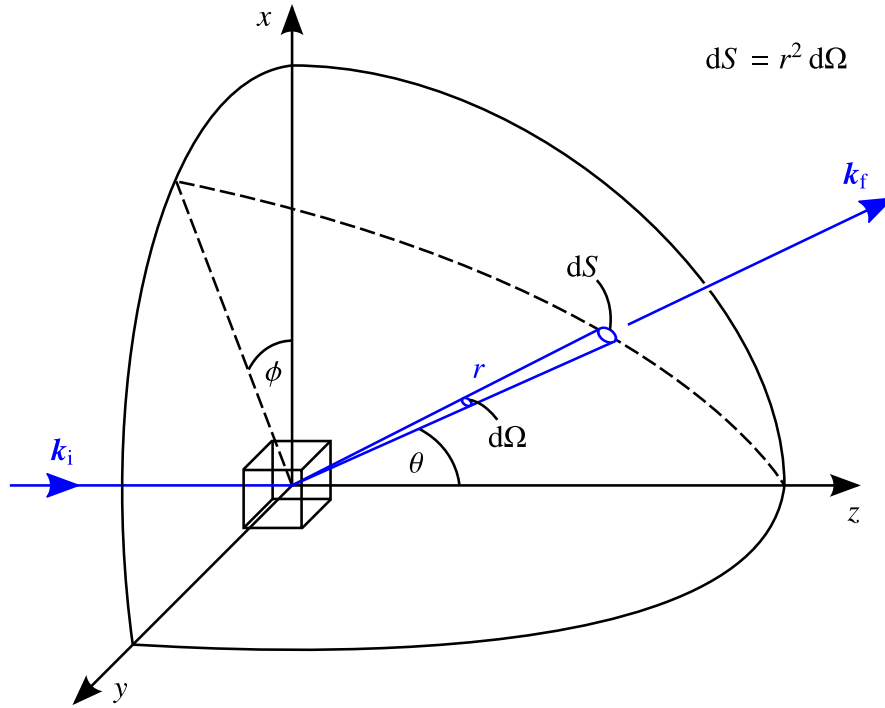


Figure 3-6 The geometry of a neutron scattering experiment. Diagram adapted from Squires [9] and Hannon [10].

and

$$\sigma_{\text{tot}} = \int_{\text{all directions}} \left(\frac{d\sigma}{d\Omega} \right) d\Omega \quad (3-6)$$

If the scattering is axially symmetric about ϕ , (3-6) becomes

$$\sigma_{\text{tot}} = \int_0^\pi \frac{d\sigma}{d\Omega} 2\pi \sin \theta d\theta \quad (3-7)$$

since, from Figure 3-6,

$$d\Omega = \sin \theta d\theta d\phi \quad (3-8)$$

Experimental cross-sections are quoted per atom, i.e. the above equations are divided by the number of atoms in the scattering system.

3.7.2.3 Scattering from a single fixed nucleus

As noted in §3.7.1, the wavelength λ of a thermal neutron is of the order of 1 \AA : since the nuclear forces that cause scattering are of a much shorter range ($\sim 10^{-15} \text{ m}$), nuclei can be considered as point-like scattering centres that give rise to scattered neutron waves that are spherically symmetric.

Consider a nucleus that is fixed in position at the origin, with the z -axis along the direction of \mathbf{k}_i , the wave vector of the incident neutrons (Fig. 3-6). The incident neutrons can be represented by the wavefunction

$$\Psi_{\text{inc}} = \exp(ikz) \quad (3-9)$$

and the wavefunction of the scattered neutrons at the point \mathbf{r} is

$$\Psi_{\text{sc}} = -\frac{b}{r} \exp(ikr) \quad (3-10)$$

where b is a constant known as the (*bound atom*) *scattering length* with dimensions of [length]. Note that the scattering is elastic (because the nucleus is fixed and the energy of the neutrons is too small to excite it) and so the magnitude of \mathbf{k}_i is unchanged after scattering (so $k_i = k_f = k$).

The value of the scattering length is dependent upon the type of nuclide (element and isotope) and its spin—for a nucleus with non-zero spin I there will be two scattering lengths, corresponding to the neutron-nucleus spin states $I + \frac{1}{2}$ and $I - \frac{1}{2}$ (the neutron has spin $\frac{1}{2}$); a nucleus with zero spin will only have a single scattering length, corresponding to the spin state $\frac{1}{2}$. Most scattering lengths are positive, corresponding to a phase change of π between the scattered and incident waves, but a small number of nuclides have negative scattering lengths. The value of b is determined empirically, and shows no obvious trend with the position in the periodic table.

The flux of the incident neutrons on the static nucleus is

$$\Phi = v |\Psi_{\text{inc}}|^2 = v \quad (3-11)$$

where v is the velocity of the neutrons (before and after the elastic scattering). The number of scattered neutrons passing through an area dS (Fig. 3-6) is

$$v dS |\Psi_{\text{sc}}|^2 = v dS \frac{b^2}{r^2} = vb^2 d\Omega \quad (3-12)$$

By substituting equations (3-11) and (3-12) into equation (3-3) we obtain the expression for the differential cross section for a single fixed nucleus

$$\frac{d\sigma}{d\Omega} = \frac{vb^2 d\Omega}{\Phi d\Omega} = b^2 \quad (3-13)$$

and by using this result with equation (3-4) the expression for the total scattering cross section is shown to be

$$\sigma_{\text{tot}} = 4\pi b^2 \quad (3-14)$$

Thus the total scattering from a single fixed nucleus is proportional to b^2 . Values for b and σ for the various nuclides are given by Sears [13].

3.7.2.4 Fermi pseudo-potential

The interaction between a neutron and a scattering system may be represented by the Fermi pseudo-potential

$$V(\mathbf{r}) = \frac{2\pi\hbar^2}{m_n} \sum_{j=1}^N b_j \delta(\mathbf{r} - \mathbf{R}_j) \quad (3-15)$$

where m_n is the mass of a neutron, and the summation is taken over the N nuclei whose position vectors and scattering lengths are \mathbf{R}_j and b_j respectively. Together with Fermi's golden rule (which, for scattering purposes, is equivalent to the Born approximation), this representation results in a general expression for the nuclear scattering of neutrons:

$$\frac{d^2\sigma}{d\Omega dE} = \frac{1}{N} \frac{k_f}{k_i} \frac{1}{2\pi\hbar} \sum_{j,j'}^N b_j b_{j'} \int_{-\infty}^{\infty} \langle \exp \{ -i\mathbf{Q} \cdot [\mathbf{R}_j(0) - \mathbf{R}_{j'}(t)] \} \rangle \exp(iEt/\hbar) dt \quad (3-16)$$

The angular brackets represent a thermal average at the temperature T of the scattering system. $\mathbf{R}_j(t)$ is the position of the j th nucleus at time t , and \mathbf{Q} is the *scattering vector*, defined by

$$\mathbf{Q} = \mathbf{k}_i - \mathbf{k}_f \quad (3-17)$$

where \mathbf{k}_i and \mathbf{k}_f are the incident and scattered neutron wave vectors, respectively. \mathbf{Q} is also commonly referred to as the *momentum transfer*, although this term should more properly be used for the expression $\hbar\mathbf{Q}$.

Note that the Fermi pseudo-potential does not correspond to the actual scattering potential. Nor do the conditions necessary for Fermi's golden rule to apply hold true for the nuclear scattering of thermal neutrons (the rule is based on perturbation theory). However, when combined, the golden rule and the pseudo-potential give the required model of isotropic scattering for a single fixed nucleus, and this result is used to justify their use [14, 15].

3.7.2.5 Total diffraction: elastic scattering

In elastic scattering the magnitude of the neutron wave vectors is unchanged by scattering ($k_i = k_f$) so the scattering vector may be evaluated as

$$|\mathbf{Q}| = Q = 2k \sin \theta = \frac{4\pi \sin \theta}{\lambda} \quad (3-18)$$

Also, equation (3-16) can be integrated as equation (3-5) to give

$$\frac{d\sigma}{d\Omega} = I(\mathbf{Q}) = \frac{1}{N} \sum_{j,j'}^N b_j b_{j'} \left\langle \exp \left\{ -i\mathbf{Q} \cdot [\mathbf{R}_j(0) - \mathbf{R}_{j'}(t)] \right\} \right\rangle \quad (3-19)$$

Therefore the total diffraction pattern $I(\mathbf{Q})$ depends upon the vectors \mathbf{R}_j to $\mathbf{R}_{j'}$ between atoms, with a weighting from the scattering lengths. Thus total diffraction depends upon the atom positions at an arbitrary time zero, and so gives an instantaneous ‘snapshot’ of the interatomic vectors. Note that the assumptions for the fixed nucleus model do not hold exactly and as a result an inelasticity correction, first calculated by Placzek [16], must be made to total diffraction data.

3.7.2.6 Total diffraction: coherent and incoherent scattering

Equation (3-19) can also be written in the form

$$I(\mathbf{Q}) = \sum_{j,j'}^N b_j b_{j'} \langle j, j' \rangle \quad (3-20)$$

The scattering length b_j for an individual nucleus of an element varies with the isotope and spin (q.v. §3.7.2.3)—these effects are known as *isotopic incoherence* and *spin incoherence*. Therefore, to obtain a useful result, equation (3-20) is averaged over all possible distributions of scattering length, assuming that there is no correlation between the values of b_j for any two nuclei. Now the average value of $b_j b_{j'}$ is

$$\begin{aligned} \overline{b_j b_{j'}} &= (\bar{b})^2, & j \neq j' \\ \overline{b_j b_{j'}} &= \bar{b}^2, & j = j' \end{aligned} \quad (3-21)$$

where \bar{b} is the average scattering length (usually known as the *coherent scattering length*) for all nuclei of a particular element, whilst \bar{b}^2 is the average of the squared scattering length for the element. The double summation of equation (3-20) may now be separated into $j \neq j'$ (“*distinct*”) terms and $j = j'$ (“*self*”) terms:

$$I(\mathbf{Q}) = i(\mathbf{Q}) + \sum_l c_l \bar{b}_l^2 \quad (3-22)$$

where $c_l = N_l$, the atomic fraction for element l , and the distinct differential cross-section is

$$i(\mathbf{Q}) = \sum_{l,l'}^N \bar{b}_l \bar{b}_{l'} \sum_{j=1, j \neq j'}^{N_l} \sum_{j'=1}^{N_{l'}} \frac{1}{N} \left\langle \exp \left\{ -i\mathbf{Q} \cdot [\mathbf{R}_j(0) - \mathbf{R}_{j'}(t)] \right\} \right\rangle \quad (3-23)$$

The l and l' summations are over the types of elements in the sample (e.g. for $\text{Sb}_4\text{O}_5\text{Cl}_2$, $l = \text{Sb, O, Cl}$). The j (or j') summations are then over all the N_l (or $N_{l'}$) atoms of element l (or l'), excluding terms where j and j' refer to the same atom. By adding and subtracting a $\sum_j \overline{b_j^2} \langle j, j \rangle$ term the differential cross-section for total diffraction may be separated into its coherent and incoherent parts:

$$I(\mathbf{Q}) = \left\langle \overline{b^2} \right\rangle_{\text{av}} S(\mathbf{Q}) + \frac{\sigma_{\text{inc}}}{4\pi} \quad (3-24)$$

where the structure factor is given by

$$S(\mathbf{Q}) = \frac{1}{\left\langle \overline{b^2} \right\rangle_{\text{av}}} \sum_{l,l'} \overline{b_l} \overline{b_{l'}} \sum_{j,j'} \frac{1}{N} \left\langle \exp \left\{ -i\mathbf{Q} \cdot [\mathbf{R}_j(0) - \mathbf{R}_{j'}(0)] \right\} \right\rangle = 1 + \frac{i(\mathbf{Q})}{\left\langle \overline{b^2} \right\rangle_{\text{av}}} \quad (3-25)$$

in which self terms ($j = j'$) are now included in the summation. The coherent and incoherent cross-sections of the sample are

$$\sigma_{\text{coh}} = 4\pi \left\langle \overline{b} \right\rangle_{\text{av}}^2 \quad \sigma_{\text{inc}} = 4\pi \left(\left\langle \overline{b^2} \right\rangle_{\text{av}} - \left\langle \overline{b} \right\rangle_{\text{av}}^2 \right) \quad (3-26)$$

in which average values for the sample are defined as

$$\begin{aligned} \left\langle \overline{b} \right\rangle_{\text{av}} &= \sum_l c_l \overline{b_l} \\ \left\langle \overline{b^2} \right\rangle_{\text{av}} &= \sum_l c_l \overline{b_l^2} \end{aligned} \quad (3-27)$$

The coherent differential cross-section $\left\langle \overline{b^2} \right\rangle_{\text{av}} S(\mathbf{Q})$ is what would be measured from a sample for which all nuclei of element l had a scattering length of $\overline{b_l}$. It is the coherent contribution to the differential cross-section that contains the interference information relating to the positions of the atoms in the sample; the self and incoherent contributions are featureless (Fig. 3-7). For most elements the incoherent cross-section is relatively small, but a notable exception is hydrogen for which it is very large, such that the measured experimental diffraction pattern is dominated by the incoherent contribution.

3.7.2.7 Total diffraction from a disordered sample

For an isotropic sample, the diffraction pattern only depends upon the magnitude of the momentum transfer \mathbf{Q} vector. In this case the distinct scattering $i(\mathbf{Q})$ (Eqn. (3-22)) is related to a neutron correlation function $T(r)$ by a Fourier transform:

$$T(r) = T_0(r) + \frac{2}{\pi} \int_0^\infty Q i(\mathbf{Q}) \sin(rQ) dQ \quad (3-28)$$

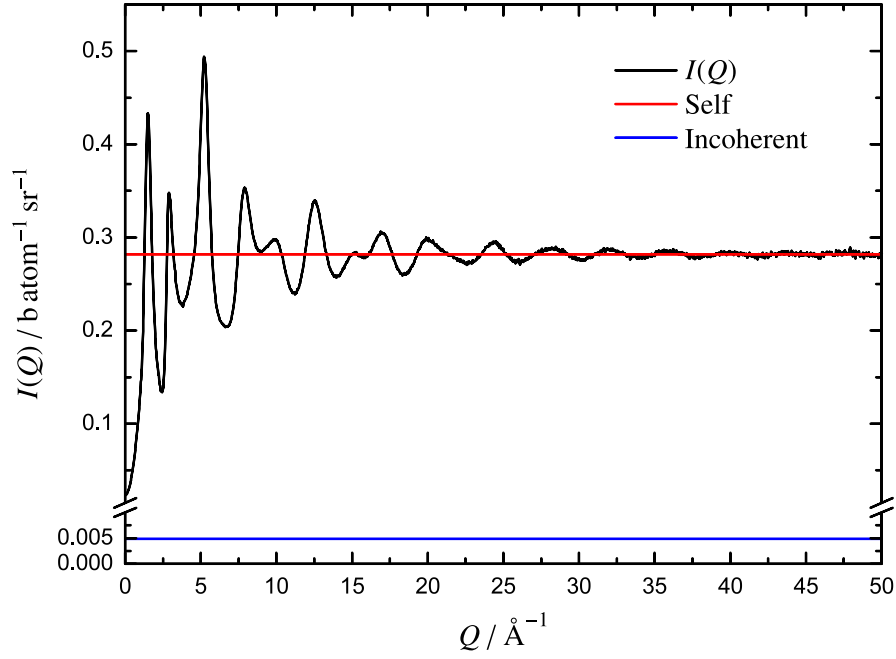


Figure 3-7 The total diffraction pattern, $I(Q)$, for SiO_2 glass [17], shown together with the self and incoherent contributions. Note that for an isotropic sample such as a glass the direction of the \mathbf{Q} vector is unimportant.

$T_0(r)$ is the average density contribution to the correlation function, given by

$$T_0(r) = 4\pi r g_0 \left(\sum_l c_l \bar{b}_l \right)^2 \quad (3-29)$$

where g_0 is the average number of atoms per unit volume in the sample, c_l is the atomic fraction for element l , and the l summation is over the types of elements in the sample. Figure 3-8 shows the neutron correlation function, $T(r)$, for SiO_2 glass, obtained by Fourier transformation of the diffraction data shown in Figure 3-7; also shown is the average density contribution $T_0(r)$.

Since the measured range of Q terminates at some finite value Q_{\max} , termination ripples will appear in the real-space data obtained from the Fourier transformation. A modification function $M(Q)$, such as that given by Lorch [18], is often used to reduce these ripples:

$$\begin{aligned} M(Q) &= \frac{\sin \Delta r Q}{\Delta r Q}, & Q \leq Q_{\max} \\ M(Q) &= 0, & Q > Q_{\max} \end{aligned} \quad (3-30)$$

where the resolution in real-space is $\Delta r = 2\pi/Q_{\max}$. With $M(Q)$, equation (3-28) becomes

$$T(r) = T_0(r) + \frac{2}{\pi} \int_0^\infty Q i(Q) M(Q) \sin(rQ) dQ \quad (3-31)$$

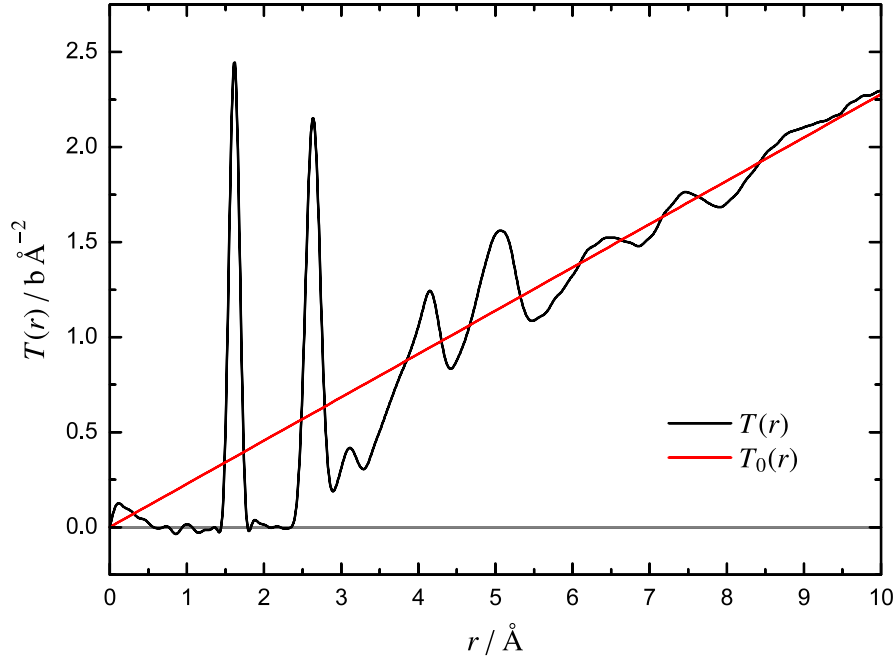


Figure 3-8 The neutron correlation function, $T(r)$, for SiO_2 glass [17], obtained from the data in Figure 3-7. Also shown is the average density contribution, $T_0(r)$.

The total correlation function is a weighted sum of partial correlation functions:

$$T(r) = \sum_l \sum_{l'} c_l \bar{b}_l \bar{b}_{l'} t_{ll'}(r) \quad (3-32)$$

Each partial correlation $t_{ll'}(r)$ is related to a generalised van Hove distinct correlation function [19] by

$$t_{ll'}(r) = 4\pi r G_{ll'}^D(r, 0) \quad (3-33)$$

where

$$G_{ll'}^D(r, t) = \frac{1}{N_l} \sum_{j=1, j \neq j'}^{N_l} \sum_{j'=1}^{N_{l'}} \int \langle \delta(\mathbf{r}' - \mathbf{R}_j(0)) \cdot \delta(\mathbf{r}' + \mathbf{r} - \mathbf{R}_{j'}(t)) \rangle d\mathbf{r}' \quad (3-34)$$

It can be interpreted from the above equations that $r t_{ll'}(r) dr$ is the average number of atoms of element l' which are located in a spherical shell of radius r to $r + dr$, centred on an atom of element l (Fig. 3-9). For the experimental data for SiO_2 glass shown in Figure 3-8, the first peak in the correlation function arises from the nearest neighbour Si–O bonds, whilst the second peak arises from the non-bonded O···O distance in the $[\text{SiO}_4]$ tetrahedra that form the random network structure.

The expected lengths of particular atom-atom correlations can be predicted from bond-valence parameters, as explained by Hannon and Parker [20]:

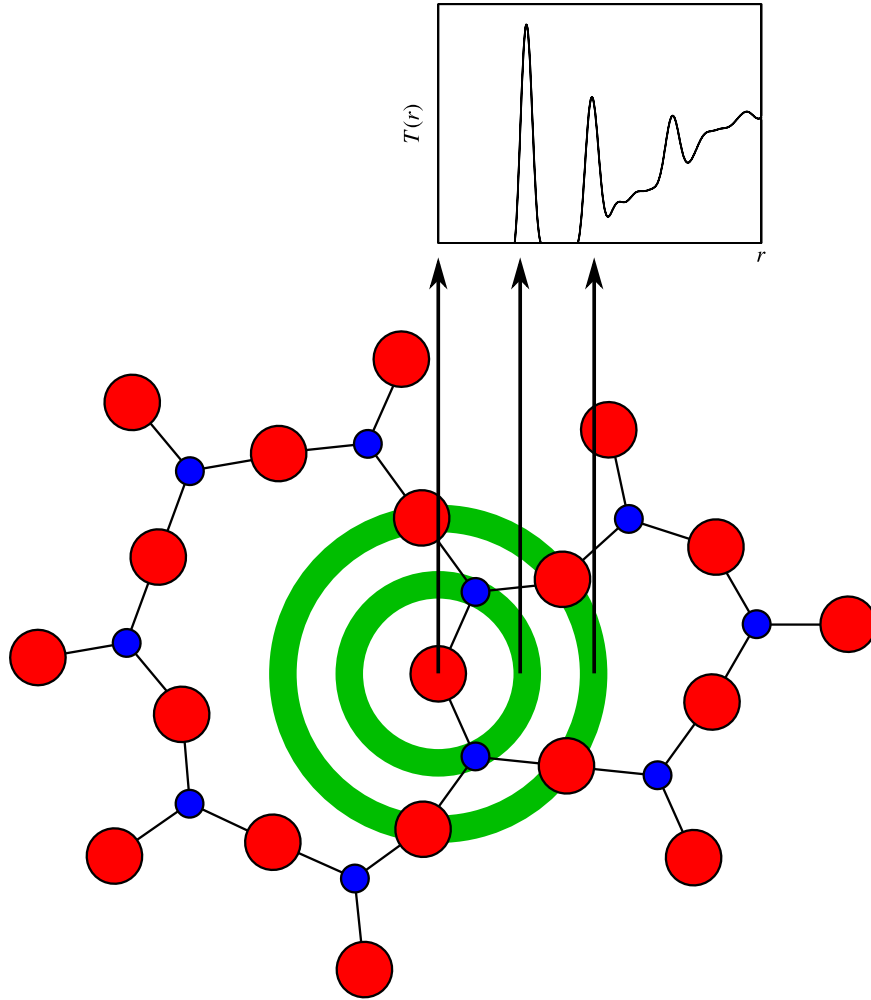


Figure 3-9 A simulated neutron correlation function, $T(r)$, together with a fragment of an A_2X_3 network, showing how the peaks in the correlation function arise from the interatomic distances.

“According to bond-valence theory [21] the valence of an atom i may be expressed in the form

$$V_i = \sum_j v_j = \sum_j \exp\left(\frac{R_{ij} - d_{ij}}{b}\right), \quad (3-35)$$

where the summation is performed over its neighbours, j . d_{ij} and v_{ij} are the length and the valence of the bond between atoms i and j , respectively. R_{ij} is the bond-valence parameter for the atom pair (i, j) (tabulated values for R_{ij} , based on crystal structures, are given by Brese and O’Keeffe [21]) and b is a universal constant (0.37 \AA). If we make the simplifying assumption that all of the n_{ij} neighbours to atom i have the same bond length, d_{ij} , then

this interatomic distance is given by

$$d_{ij} = R_{ij} + b \log_e \left(\frac{n_{ij}}{V_i} \right) .” \quad (3-36)$$

3.7.3 ISIS: A pulsed neutron source

The neutrons that are used in scattering experiments are either produced in nuclear reactors or from accelerator-based sources; examples of the former would be the Institut Laue-Langevin in Grenoble and the Laboratoire Léon Brillouin near Paris, whilst ISIS in Oxfordshire and the Spallation Neutron Source (SNS) at Oak Ridge National Laboratory in the USA are instances of the latter. All of the neutron experiments in this work were performed at ISIS.

ISIS uses a linear particle accelerator to accelerate H^- ions to 70 MeV in 200 ms pulses before passing them through a 0.3 mm thick aluminium oxide foil that strips the two electrons from each ion, resulting in a proton beam. The beam is then injected into the synchrotron and accelerated to an energy of 800 MeV before extraction. The entire process is repeated 50 times a second and generates a proton current of $\sim 200 \mu A$.

The high-energy proton beam collides with a target made of the heavy metal tantalum. Collisions excite the nuclei in the target which then release energy by discharging neutrons (primarily), some of which will cause further collisions; approximately 15 neutrons are produced for every proton delivered to the target. These neutrons generally have very high energies and so pass through hydrogen-rich moderators to slow them to useful velocities. These moderators make use of the large scattering cross-section of hydrogen to slow down the neutrons by repeated collisions. The moderators used at ISIS are ambient temperature water (316 K), liquid methane (100 K) and liquid hydrogen (20 K), each of which provides a distinct spectral distribution of neutrons for different types of scattering experiment.

All neutron experiments in this work were carried out on the GEM (GEneral Materials) diffractometer [22] (Fig. 3-10) at ISIS. GEM uses a liquid methane moderator to obtain thermal neutrons, but the beam is under-moderated to prevent over-broadening of the pulse, giving a distinctive flux shape (Fig. 3-11). The path length from the moderator to the sample is relatively long (~ 17 m), giving a high resolution in reciprocal space but reducing the flux incident on the sample. For a disordered sample where intensity is spread across the entire Q -range, rather than being concentrated in Bragg peaks, the

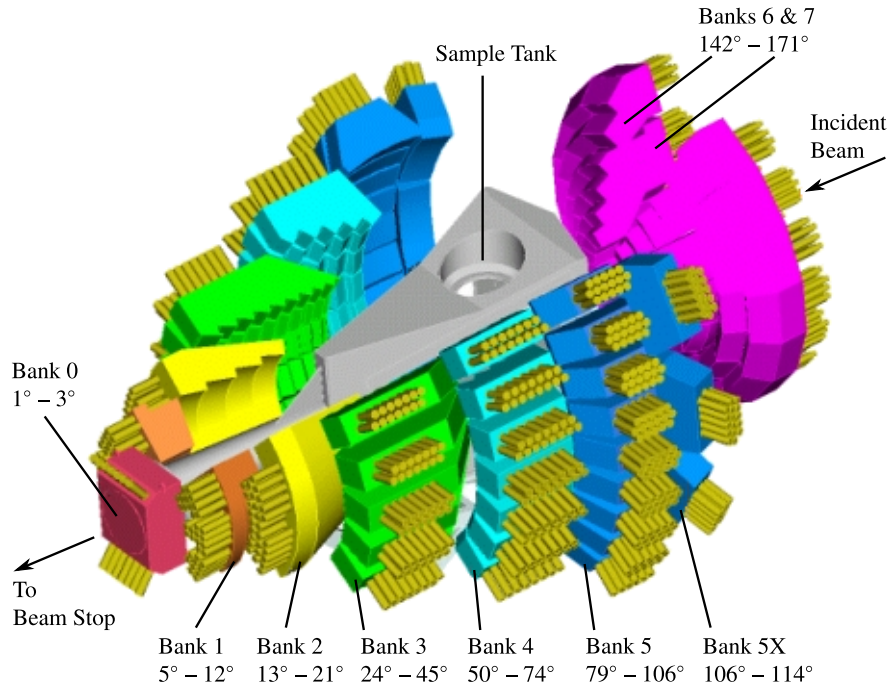


Figure 3-10 The layout of the GEM diffractometer. GEM has 7270 detectors over 8 banks covering the scattering angles from 1.21° to 171.4° , and an azimuthal angle range of $\pm 45^\circ$ [22].

lower flux is undesirable—however, the high Q resolution leads to less damping of the differential correlation function $D(r) (= T(r) - T_0(r))$ and thus a lower error on the coordination numbers measured from it [22]. The large detector area of the diffractometer helps to compensate for the long path length.

3.7.4 Data analysis

3.7.4.1 Extracting the distinct scattering

The neutron diffraction data obtained from an experiment on GEM require some corrections before the distinct scattering can be extracted; the GUDRUN program [23] and the ATLAS software suite [24] were used for processing the data. The GUDRUN manual [23] explains the various calculations and corrections in detail, so they shall be only briefly discussed here.

There are five stages to the corrections implemented by GUDRUN:

- Data from an empty chamber experiment are used to remove the background from all the data.

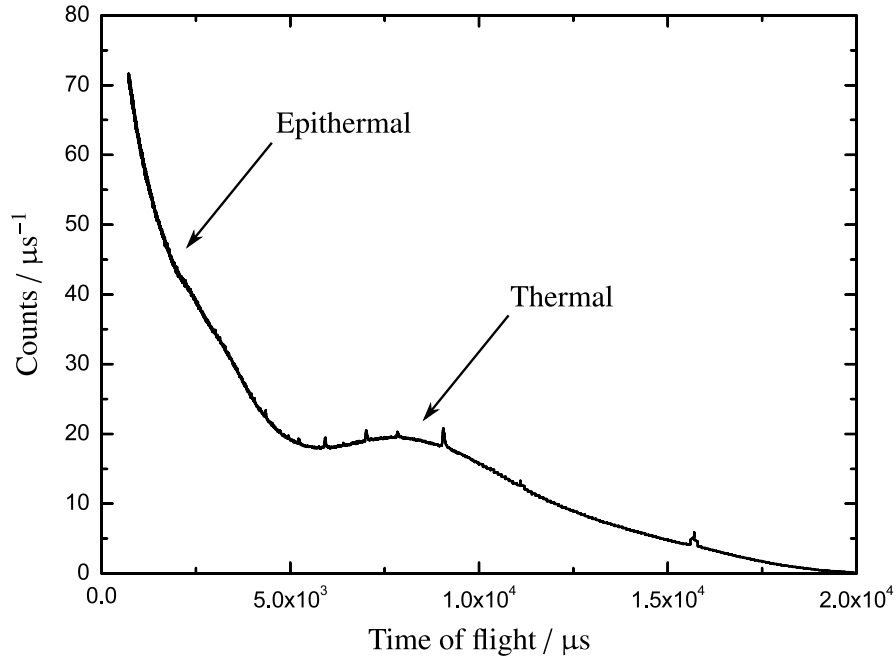


Figure 3-11 The flux of neutrons after they have been moderated using liquid methane at ~ 110 K. The data were taken using a vanadium rod on the GEM diffractometer. The contribution from epithermal and thermal neutrons are indicated.

- Scattering data from a vanadium rod are used to adjust the sample and vanadium can data for the flux.
- A correction for multiple scattering is made.
- Scattering from the can and attenuation effects are allowed for.
- Finally, the distinct scattering cross section, $i(Q)$, is absolutely normalised to the number of atoms in the sample.

$i(Q)$ from the raw data only covers a finite range in Q . At high Q the limit of usable data is typically 35 \AA^{-1} to 45 \AA^{-1} . At low Q the data extend down to $\sim 0.3 \text{ \AA}^{-1}$, below which the data need to be simulated. For a glass the data are extrapolated as a quadratic of the form $A + BQ^2$ down to $Q = 0$; for a crystal, a horizontal line might be more appropriate for the extrapolation.

3.7.4.2 The total correlation function

The total correlation function $T(r)$ (q.v. §3.7.2.7) is obtained from the distinct scattering by a Fourier transform (Eqn. (3-28)). The Lorch modification function [18]

(Eqn. (3-30)) damps the data at values near $Q = 0$ and $Q = Q_{\max}$ to reduce the effects of termination ripples caused by the finite Q range, but causes broadening of the peaks in $T(r)$. The peaks may be fitted with a Gaussian convoluted with the real space resolution, and from these fits coordination numbers, bond lengths and thermal widths can be extracted.

As discussed in §3.7.2.7, $T(r)$ is a weighted sum of the partial correlation functions between the different types of atom in the sample. At low r , the peaks that arise in $T(r)$ are attributable to individual partial correlations, and are usually well-separated: for example, in the $T(r)$ for $v\text{-SiO}_2$, as shown in Figure 3-9, the first peak arises solely from the Si–O correlation. Thus, by dividing by the appropriate weighting factor (see Equation (3-32)), the partial correlation function can be displayed over the limited range of r occupied by the particular non-overlapping peak. This can be used to normalise the peaks from samples of different compositions, permitting a comparison that can reveal any differences in bonding.

3.7.5 Experimental method

All of the neutron diffraction in this work was obtained using the GEM diffractometer [22] at the ISIS pulsed neutron source (*q.v.* §3.7.3). Glass samples, in the form of fragments and powder, were contained in vanadium cans of diameter 8.3 mm or 5 mm with walls of thickness 25 μm . The neutron beam size was 40 mm high by 15 mm wide. To allow for accurate corrections to be made, data were also collected for the empty chamber, an empty can and an 8 mm vanadium rod for each experimental period—data for a given glass system were typically obtained over several consecutive days, but separate systems were often measured months apart. Glass samples were typically measured until $\sim 1000 \mu\text{A h}$ of accumulated data had been collected.

References

- [1] R. G. Orman and D. Holland, *J. Solid State Chem.* **180** (9), (2007), 2587–2596.
- [2] R. G. Orman, *Phase Transitions in Antimony Oxides and Related Glasses*, MSc Thesis, University of Warwick (2005).
- [3] Inorganic Crystal Structure Database, Chemical Database Service, Daresbury Laboratory (2009), <http://cds.dl.ac.uk/cds/cds.shtml>.
- [4] C. V. Raman and K. S. Krishnan, *Nature* **121**, (1928), 501–502.
- [5] P. McMillan, *Am. Mineral.* **69**, (1984), 622–644.
- [6] C. N. Banwell, *Fundamentals of Molecular Spectroscopy* (McGraw-Hill, 1983), 3rd ed.
- [7] K. Nakamoto, *Infrared and Raman Spectra of Inorganic and Coordination Compounds (Part A: Theory and Applications in Inorganic Chemistry)* (Wiley-Interscience, 1997), 5th ed.
- [8] J. Chadwick, *J. Roy. Soc. Proc.* **136**, (1932), 692–708.
- [9] G. L. Squires, *Introduction to the Theory of Thermal Neutron Scattering* (Dover Publications Inc., Mineola, New York, 1996).
- [10] A. C. Hannon, in: *Encyclopedia of Spectroscopy and Spectrometry*, edited by J. Lindon, G. Tranter and J. Holmes (AP, London, 2000), vol. 2, pp. 1479–1492.
- [11] A. C. Wright, *Experimental Techniques of Glass Science* (The American Ceramic Society, 1993), chap. 8, pp. 205–314.
- [12] K. Sköld and D. L. Price (eds.), *Methods of Experimental Physics: Neutron Scattering*, vol. 23A (Academic Press Inc., London, 1986).
- [13] V. F. Sears, *Neutron News* **3** (3), (1992), 26–37.
- [14] E. Fermi, *Ric. Sci.* **7** (2), (1936), 13–52.
- [15] G. Breit, *Phys. Rev.* **71**, (1947), 215–231.
- [16] G. Placzek, *Phys. Rev.* **86**, (1952), 377–388.
- [17] E. R. Barney, (personal communication) (2008).

- [18] E. Lorch, *J. Phys. C Solid State* **2** (2), (1969), 229–237.
- [19] L. Van Hove, *Phys. Rev.* **95** (1), (1954), 249–262.
- [20] A. C. Hannon and J. M. Parker, *J. Non-Cryst. Solids* **274**, (2000), 102–109.
- [21] N. E. Brese and M. O’Keeffe, *Acta Crystallogr. B* **47**, (1991), 192–197.
- [22] A. C. Hannon, *Nucl. Instrum. Meth. A* **551** (1), (2005), 88–107.
- [23] S. E. McLain, D. Bowron, A. C. Hannon and A. K. Soper, *GUDRUN: A computer program developed for analysis of neutron diffraction data* (2006).
- [24] A. C. Hannon, W. S. Howells and A. K. Soper, *Inst. Phys. Conf. Ser.* **107**, (1990), 193–211.

Chapter 4

Antimony Oxide and Oxychloride Glasses

4.1 Sample preparation and characterisation

An attempt was made to prepare antimony oxide glass through roller-quenching of the melt: this method offers a significantly higher cooling rate ($\sim 10^5 \text{ }^\circ\text{C s}^{-1}$) than other methods, such as splat-quenching ($\sim 10^3 \text{ }^\circ\text{C s}^{-1}$). 8.5 g of Sb_2O_3 (99.6 %, Alfa Aesar) in a lidded platinum crucible was placed in a furnace that had been pre-heated to $1000 \text{ }^\circ\text{C}$, left for ~ 8 min until molten, then roller-quenched between two stainless steel rollers counter-rotating at several hundred revolutions per minute. The gap between the rollers was $\sim 18 \text{ }\mu\text{m}$ and a stainless steel pan was used to collect the resulting, brittle glass fragments. These were manually sorted into groups by appearance: $\sim 10 \%$ were clear and transparent, $\sim 20 \%$ were yellow and opaque, and the remainder were a cloudy white. This material is later referred to as the “ Sb_2O_3 glass” for convenience, but this should not necessarily be taken as the actual chemical formula of the glass.

Antimony oxychloride glass was prepared from crystalline onoratoite. The latter was synthesised by a method similar to that of Matsuzaki *et al.* [1]: 20 g of SbCl_3 (99 %, Sigma-Aldrich) were hydrolysed with 200 ml of distilled H_2O at $35 \text{ }^\circ\text{C}$ and stirred thoroughly until the crystals had dissolved. The flocculent precipitate was then suction-filtered and the residue washed with diethyl ether before being left to stand for 60 h to allow any remaining ether to evaporate (subsequent experiments have determined 24 h to be sufficient). The resulting material was placed in a drying oven at $80 \text{ }^\circ\text{C}$ for 1 h before being heated to $440 \text{ }^\circ\text{C}$ under nitrogen in a platinum crucible and held for 4 h at that temperature before being allowed to cool to $50 \text{ }^\circ\text{C}$ for retrieval. X-ray diffraction confirmed the sample to be single-phase onoratoite (Fig. 4-1).

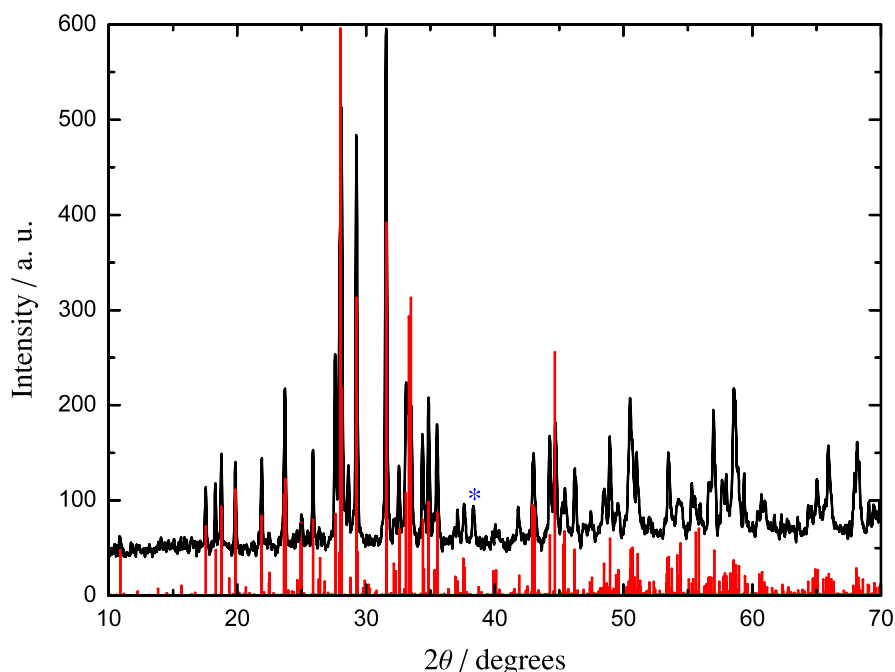


Figure 4-1 The X-ray diffraction pattern of the synthesised crystalline onoratoite, $\text{Sb}_8\text{O}_{11}\text{Cl}_2$. Red lines are calculated peak positions from the single-crystal study of Mayerová *et al.* [2]. The starred peak is from the aluminium sample holder.

To prepare the glass, a sample of the crystalline onoratoite in a lidded alumina crucible was placed into a furnace at 1100°C and left for ~ 10 min before being splat-quenched between two cooled copper plates, resulting in a pale yellow, translucent glass. For convenience, this sample is subsequently referred to as the “ $\text{Sb}_8\text{O}_{11}\text{Cl}_2$ glass” (based on the use of onoratoite as the precursor), but this should not necessarily be taken as indicative of the actual chemical formula.

X-ray diffraction was used to determine that only the clear, transparent flakes of Sb_2O_3 glass were in fact fully amorphous (Fig. 4-2a), whilst the cloudy white portions contained some crystalline material and the opaque yellow fragments were fully crystalline—only the completely vitreous material was used in all subsequent measurements. The $\text{Sb}_8\text{O}_{11}\text{Cl}_2$ glass was also confirmed to be fully amorphous within the limits of detection ($\sim 5\%$) (Fig. 4-2b). EDX measurements of the oxychloride samples, taken over three different areas of a powdered sample, gave a mean value of $9(1)\%$ chlorine in the onoratoite crystal (in line with the 9.5% predicted from the chemical formula) but only $6(1)\%$ in the $\text{Sb}_8\text{O}_{11}\text{Cl}_2$ glass. The spectra of both the oxide and oxychloride glasses showed no detectable contaminants, such as aluminium from the crucible used

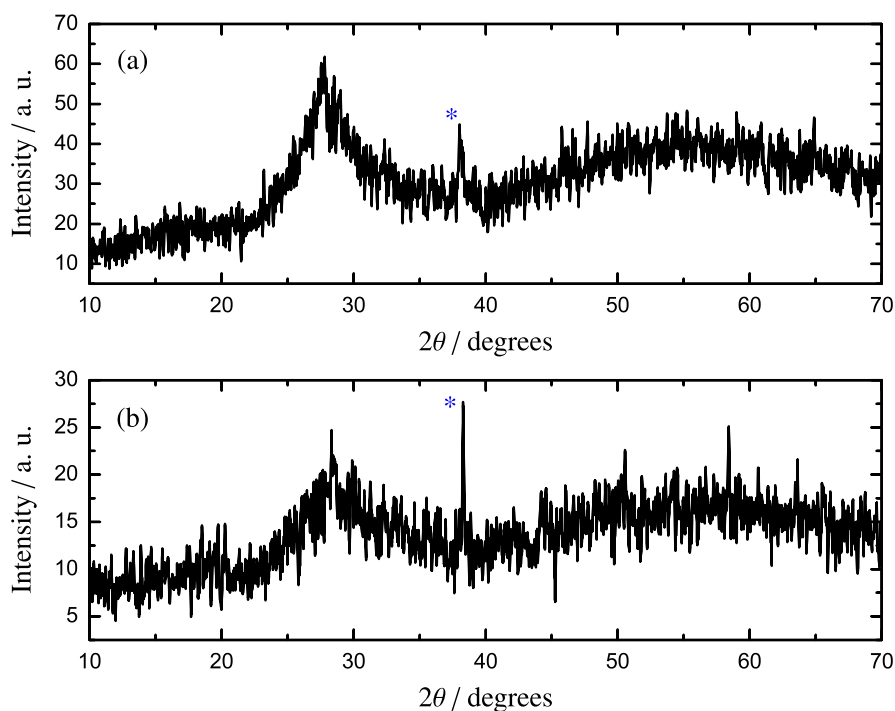


Figure 4-2 The XRD patterns of (a) the Sb_2O_3 glass, and (b) the $\text{Sb}_8\text{O}_{11}\text{Cl}_2$ glass. The starred peaks are from the aluminium sample holders.

for the $\text{Sb}_8\text{O}_{11}\text{Cl}_2$ glass sample.

Raman spectra of the Sb_2O_3 (Fig. 4-3) and $\text{Sb}_8\text{O}_{11}\text{Cl}_2$ (Fig. 4-4) glasses and the related crystals were obtained, with the comparison of the oxychloride samples appearing to demonstrate that all of the major crystal bands are represented in the glass data, albeit broadened significantly by the disorder in the system. The $\text{Sb}_8\text{O}_{11}\text{Cl}_2$ glass spectrum is also very similar to that previously reported for an Sb_2O_3 – SbCl_3 glass [3], although there are some small differences in the 245 cm^{-1} to 310 cm^{-1} region and features $\leq 245\text{ cm}^{-1}$ are less intense in the $\text{Sb}_8\text{O}_{11}\text{Cl}_2$ glass. Whilst studying the Sb_2O_3 – SbCl_3 glass, Orman [3] noted that age-related effects were observed in the thermal behaviour of the sample and speculated that these were related to the introduction of hydroxyl groups from interaction with atmospheric moisture—this may be the cause of the differences between the Raman spectra of the two glasses, since the $\text{Sb}_8\text{O}_{11}\text{Cl}_2$ glass was measured within days of being made, whilst the Sb_2O_3 – SbCl_3 glass was stored for several months before Raman measurements were taken.

Mössbauer spectroscopy was performed at 77 K on the previous Sb_2O_3 – SbCl_3 glass, as well as onoratoite and cervantite, by Dr Mike Thomas at the University of Liverpool. These measurements showed no detectable Sb^{5+} in either the glass or the oxychloride

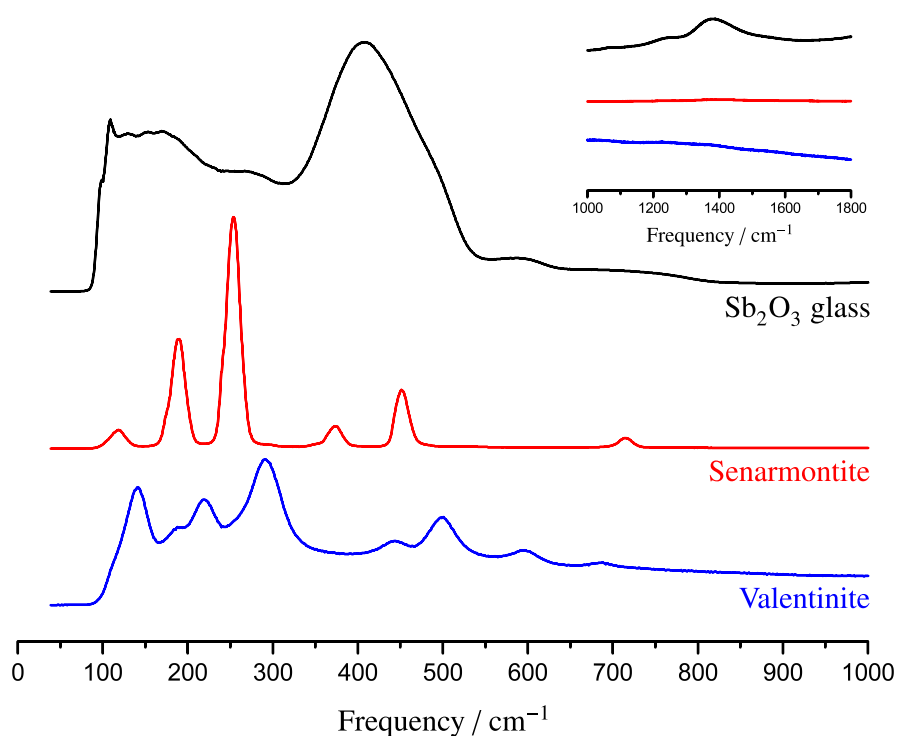


Figure 4-3 Polarised Raman spectra obtained for the Sb_2O_3 glass, commercial senarmontite (as used for the glass-making) and mechanically-derived valentinite (from a previous study [3]). The laser source had a wavelength of 785 nm.

crystal, whilst the cervantite sample was shown to contain the expected 1:1 ratio of Sb^{3+} to Sb^{5+} [4, 5].

4.2 Thermal analysis

4.2.1 Antimony oxide glass

Simultaneous TGA and DSC measurements were taken of the crystalline onoratoite and both glasses, over a temperature range of 30 °C to 800 °C at a heating rate of 10 °C min⁻¹ under dry nitrogen. Platinum crucibles were used for the samples, whilst an empty alumina crucible was used as the reference. The Sb_2O_3 glass exhibits clear glass transition and crystallisation events, at 250(2) °C and 303(2) °C respectively, which compare well with the values of 245 °C and 296 °C reported previously by Bednarik and Neely [6] for a silica-contaminated Sb_2O_3 glass. Following these events there is a positive slope as the crystallised Sb_2O_3 begins to volatilise before melting (Fig. 4-5). It is not clear if a senarmontite-valentinite transition occurs before the sample melts, and unfortunately

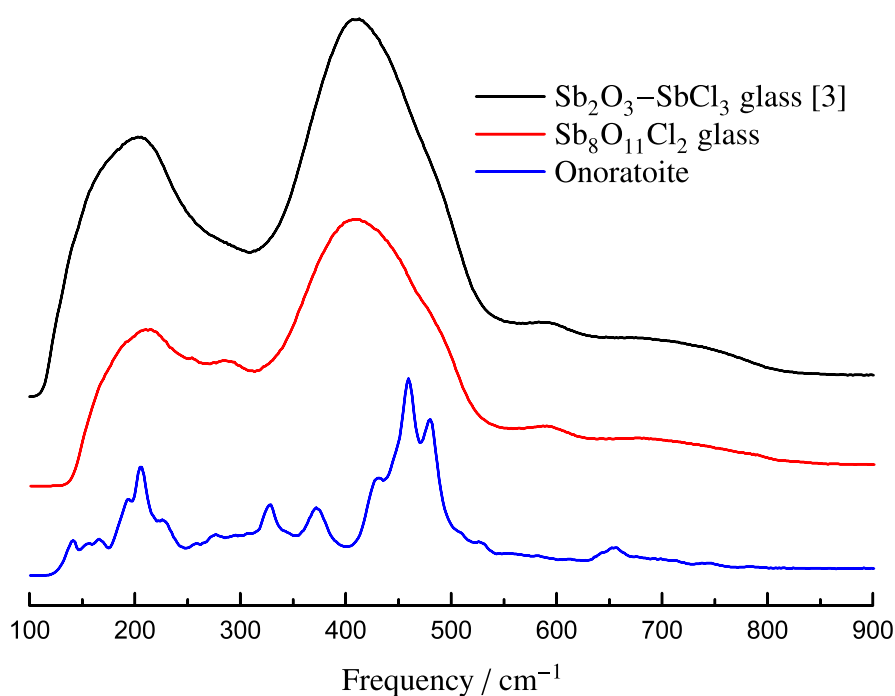


Figure 4-4 Unpolarised Raman spectra obtained for the oxychloride crystal and glass samples, compared with the data previously gathered for the $\text{Sb}_2\text{O}_3\text{-SbCl}_3$ glass [3]. The laser source had a wavelength of 514 nm and spectra were initially obtained over the full range available (100 cm^{-1} to 3200 cm^{-1}) before being baseline subtracted. No features are present in the spectra beyond 900 cm^{-1} .

there was insufficient sample to analyse the crystallisation products by XRD. Therefore, the glass may crystallise to either senarmonite or valentinite, or a mixture of the two, whilst the fact that mass remained after volatilisation and melting may suggest that a small quantity of cervantite is also formed during crystallisation.

0.5841 mg of material remained after the thermal program: if this is assumed to have been entirely Sb_2O_4 , then 1.90×10^{-6} mol of the substance—or twice as many antimony atoms, half of which are Sb^{5+} —were present. The initial mass of $\nu\text{-Sb}_2\text{O}_3$ was 6.49 mg and thus contained 4.45×10^{-5} mol of Sb atoms, so the Sb^{5+} present after the TGA/DSC run would suggest that 4.3 % of the antimony in the glass is Sb^{5+} . However, the reducing conditions of the experiment may have lowered the oxidation state of some Sb^{5+} that was initially present in the glass, whilst it is also possible that limited oxidation has occurred: a previous study [7] also observed cervantite formation after thermal analysis of the crystalline Sb_2O_3 polymorphs under reducing conditions, the authors speculating that this might be due to chemisorbed, or physically absorbed, water. Therefore the amount of Sb^{5+} present in the glass cannot be accurately determined

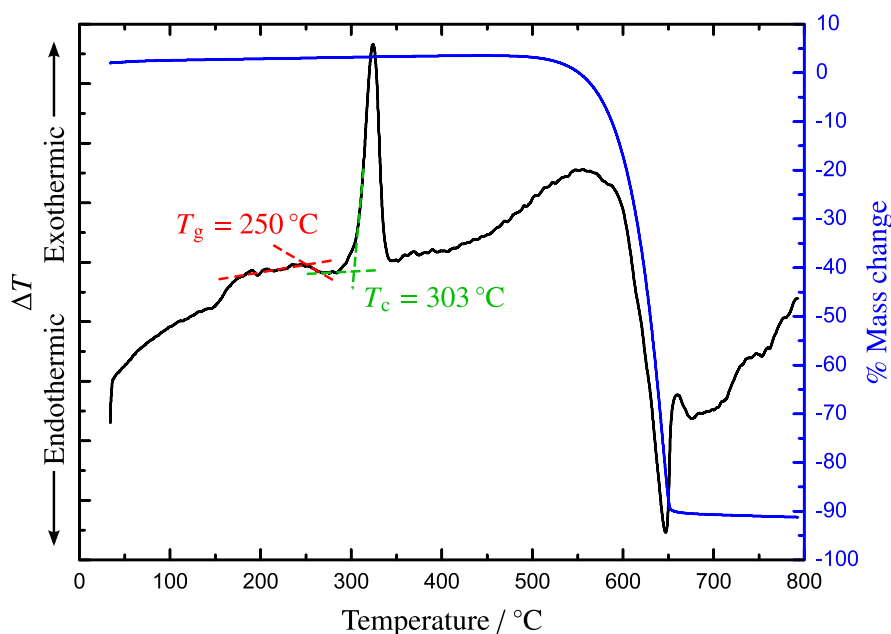


Figure 4-5 TGA/DSC data for the Sb_2O_3 glass under nitrogen, at a heating rate of $10^{\circ}\text{C min}^{-1}$ in a platinum crucible. An empty alumina crucible was used as the reference. The amount of noise in the data is probably a result of the limited sample mass available for the measurement.

by this method.

4.2.2 Antimony oxychloride glass

The $\text{Sb}_8\text{O}_{11}\text{Cl}_2$ glass appears to exhibit two glass transition temperatures (Fig. 4-6), but earlier work on antimony oxychloride glass found that this effect was only observed when heating a powdered sample, as opposed to a fragment of the glass, suggesting that a sintering process is taking place in the devitrified glass before crystallisation [3]. The glass transition and crystallisation temperatures measured were $278(2)^{\circ}\text{C}$ and $318(2)^{\circ}\text{C}$, respectively.

Based on previous work, the $\text{Sb}_8\text{O}_{11}\text{Cl}_2$ glass can be expected to crystallise primarily to onoratoite and senarmontite, with a small quantity of valentinite [3]. The DSC data for the $\text{Sb}_8\text{O}_{11}\text{Cl}_2$ crystal and glass are therefore quite similar, as shown in Figure 4-7. Except for the glass transition and crystallisation events already discussed, the principal thermal features are labelled.

The feature at “A”, onset $351(2)^{\circ}\text{C}$, which is only visible in the crystal data, is believed to be an artifact of the equipment. The event “B”, commencing at $501(2)^{\circ}\text{C}$, is much larger in the crystal data and coincides with a change in the rate of mass loss (see

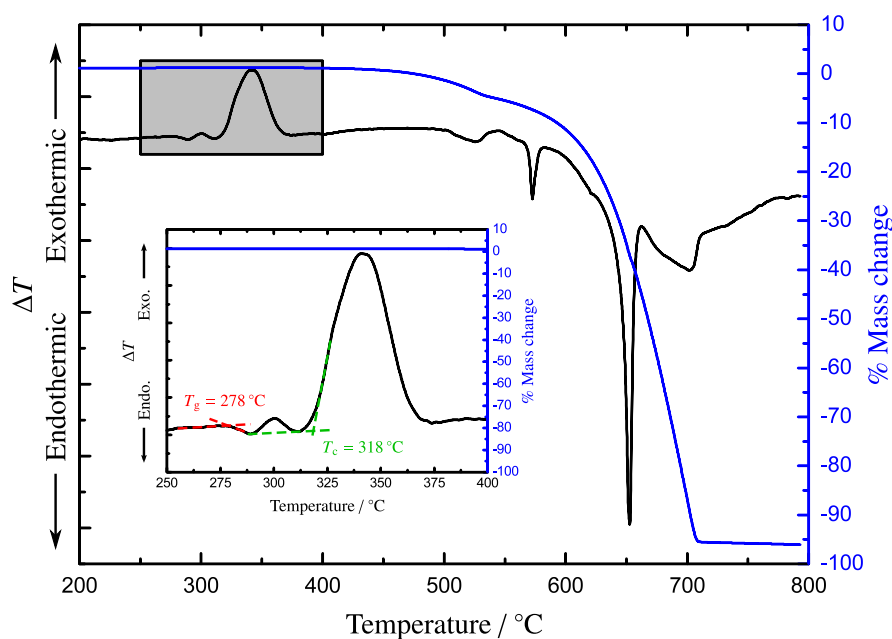


Figure 4-6 TGA/DSC data for the $\text{Sb}_8\text{O}_{11}\text{Cl}_2$ glass under nitrogen, at a heating rate of $10^\circ\text{C min}^{-1}$ in a platinum crucible. An empty alumina crucible was used as the reference. The shaded portion of the main graph, showing the glass transition and crystallisation, is expanded for clarity.

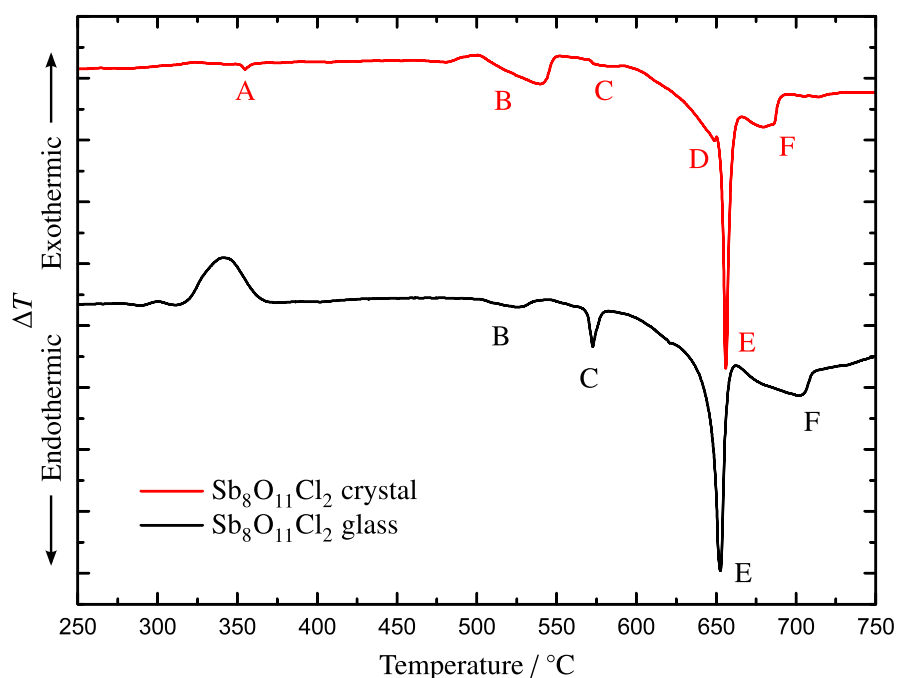


Figure 4-7 Comparison of DSC data obtained for the $\text{Sb}_8\text{O}_{11}\text{Cl}_2$ glass and crystal samples under nitrogen, at a heating rate of $10^\circ\text{C min}^{-1}$ in platinum crucibles. An empty alumina crucible was used as the reference. For this plot the data have been normalised with respect to the initial sample mass.

Figure 4-6 for mass change data), strongly suggesting that it corresponds to the decomposition of onoratoite to senarmontite and $\text{SbCl}_{3(g)}$ [8]. The cause of the thermal event at “C” (onset 567(2) °C) is ambiguous: it may be a greatly depressed senarmontite-valentinite phase transition, perhaps due to the presence of the chlorine in the sample. However, the previous study by Orman [3] did not observe the breakdown of onoratoite to occur at “B”, but instead much closer to 570 °C, suggesting that the samples studied here in fact undergo two distinct decomposition events. The work of Belluomini *et al.* [8], who report decomposition occurring in the range 470 °C to 540 °C, would seem to support this theory, although the absence of an obvious change in the rate of mass loss at “C” is inconsistent with this interpretation. The different strengths of the events at “B” and “C” between the crystal and glass may be related to the lower chlorine content of the latter (*q.v.* §4.1).

Event “D” (onset is ambiguous, peak maximum occurs at 648(2) °C) is only distinguishable in the crystal data, but probably also occurs in the glass, based on the asymmetry of the subsequent peak “E”, and is consistent with temperatures reported for the senarmontite-valentinite transition [7, 9]. The strongly endothermic peak at “E”, maximum at 654(2) °C, can be clearly assigned to Sb_2O_3 melting, whilst the feature at “F” represents the end of Sb_2O_3 sublimation (and evaporation, after melting) which began at approximately the same temperature as event “B”, as shown by the negative gradient to the slope from that point forward. The material, amounting to ~4 % of the initial sample mass, that remains after “F” (Fig. 4-6, and similarly for the crystal) is probably a small quantity of cervantite, analogous to that observed in the Sb_2O_3 glass TGA/DSC (Fig. 4-5). Presuming the glass to have the chemical formula of onoratoite ($\text{Sb}_8\text{O}_{11}\text{Cl}_2$) and the amount of Sb^{5+} to remain unchanged, this would indicate that 2.0 % of the antimony atoms in the glass are at the higher oxidation state. However, the same caveats discussed earlier still apply (*q.v.* §4.2.1)—in addition, EDX analysis indicated significantly less chlorine to be present in the glass than in crystalline onoratoite (*q.v.* §4.1), suggesting that the chemical formula of the glass is different to that used for the calculation.

4.3 Density measurements

A density of $5.27(2) \text{ g cm}^{-3}$ was measured for the Sb_2O_3 glass, which can be compared with densities of $5.57(2) \text{ g cm}^{-3}$ and $5.66(2) \text{ g cm}^{-3}$ measured for samples of senarmontite and valentinite, respectively—these latter were the commercial Sb_2O_3 used for the glass-making, shown by XRD to be pure senarmontite [7], and the valentinite obtained previously by the mechanical milling method of Berry and Ren [10], which X-ray diffraction had also shown to be single phase [7]. This glass density is significantly higher than previously reported for attempts at Sb_2O_3 glass, which are typically between 5.05 g cm^{-3} and 5.105 g cm^{-3} [11–14], being closest to the value of 5.179 g cm^{-3} given by Kordes [15], but this may be expected since most previous samples have contained some contamination (*q.v.* §2.2). That the glass density is lower than those of the two Sb_2O_3 polymorphs is understandable, since the amorphous structure should be expected to pack less well than the crystal formations, even if the vitreous network is based on one of the two crystalline phases.

The density of the crystalline onoratoite was measured to be $5.45(2) \text{ g cm}^{-3}$: this is in line with reports in the literature, where a value of 5.3 g cm^{-3} had previously been measured by Belluomini *et al.* [8], along with a calculated density of 5.49 g cm^{-3} , whilst other authors determined values of 5.425 g cm^{-3} [16] and 5.43 g cm^{-3} [2] from their single-crystal XRD data. A density of $5.10(2) \text{ g cm}^{-3}$ was measured for the $\text{Sb}_8\text{O}_{11}\text{Cl}_2$ glass, which is close to the value of 5.05 g cm^{-3} reported by Johnson *et al.* [14] for an Sb_2O_3 glass that later work showed to contain 6(2) at.% chlorine [3].

4.4 Neutron diffraction

4.4.1 Antimony oxide glass

The signal-to-noise ratio in the neutron diffraction data collected for the antimony oxide glass sample was sufficient to conduct a Fourier transform to real-space up to $Q_{\text{max}} = 35 \text{ \AA}^{-1}$ —this was quite limited considering the length of the experiment, but was probably due to the poor packing efficiency and limited quantity of glass flakes produced from roller-quenching ($\sim 4.21 \text{ g}$), resulting in a low effective density of sample in the neutron beam ($\sim 1.079 \text{ g cm}^{-3}$). The total correlation function, $T(r)$, obtained for the

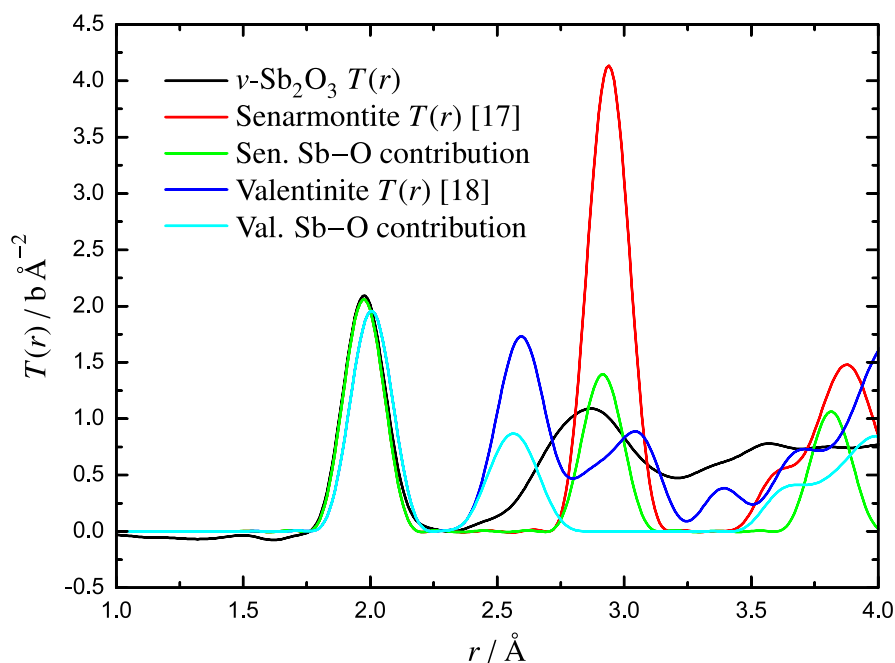


Figure 4-8 The total correlation function $T(r)$ for the Sb_2O_3 glass, compared with simulated correlation functions from the two crystalline polymorphs of Sb_2O_3 , senarmontite [18] and valentinite [19]. Also shown are the Sb–O contributions to the crystal correlation functions.

glass is shown in Figure 4-8, as well as simulated data for the two crystalline Sb_2O_3 polymorphs, senarmontite and valentinite, generated using the XTAL program [17].

The first peak in the correlation function, at ~ 1.98 Å, is well-defined and exhibits a small degree of asymmetry. Compared with the two crystalline polymorphs of Sb_2O_3 , this suggests that the $[\text{SbO}_3]$ trigonal pyramids found in senarmontite, which have an Sb–O length of 1.977 Å [18], are the closer match to the units present in the glass. However, the double-chain structure of valentinite would appear better suited to forming the ‘continuous random network’ expected of a glass. The majority of earlier work on Sb_2O_3 glasses (with small amounts of SiO_2 or B_2O_3 contamination) concluded that the structure was similar to valentinite, based on evidence from XRD, and IR or Raman spectroscopy [11, 13, 20], and it may be possible that the double-chain structure of the crystal is retained in the glass, with shorter Sb–O bond lengths (due to the relaxation of the requirement for regular atomic ordering): if so, this should be indicated by a smaller O–Sb–O angle.

The second peak at ~ 2.85 Å is considerably broader since it covers both the first O···O and the second Sb···O correlations (senarmontite has a second Sb···O distance of

2.92 Å, whilst valentinite has 2.52 Å and 2.62 Å). Here again it is not straightforward to rule out either crystalline polymorph as a basis for the short-range structure in the glass, since the wide distribution of bond lengths covers both possibilities. However, the lack of intensity on the smaller- r side of the peak suggests that any valentinite-type structures are in the minority, particularly if the Sb–O distance has relaxed as suggested above, since this should only bring the oxygen atoms closer together.

Comparisons of the measured data with simulated correlation functions for cervantite (Sb_2O_4) [4] (Fig. 4-9) and Sb_2O_5 [21] (Fig. 4-10), suggest that these crystals may bear more resemblance to the glass structure than the exclusively trigonal pyramidal arrangements found in crystalline Sb_2O_3 . Both Sb_2O_4 and Sb_2O_5 incorporate Sb^{5+} ions as $[\text{Sb}^{5+}\text{O}_6]$ octahedra with six bonds of varying length, which result in a broad Sb–O peak that does not agree as well with the glass $T(r)$ as the Sb_2O_3 crystals do. However, it is conceivable that in removing the requirement for long-range structural order, more regular polyhedra might be found in the glass, leading to a narrower Sb–O peak. Alternatively, the structure of Sb_2O_4 also contains $[\text{Sb}^{3+}\text{O}_4]$ pseudo-trigonal bipyramids with pairs of bonds at ~ 2.02 Å and ~ 2.23 Å, which may explain the asymmetry on the greater- r side of the Sb–O peak in the glass $T(r)$. Finally, the position of the combined first O···O / second Sb···O peak is also well-matched by both Sb_2O_4 and Sb_2O_5 , although the intensities differ from the glass.

Therefore, comparison with the crystalline antimony oxides suggests that the glass contains at least some four-coordinated Sb^{3+} and/or six-coordinated Sb^{5+} . Unfortunately, Mössbauer data was not obtained for the Sb_2O_3 glass, so the proportion of Sb^{5+} present in the sample is unknown—based on the data obtained for the antimony borate (*q.v.* §5.1) and antimony silicate (*q.v.* §6.1) systems, the amount could be predicted to be at least 10 % to 20 % of the antimony present in the glass, although this is unlikely to be an accurate estimate due to the different redox conditions in the glass melts.

The O···O peak in the glass $T(r)$ is quite broad and asymmetric, probably due to overlapping secondary and tertiary Sb···O correlations (as in cervantite, *q.v.* Fig. 4-9), which makes fitting difficult. However, by considering the FWHM points of both this peak and that which arises from the first Sb–O correlation, an O–Sb–O angular range of 79.4° to 106.7° can be calculated. This range is quite broad, and covers all of the typical units found in the crystalline antimony oxides, however the average value of

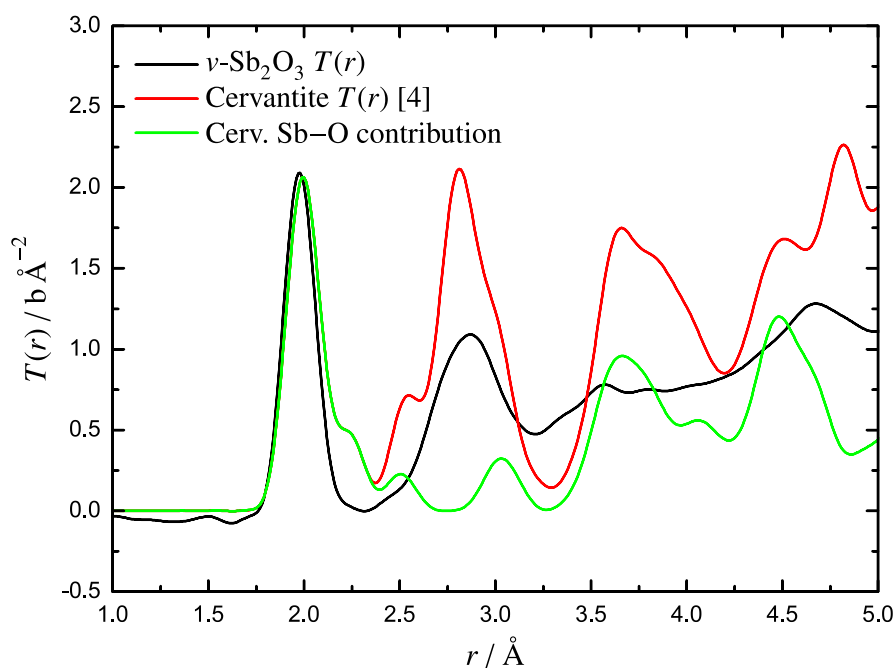


Figure 4-9 $T(r)$ of the Sb_2O_3 glass compared with simulated correlation functions for crystalline cervantite (Sb_2O_4) [4]. Also shown is the Sb–O contribution to the crystal correlation function.

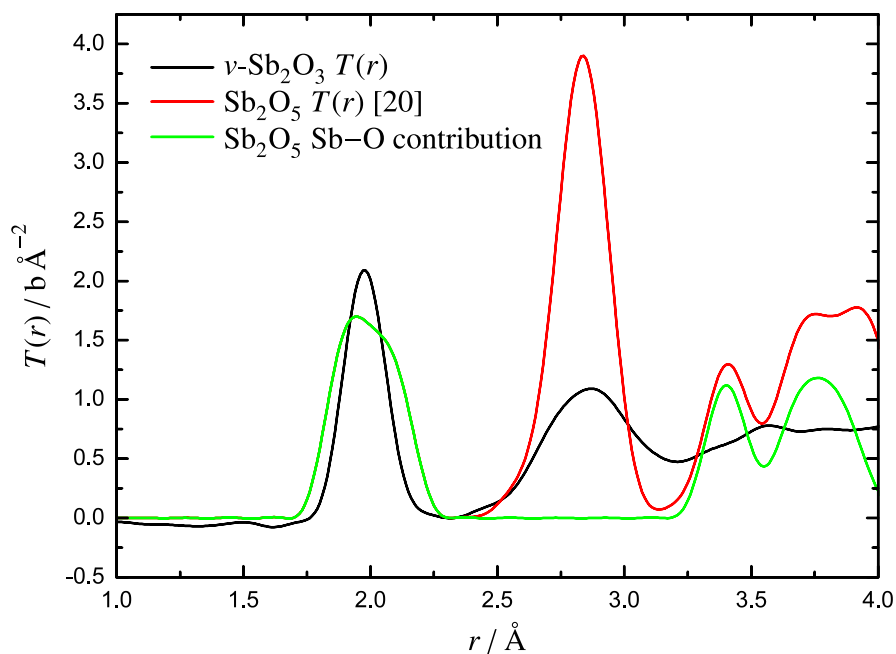


Figure 4-10 $T(r)$ of the Sb_2O_3 glass compared with simulated correlation functions for crystalline Sb_2O_5 [21]. Also shown is the Sb–O contribution to the crystal correlation function.

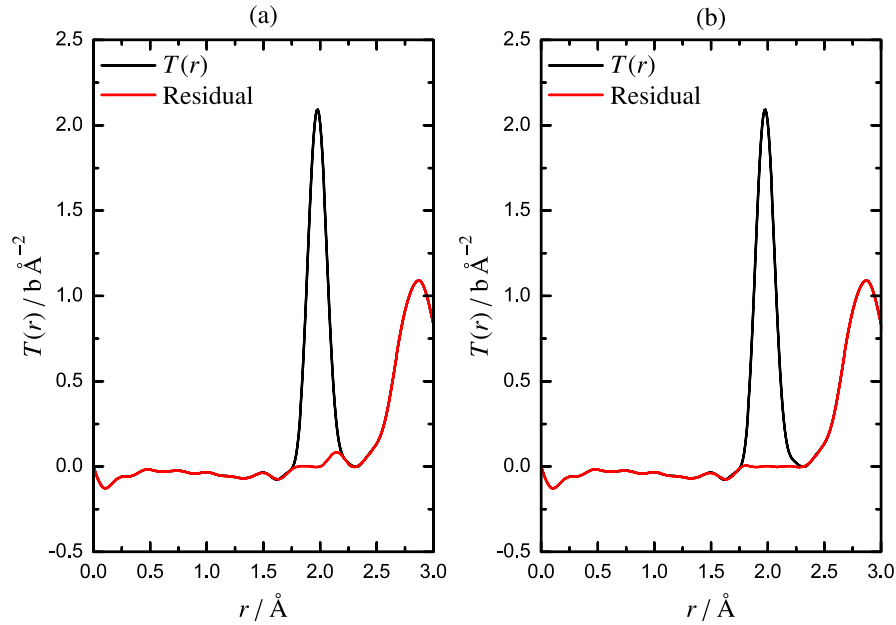


Figure 4-11 The residuals of (a) single- and (b) double-peak fits to the first Sb–O correlation for the Sb_2O_3 glass.

93.1° is in good agreement with the angles previously obtained by Imaoka *et al.* [22] and Hasegawa *et al.* [11] from X-ray diffraction. This average value is also higher than that to be expected from a ‘relaxed valentinite’ structure with shorter Sb–O bond lengths, as suggested earlier.

To obtain a coordination number, the first Sb–O correlation was initially fitted with a single peak, but examination of the residual demonstrated that a second peak was also present (Fig. 4-11a). To fit two peaks in such close proximity it was necessary to constrain the RMS deviations to be the same for both peaks, which is only an approximation since longer bond lengths should result in weaker bonds and higher deviations for the same pair of atoms. The two-peak fit resulted in a much improved residual (Fig. 4-11b) with peak positions $r_{\text{SbO}(1)} = 1.972(1) \text{ \AA}$ and $r_{\text{SbO}(2)} = 2.092(4) \text{ \AA}$, and coordination numbers $n_{\text{SbO}(1)} = 2.99(2)$ and $n_{\text{SbO}(2)} = 0.25(2)$. The total coordination number is similar to the value of 3.15 reported by Hasegawa *et al.* [11] for an Sb_2O_3 glass stabilised with 5 mol% B_2O_3 , obtained by fitting a single peak at 1.99 \AA .

The position of the second Sb–O peak is consistent with bond-valence predictions for four-coordinated Sb^{3+} [23, 24]: if it is assumed that this peak results from all four bonds in the $[\text{Sb}^{3+}\text{O}_4]$ units being of this length, then the coordination number indicates that 6.3(5) % of the antimony in the glass exists in such units. In this case, the

coordination number resulting from the first peak is too high for the remaining antimony atoms to occur only in $[\text{SbO}_3]$ trigonal pyramids—a value of 2.81(2) would be expected. Therefore a portion of the antimony atoms that are not four-coordinated at $r_{\text{SbO}(2)}$ must be bonded to four or more oxygen atoms at $r_{\text{SbO}(1)}$: the most obvious candidate is six-coordinated Sb^{5+} , which bond-valence calculations would predict to have a bond length of 2.009 Å [23, 24]; such octahedra are found in crystalline Sb_2O_4 [4, 5] and Sb_2O_5 [21] with slightly shorter bonds. The coordination number for the first peak then arises from the equation

$$3(x - a) + 6(1 - x) = 2.99 \quad (4-1)$$

where x is the fraction of antimony that is Sb^{3+} and a is the fraction (≈ 0.063) of Sb^{3+} atoms present in $[\text{SbO}_4]$ units (at greater r). This solves to give $x = 0.941(7)$, meaning that 5.9(7) % of the antimony atoms in the glass would need to be Sb^{5+} to achieve the observed coordination number. Since this amount is the same (within error) as the proportion of four-coordinated Sb^{3+} , if this model is correct it may indicate that the ‘ $v\text{-Sb}_2\text{O}_3$ ’ is more accurately amorphous $y\text{Sb}_2\text{O}_3 \cdot (1 - y)\text{Sb}_2\text{O}_4$ where $y = x - a \approx 0.876(4)$ (from the overlap of the Sb^{5+} and four-coordinated Sb^{3+} values, assuming the two actual amounts to be equal).

In the absence of any data on the amount of Sb^{5+} in the glass, there are two other models that could also give rise to the values measured. If there is little or no Sb^{5+} in the glass, then $[\text{Sb}^{3+}\text{O}_4]$ units that have a 3+1 geometry—such that they are three-coordinated at $r_{\text{SbO}(1)}$ with a fourth bond length at $r_{\text{SbO}(2)}$ —would be consistent with the coordination numbers measured, with 25(2) % of the Sb^{3+} present in this configuration. Such units are not seen in the crystalline antimony oxides, but similar arrangements are present in the Mayerová model of onoratoite (*q.v.* §2.3) and TeO_2 glasses [25]. Alternatively, if there is more Sb^{5+} present than considered above, no $[\text{Sb}^{3+}\text{O}_4]$ units are needed: instead, $[\text{Sb}^{5+}\text{O}_6]$ octahedra that are more similar to those in crystalline Sb_2O_5 may be present. These have a range of bond lengths (*q.v.* §2.1) that would result in the antimony atom being three-coordinated at $r_{\text{SbO}(1)}$ with the three longer bonds added at progressively greater r to make up the contribution from the second Sb–O peak. However, from the value of $n_{\text{SbO}(2)}$, this would only account for, at most, 9 % of the antimony in the glass being Sb^{5+} : from the neutron data this would appear to be the maximum amount that may be present in the glass.

In summary, as demonstrated in Figure 4-9, the Sb_2O_4 structure is somewhat similar to that of the glass, whilst the two Sb_2O_3 polymorphs are quite different beyond the first Sb–O correlation (Fig. 4-8). Thus it would appear that the $[\text{SbO}_3]$ units form a network that is unlike that of either senarmontite or valentinite. A possible model for this structure is discussed in the next section, where the oxide and oxychloride glasses are compared.

4.4.2 Antimony oxychloride glass

The data obtained for the $\text{Sb}_8\text{O}_{11}\text{Cl}_2$ glass were good enough to allow a Fourier transform to real-space with a Q_{max} of 40 \AA^{-1} , whilst the onoratoite crystal data, being collected over a shorter period, were only useful to a Q_{max} of 27.4 \AA^{-1} . Simulated crystal correlation functions for the onoratoite model proposed by Menchetti *et al.* [16] were generated using the XTAL program [17], and a comparison with the neutron data shows that there is a significant deviation from the predicted Sb–O and O...O correlations (Fig. 4-12). The Menchetti model predicts that half of the Sb–O separations are $\sim 2.2 \text{ \AA}$, corresponding to the links along the basic ladder structure (Fig. 4-13), whilst the perpendicular Sb–O ‘rungs’ of the ladder are $\sim 2.0 \text{ \AA}$. This leads to roughly equivalent peaks in the correlation function centred at 2.0 \AA and 2.2 \AA , however the neutron diffraction data show that the majority of the Sb–O separations are of the shorter variety, with only a small proportion of longer bonds. The shortest O...O distance predicted by Menchetti *et al.*, arising from the oxygen atoms in the plane of the ladder, is also noticeably shorter than that actually observed (the second O...O peak arises from the interaction between the intra-ladder and the inter-ladder oxygen atoms). These two disagreements suggest that the ladder structure is actually distorted beyond the simple repeating structure of the Menchetti model.

A comparison of the crystal data with simulated partial correlation functions derived from the model of Mayerová *et al.* [2] using XTAL [17] is more favourable (Fig. 4-14). Both the Sb–O and the O...O contributions reproduce the observed data with a high degree of accuracy; the slightly broader features in the neutron data are probably a result of small inaccuracies in the oxygen positions predicted for the model. This strongly suggests that the model of Mayerová *et al.* is a more accurate representation of the structure of onoratoite than that of the Menchetti *et al.* model.

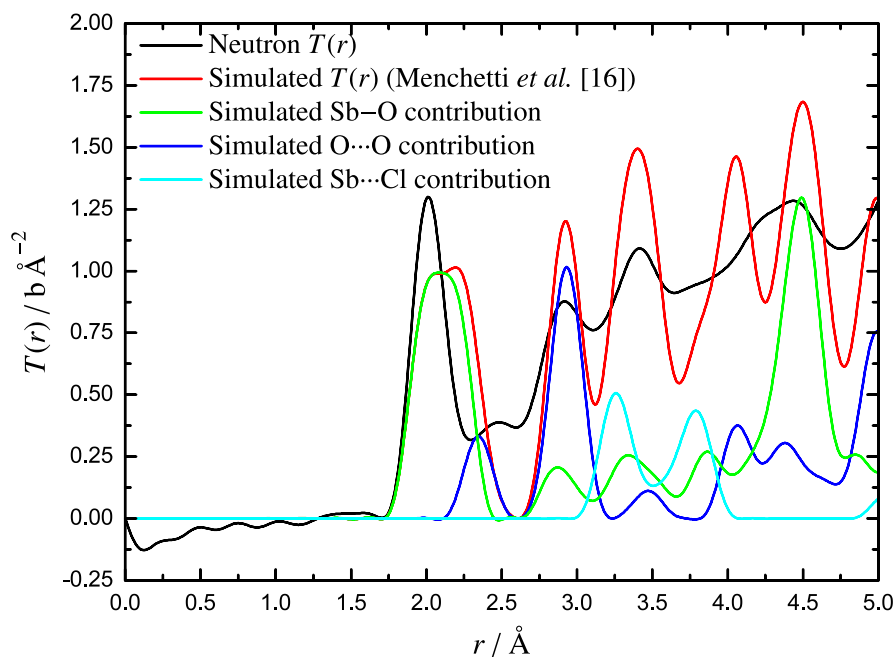


Figure 4-12 The neutron $T(r)$ of the onoratoite crystal compared with simulated correlation functions from the model of Menchetti *et al.* [16] using a Q_{\max} of 27.4 \AA^{-1} (the same as the neutron data). Sb...Sb, Cl...O and Cl...Cl correlations do not begin until $\geq 3.0 \text{ \AA}$ and so are not shown.

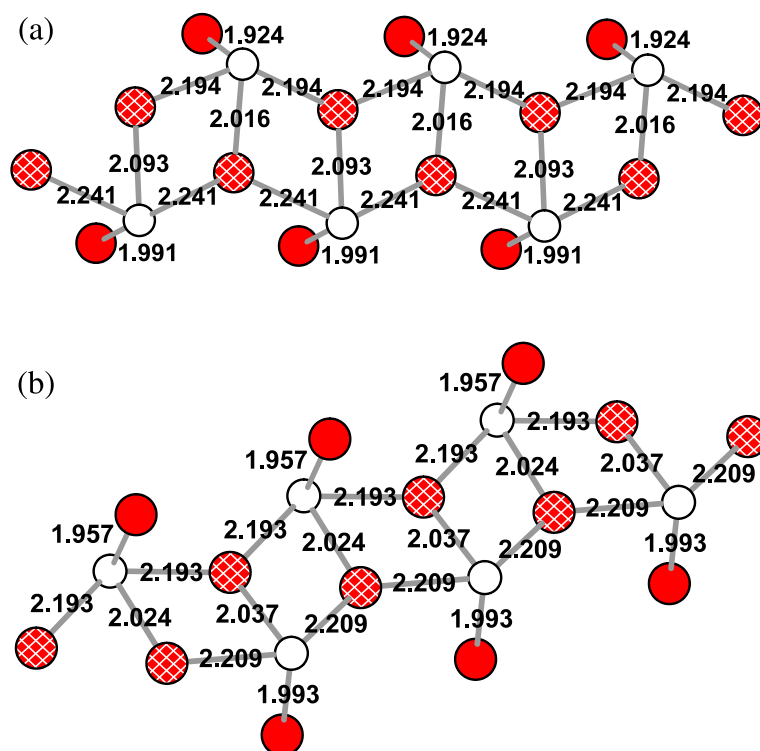


Figure 4-13 The two basic ‘ladder’ units of the Menchetti model [16]. Oxygen atoms are red, antimony atoms are white. Partially occupied oxygen sites are indicated by white cross-hatching. Sb–O bond lengths are also shown.

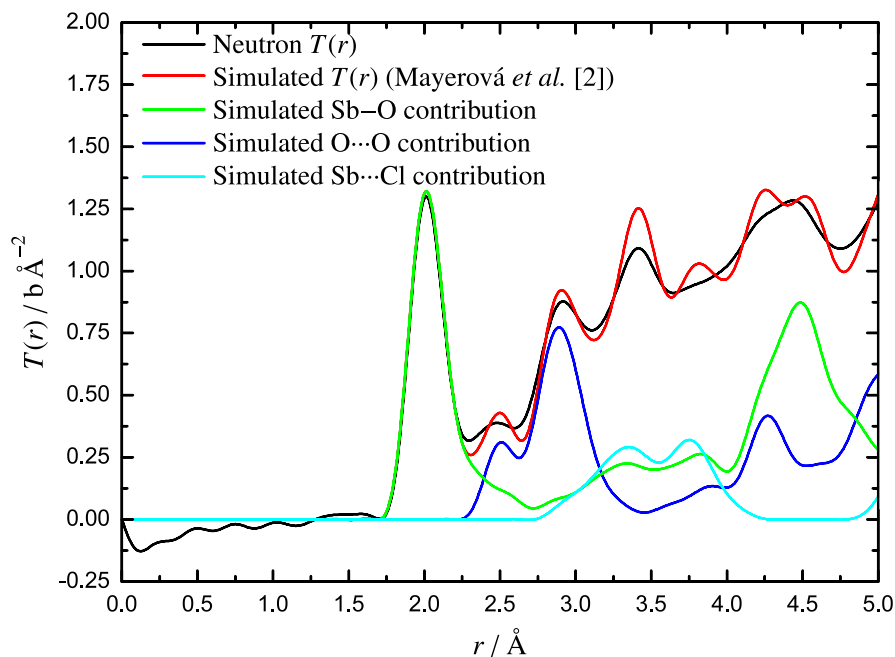


Figure 4-14 The neutron $T(r)$ of the onoratoite crystal compared with simulated correlation functions from the model of Mayerová *et al.* [2] using a Q_{\max} of 27.4 \AA^{-1} (the same as the neutron data). Sb···Sb, Cl···O and Cl···Cl correlations do not begin until $\geq 3.0 \text{ \AA}$ and so are not shown.

Using the onoratoite model of Mayerová *et al.*, a further set of correlation functions were generated (using a Q_{\max} of 40 \AA^{-1}) and compared with the $T(r)$ measured for the $\text{Sb}_8\text{O}_{11}\text{Cl}_2$ glass (Fig. 4-15)—the simulation was used in preference to the recorded onoratoite neutron data because it could be generated to match the full Q -range of the glass data (as opposed to comparing $Q_{\max} = 27.4 \text{ \AA}^{-1}$ with $Q_{\max} = 40 \text{ \AA}^{-1}$). The comparison shows a reasonable agreement and suggests that the short-range order in the glass structure is quite similar to that in the crystalline mineral. The Sb–O peak in the glass is narrower and sharper, indicating a relaxation of the longer bond lengths from the crystal model, which are principally those along the arms of the antimony-oxygen ladders (Fig. 4-16), perhaps suggesting straighter configurations than the zig-zag arrangement present in the crystal. This is also consistent with a shift in the first O···O correlation from $\sim 2.5 \text{ \AA}$ to slightly greater r , since these distances arise from within each ladder (diagonally across each step) and would be separated further by a more linear ladder design.

A reasonable fit to the first Sb–O correlation can be achieved by using two peaks (Fig. 4-17) with positions $r_{\text{SbO}(1)} = 1.980(7) \text{ \AA}$ and $r_{\text{SbO}(2)} = 2.136(41) \text{ \AA}$, and coordina-

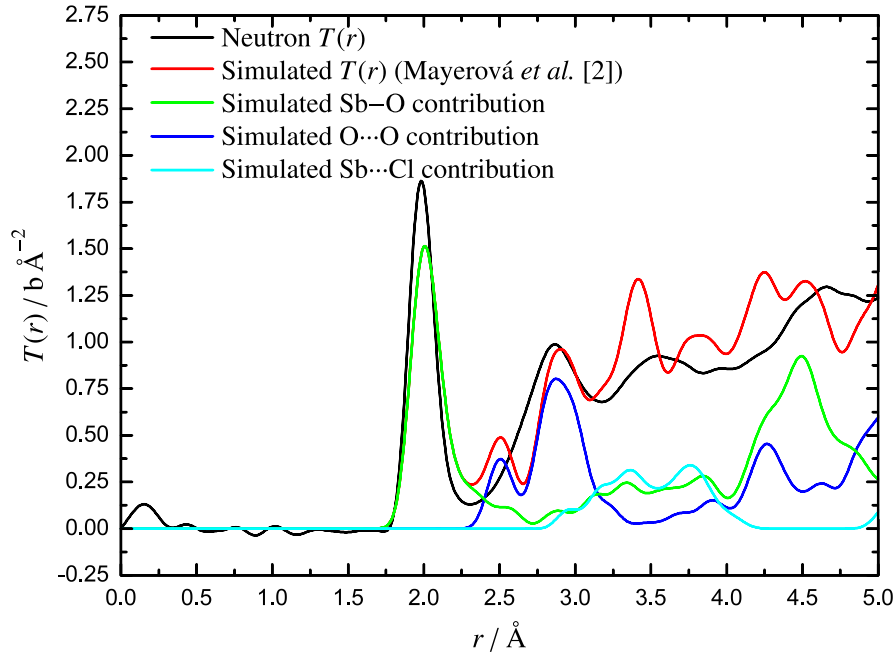


Figure 4-15 The neutron $T(r)$ of the $\text{Sb}_8\text{O}_{11}\text{Cl}_2$ glass compared with simulated correlation functions from the model of Mayerová *et al.* [2] using a Q_{max} of 40 \AA^{-1} (the same as the neutron data). $\text{Sb}\cdots\text{Sb}$, $\text{Cl}\cdots\text{O}$ and $\text{Cl}\cdots\text{Cl}$ correlations do not begin until $\geq 3.0 \text{ \AA}$ and so are not shown.

tion numbers $n_{\text{SbO}(1)} = 2.85(26)$ and $n_{\text{SbO}(2)} = 0.39(30)$. The large errors on the second peak arise from the region of nearly uniform intensity between the $\text{Sb}\text{--}\text{O}$ and $\text{O}\cdots\text{O}$ peaks, resulting in uncertainty in the exact position and extent of the fitted peak. In fact, considering the $\text{Sb}\text{--}\text{O}$ contribution to $T(r)$ in the Mayerová model of onoratoite (Fig. 4-16), it is reasonable to suppose that this region may also contains a third, smaller $\text{Sb}\text{--}\text{O}$ peak that is not defined well enough to be fitted.

The total n_{SbO} of 3.24 (or ~ 3.44 if allowance is made for a third peak approximately half the size of the second) is reasonably consistent with the coordination number of 3.438 predicted by the Mayerová model out to 2.45 \AA : this disregards some of the longer distances in certain $[\text{SbO}_4]$ units (these bonds are highlighted in blue in Figure 4-16), lowering the ratio of four-coordinated to three-coordinated antimony atoms from 11:5 to 7:9. It is unclear if these longer $\text{Sb}\text{--}\text{O}$ distances also occur in the glass (due to the overlapping $\text{O}\cdots\text{O}$ correlation), and so it is also not apparent whether the entire ladder structure is preserved (including the bonds longer than 2.45 \AA) or if instead the connecting chains of $[\text{SbO}_3]$ groups are extended (as Figure 4-16 with the blue bonds removed).

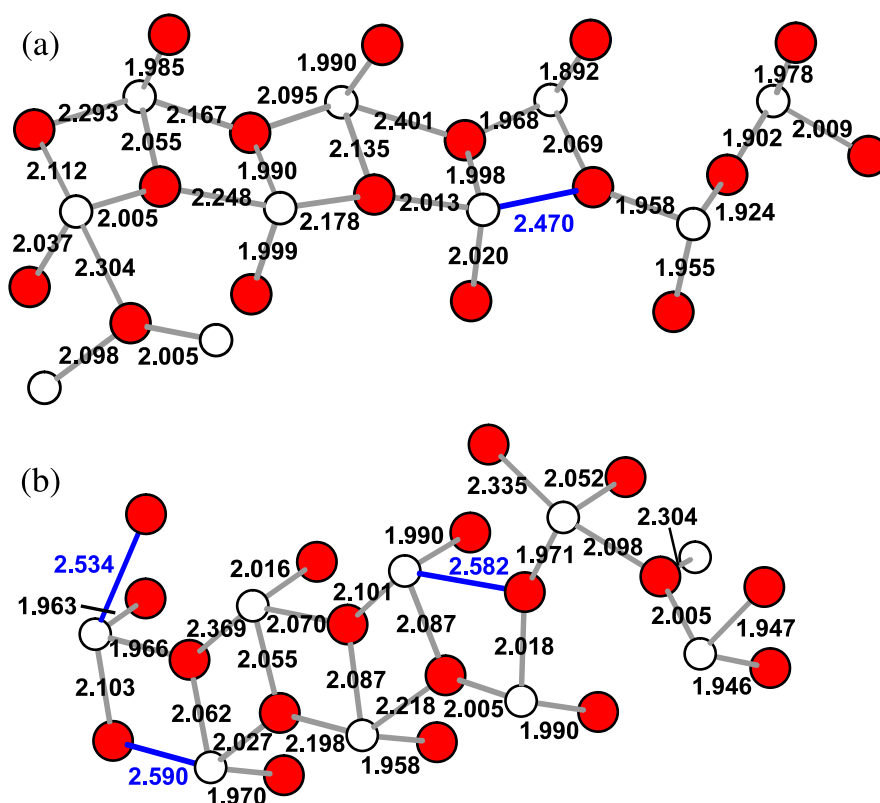


Figure 4-16 The two types of basic 'ladder' unit in the Mayerová model [2]: (a) the ladder is interrupted by two $[\text{SbO}_3]$ groups; (b) the ladder is bridged by one $[\text{SbO}_3]$ and one $[\text{SbO}_4]$ group. Oxygen atoms are red, antimony atoms are white. Sb-O bond lengths are also shown: the four bonds highlighted in blue are those longer than 2.45 Å.

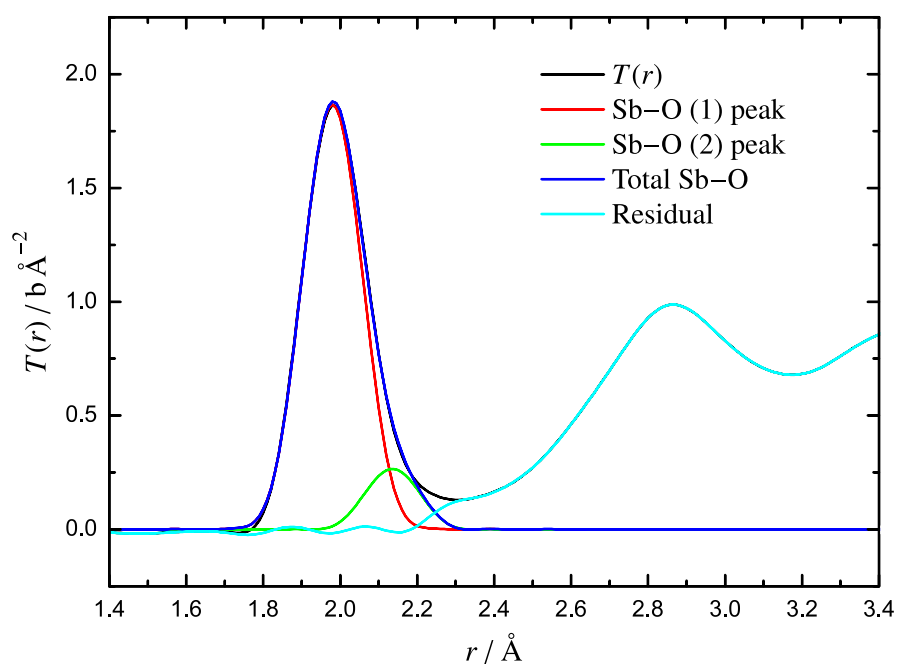


Figure 4-17 A two-peak fit to the first Sb-O correlation in the antimony oxychloride glass.

Note that these comparisons with the structure of crystalline onoratoite do not necessarily indicate that the entire extended structure—of ladders connecting edge-to-edge to form antimony-oxygen tubes, with the tubes forming alternating layers with chlorine atoms—is in any way preserved in the glass. In fact such long-range structural ordering is, by definition, non-existent in a glass structure.

An alternative prediction for the structure of the antimony oxychloride glass might consist of a more disordered network of $[\text{SbO}_3]$ trigonal pyramids and $[\text{Sb}^{3+}\text{O}_4]$ pseudo-trigonal bipyramids, with the chlorine that remains after melting either disrupting the network or filling existing vacancies. The Sb_2O_3 glass discussed earlier may be reasonably similar to this structure, perhaps with $[\text{Sb}^{5+}\text{O}_6]$ octahedra also present, whilst Mössbauer data appears to preclude any Sb^{5+} units in the oxychloride glass (*q.v.* §4.1). Comparing the total correlation functions from the two glasses (Fig. 4-18), it is apparent that the $\text{Sb}_8\text{O}_{11}\text{Cl}_2$ glass structure differs significantly from that of $\nu\text{-Sb}_2\text{O}_3$ between ~ 2.2 Å and ~ 2.5 Å. The additional intensity in this region may arise from an Sb–Cl correlation, since bond-valence calculations predict antimony to be coordinated with three chlorine atoms at 2.35 Å [23, 24], as found in crystalline SbCl_3 [26] and $\text{Sb}_2\text{O}_3\text{--ZnCl}_2$ glasses [14], although only a small proportion of the chlorine ($\sim 10\%$) could be involved based on the size of the discrepancy relative to the Sb–O peak. Alternatively, the ladder-like chains of the Mayerová model give rise to a range of longer Sb–O bond lengths in the same region (Fig. 4-15).

The $T(r)$ comparison of the two glasses also suggests a model for some of the possible structures of $\nu\text{-Sb}_2\text{O}_3$ (*q.v.* §4.4.1): chains of $[\text{SbO}_3]$ trigonal pyramids, interrupted by the occasional $[\text{Sb}^{3+}\text{O}_4]$ unit, similar to the Mayerová ladders but with less four-coordinated antimony, since the relative narrowness of the Sb–O and O···O peaks in the Sb_2O_3 glass appear to confirm that the number of $[\text{Sb}^{3+}\text{O}_4]$ units present is relatively small. The structural role of the $[\text{Sb}^{5+}\text{O}_6]$ octahedra (if present) is less clear, but these could reasonably be expected to appear paired with $[\text{Sb}^{3+}\text{O}_4]$ units, as in Sb_2O_4 , and might then serve as the means of connecting the different $[\text{SbO}_3]/[\text{SbO}_4]$ chains.

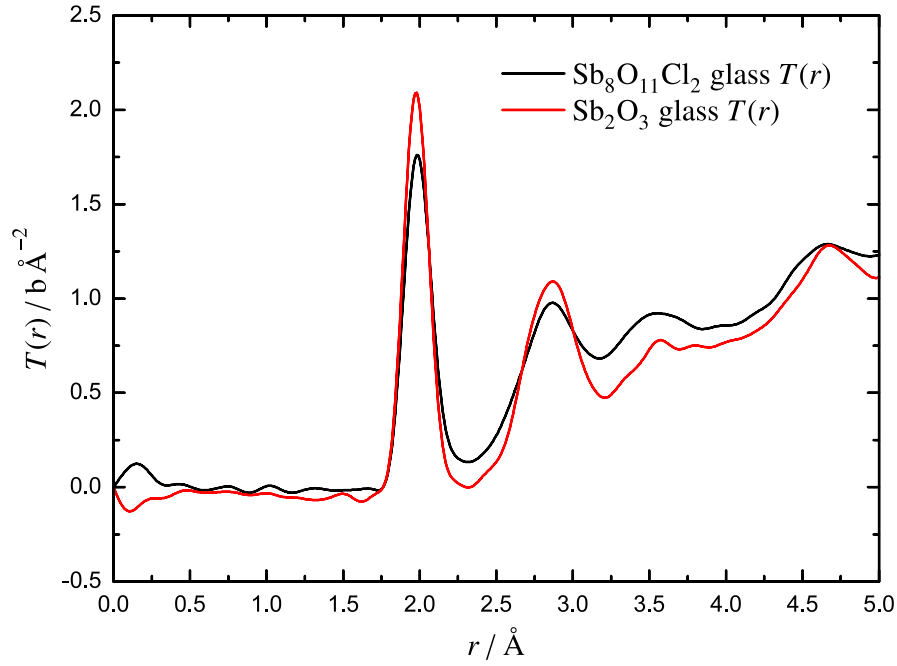


Figure 4-18 The neutron $T(r)$ of the $\text{Sb}_8\text{O}_{11}\text{Cl}_2$ glass compared with that of the Sb_2O_3 glass. Both correlation functions were obtained using a Q_{max} of 35 \AA^{-1} .

4.5 Summary

An antimony oxychloride glass was formed by melting and splat-quenching a quantity of crystalline onoratoite ($\text{Sb}_8\text{O}_{11}\text{Cl}_2$) that was prepared according to the literature [1]; a single-component antimony oxide glass was also made by roller-quenching. X-ray diffraction confirmed that the crystalline onoratoite was single-phase and that the glass samples were fully amorphous. Raman spectroscopy of the oxychloride samples suggested a broadly similar structure between the crystal and the glass, although EDX measurements indicated that the onoratoite contained $\sim 50\%$ more chlorine. Mössbauer spectroscopy indicated that neither the onoratoite crystal nor the oxychloride glass contained any appreciable quantity of Sb^{5+} . Simultaneous TGA/DSC measurements of the three samples were also obtained, the glass transitions and crystallisation temperatures calculated, and the thermal events in the oxychloride systems identified. The densities of the samples were measured by gas pycnometry, with the glasses exhibiting lower values than the associated crystals, as expected.

The neutron $T(r)$ of the Sb_2O_3 glass was compared with simulated correlation functions from the crystalline antimony oxides, with cervantite (Sb_2O_4) providing the clos-

est match. From fitting two peaks to the first Sb–O correlation, coordination numbers were found that suggested the presence of both $[\text{Sb}^{3+}\text{O}_4]$ pseudo-trigonal bipyramids and $[\text{Sb}^{5+}\text{O}_6]$ octahedra in roughly equal quantities, equivalent to ~ 12.4 mol% (amorphous) Sb_2O_4 in a network of $[\text{Sb}^{3+}\text{O}_3]$ trigonal pyramids from the remaining Sb_2O_3 component. Two additional models—one for a system containing little or no Sb^{5+} , based on the addition to the network of $[\text{Sb}^{3+}\text{O}_4]$ units in a 3+1 configuration, the other for a structure where up to 9 % of the antimony is present as Sb^{5+} , using $[\text{Sb}^{5+}\text{O}_6]$ octahedra with a range of bond lengths, similar to those in Sb_2O_5 —are also considered.

Comparisons of the onoratoite crystal $T(r)$ with the models of Menchetti *et al.* [16] and Mayerová *et al.* [2] demonstrated a strong agreement with the latter over the former, with the short- and medium-range order of this structure also relating well to the total correlation function of the antimony oxychloride glass. An alternative structure where $[\text{SbO}_3]$ and $[\text{SbO}_4]$ units are more randomly distributed was also considered, with the Sb_2O_3 glass used for comparison; it is unclear from the available data which structural model is more accurate.

References

- [1] R. Matsuzaki, A. Sofue and Y. Saeki, *Chem. Lett.* **12**, (1973), 1311–1314.
- [2] Z. Mayerová, M. Johnsson and S. Lidin, *Solid State Sci.* **8**, (2006), 849–854.
- [3] R. G. Orman, *Phase Transitions in Antimony Oxides and Related Glasses*, MSc Thesis, University of Warwick (2005).
- [4] P. S. Gopalakrishnan and H. Manohar, *Cryst. Struct. Commun.* **4**, (1975), 203–206.
- [5] J. Amador, E. Gutiérrez Puebla, M. A. Monge, I. Rasines and C. Ruiz Valero, *Inorg. Chem.* **27** (8), (1988), 1367–1370.
- [6] J. F. Bednarik and J. A. Neely, *Phys. Chem. Glasses* **23** (6), (1982), 204–205.
- [7] R. G. Orman and D. Holland, *J. Solid State Chem.* **180** (9), (2007), 2587–2596.
- [8] G. Belluomini, M. Fornaseri and M. Nicoletti, *Mineral. Mag.* **36** (284), (1968), 1037–1044.
- [9] S. A. Jones, J. Fenerty and J. Pearce, *Thermochim. Acta* **114**, (1987), 61–66.
- [10] F. J. Berry and X. Ren, *J. Mater. Sci.* **39**, (2004), 1179–1183.
- [11] H. Hasegawa, M. Sone and M. Imaoka, *Phys. Chem. Glasses* **19** (2), (1978), 28–33.
- [12] Y. P. Kutsenko, I. D. Turyanitsa and D. V. Chepur, *Fiz. Khim. Stekla* **5**, (1979), 395–398.
- [13] J. F. Bednarik and J. A. Neely, *Glastechn. Ber.* **55**, (1980), 126–129.
- [14] J. A. Johnson, D. Holland, J. Bland, C. E. Johnson and M. F. Thomas, *J. Phys. Condens. Mat.* **15**, (2003), 755–764.
- [15] E. Kordes, *Z. Phys. Chem.* **B43**, (1939), 173–190.
- [16] S. Menchetti, C. Sabelli and R. Trosti-Ferroni, *Acta Crystallogr. C* **40**, (1984), 1506–1510.
- [17] A. C. Hannon, *XTAL: A program for calculating interatomic distances and coordination numbers for model structures*, Tech. Rep. RAL-93-063, Rutherford Appleton Laboratory (1993).
- [18] C. Svensson, *Acta Crystallogr. B* **31**, (1975), 2016–2018.

- [19] C. Svensson, *Acta Crystallogr. B* **30**, (1974), 458–461.
- [20] K. Terashima, T. Hashimoto, T. Uchino, S.-H. Kim and T. Yoko, *J. Ceram. Soc. Jpn.* **104** (11), (1996), 1008–1014.
- [21] V. M. Jansen, *Acta Crystallogr. B* **35** (3), (1979), 539–542.
- [22] M. Imaoka, H. Hasegawa and S. Shindo, *J. Ceram. Soc. Jpn.* **77** (8), (1969), 263–271.
- [23] N. E. Brese and M. O’Keeffe, *Acta Crystallogr. B* **47**, (1991), 192–197.
- [24] A. C. Hannon and J. M. Parker, *J. Non-Cryst. Solids* **274**, (2000), 102–109.
- [25] J. C. McLaughlin, S. L. Tagg, J. W. Zwanziger, D. R. Haeffner and S. D. Shastri, *J. Non-Cryst. Solids* **274**, (2000), 1–8.
- [26] A. Lipka, *Acta Crystallogr. B* **35**, (1979), 3020–3022.

Chapter 5

Antimony Borate Glasses

5.1 Sample preparation and characterisation

The ^{11}B -enriched antimony borate glasses used in this work were originally created by Holland *et al.* [1] for an NMR and Mössbauer study. For ease of reference, the preparation details previously published are given below:

“Glasses were prepared of nominal composition $x\text{Sb}_2\text{O}_3 \cdot (1 - x)\text{B}_2\text{O}_3$ with $x = 0.0, 0.1, 0.2, 0.3, 0.4, 0.5, 0.6, 0.7$ and 0.8 . The starting materials were AnalaR grade Sb_2O_3 and B_2O_3 (natural isotopic content). An additional series of samples was prepared with ^{11}B enriched B_2O_3 (99.62 at.% enrichment, Eagle-Picher) to reduce absorption in subsequent neutron diffraction experiments. The amounts of oxides used were calculated to give 25 g of glass for the samples with natural isotopic content, and 10 cm^3 of glass for the ^{11}B -enriched samples. The glasses were melted in air, in 90Pt/10Rh [correction [2], orig.: “10Pt/90Rh”] crucibles, at 950°C or 1150°C for $x > 0.6$. The melts were cast onto a copper plate at room temperature to give pieces approximately 2–3 mm thick. For $x \geq 0.4$, the samples had to be splat quenched between copper plates to prevent phase separation. The glasses were transferred to a desiccator whilst still hot ($\sim 150\text{--}200^\circ\text{C}$) and subsequently stored under vacuum to prevent reaction with atmospheric moisture.”

Holland *et al.* confirmed the amorphousness of these samples by X-ray and neutron diffraction, derived the percentage of antimony atoms present as Sb^{5+} from Mössbauer data (Fig. 5-1) and used quantitative ^{11}B NMR to determine the final glass compositions. Barney [3] checked the isotopic composition of the ^{11}B -enriched B_2O_3 used in these glasses by measuring two lithium borate crystals made from the same chemicals

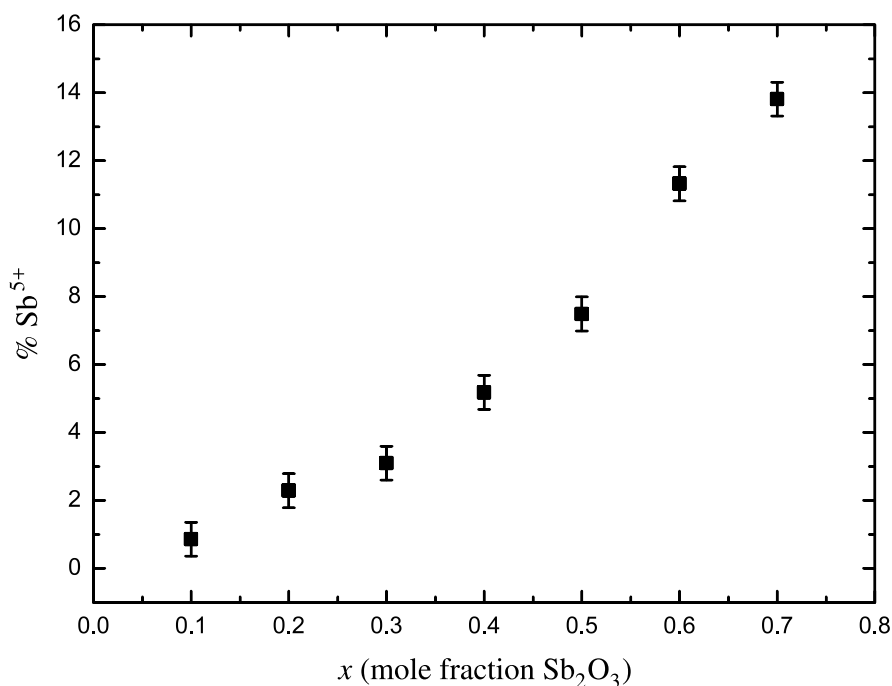


Figure 5-1 The percentage of antimony present as Sb^{5+} in the borate glasses, derived from Mössbauer data by Holland *et al.* [1].

using secondary ion mass spectroscopy: the measured composition was not significantly different from that quoted above.

In this study, EDX data were obtained to confirm that no contaminants were present in the glass within the limit of detection of the technique (~ 2 at.%). DTA measurements of a subset of the samples were also taken to confirm the T_g values previously obtained by Holland *et al.* [1]: the values obtained were the same within experimental error.

5.2 Raman spectroscopy

Unpolarised Raman spectra obtained for the antimony borate samples are shown in Figure 5-2. From studies of borate glasses in the literature—and allowing for the shift to higher wavelength expected due to the more covalent bonding character of antimony—the low-shift bands ($\sim 190\text{ cm}^{-1}$ to $\sim 690\text{ cm}^{-1}$) can be assigned to the stretching, bending and group modes of $[\text{SbO}_3]$ units [4], whilst the peak at $\sim 800\text{ cm}^{-1}$, which is most prominent at low x , is due to the breathing mode of boroxol rings [5]. Some authors have assigned the small feature at $\sim 760\text{ cm}^{-1}$ (which develops with increasing x) to the tetraborate group [4, 6] although Meera and Ramakrishna [7] noted in their

review of Raman studies of borate glasses that it also appears to arise from pentaborate and triborate groupings. The $\sim 981\text{ cm}^{-1}$ band has also not been clearly identified as arising from any single borate structural group [7]. Meera and Ramakrishna [7] associate the peak at $\sim 878\text{ cm}^{-1}$ with orthoborate units ($[\text{BO}_3]$ units with three non-bridging oxygen atoms): this seems somewhat improbable however, given the low x values at which the peak is most prominent—a 1:1 ratio of orthoborate units to Sb^{3+} ions would seem more likely for charge-balancing—in other words, the peak would be expected to be largest at $x = 0.5$. The low-intensity bands from $\sim 1200\text{ cm}^{-1}$ to $\sim 1500\text{ cm}^{-1}$ have been attributed to delocalised B–O stretching from both ring and network contributions [7], and found to be characteristic of a boron network containing non-bridging oxygen atoms [8]. This latter seems unlikely at these compositions, and is more typical of borate glasses with high modifier content, which suggests that this band arises from a different source, such as B–O–Sb linkages.

In line with the reports of other authors [4, 6, 7] the peak arising from the breathing mode of boroxol rings (at $\sim 800\text{ cm}^{-1}$) decreases rapidly with increasing x until it is almost indistinguishable from the baseline at $x \geq 0.6$. This agrees with the model suggested by Terashima *et al.* [4]: that of a network initially consisting primarily of boroxol rings—as in vitreous B_2O_3 , where $\sim 75\%$ of the boron atoms are in such groups [7, 9, 10]—being cleaved by the introduction of Sb^{3+} ions with increasing x .

5.3 Density measurements

Figure 5-3 shows the densities measured for the antimony borate glasses (Table 5-1) plotted against the nominal compositions, together with values reported in the literature [4, 11–15]. There is good agreement with the preponderance of published data, with the exception of some of the values given by Terashima *et al.* [4], which are slightly higher than those of the other authors (as noted previously in §2.4).

However, when the measured densities are plotted against the compositions determined by the quantitative NMR of Holland *et al.* [1] (Fig. 5-4) the (nominal) $x = 0.4$ and $x = 0.6$ samples deviate from the curve apparent from the literature values. This engenders some doubt as to the actual composition of the samples: an important factor when analysing neutron diffraction data.

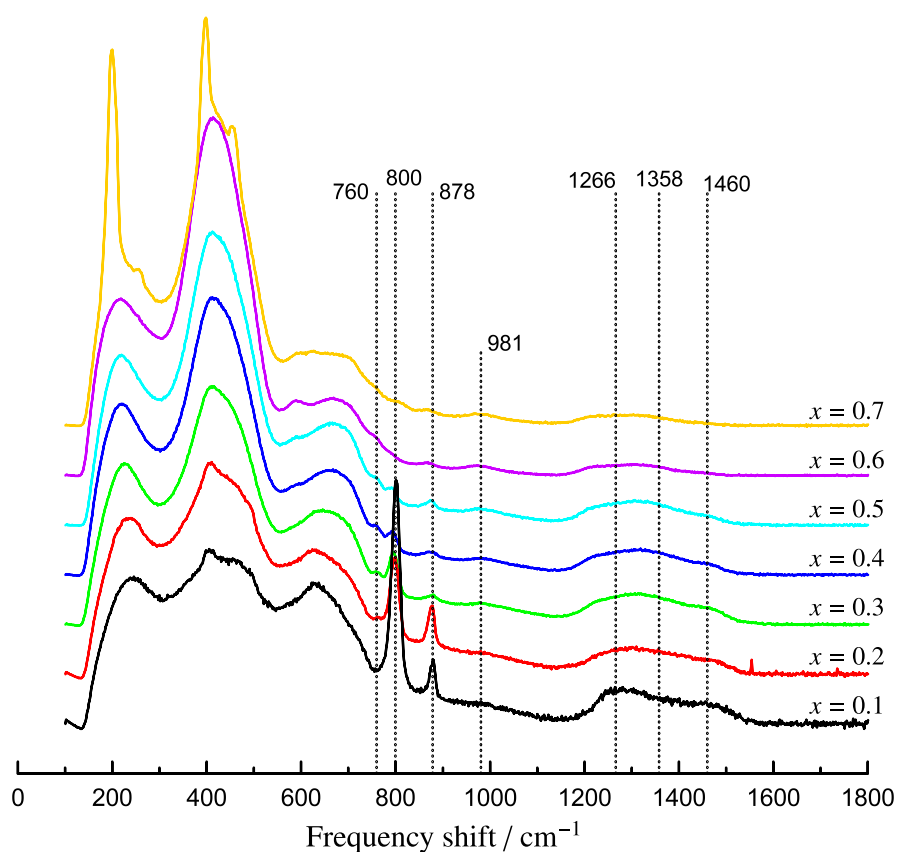


Figure 5-2 Unpolarised Raman spectra for the antimony borate glasses. The laser source had a wavelength of 514 nm and spectra were obtained over the full range available (100 cm^{-1} to 3200 cm^{-1}) before being baseline subtracted. The spectra were normalised with respect to the total integrated intensity over the whole range. No features are present in the spectra beyond 1800 cm^{-1} .

Table 5-1 The measured densities of the antimony borate glasses.

Nominal x (mole fraction Sb_2O_3)	x (Quantitative NMR [1]) (± 0.02)	Density (g cm^{-3}) (± 0.005)
0.1	0.10	2.364
0.2	0.19	2.879
0.3	0.30	3.379
0.4	0.44	3.721
0.5	0.52	4.121
0.6	0.64	4.342
0.7	0.69	4.644

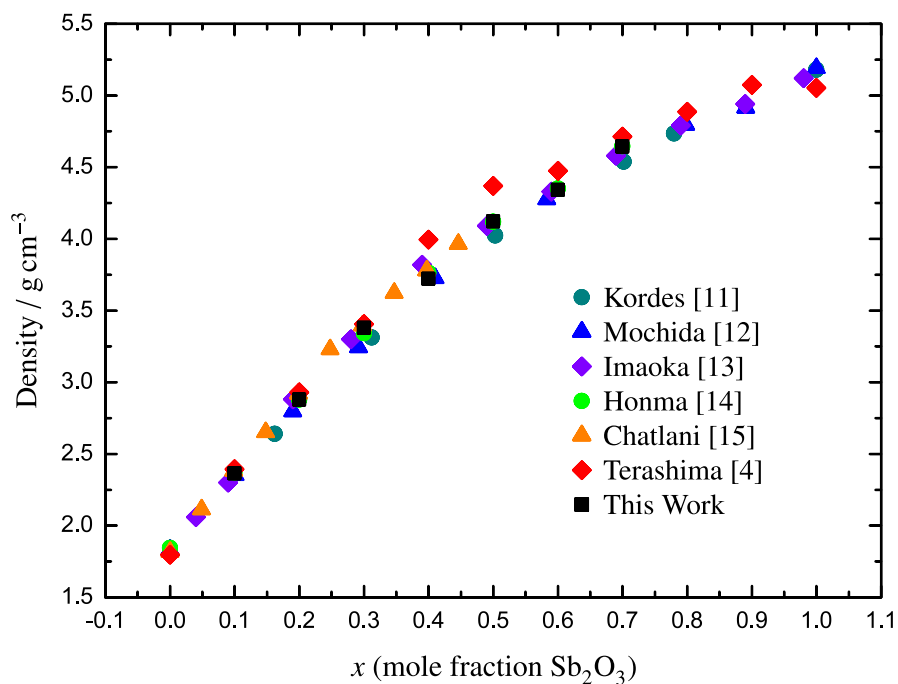


Figure 5-3 A comparison of the measured densities for the antimony borate glasses with values reported in the literature [4, 11–15], using the nominal glass compositions. Error bars are smaller than the symbols plotted.

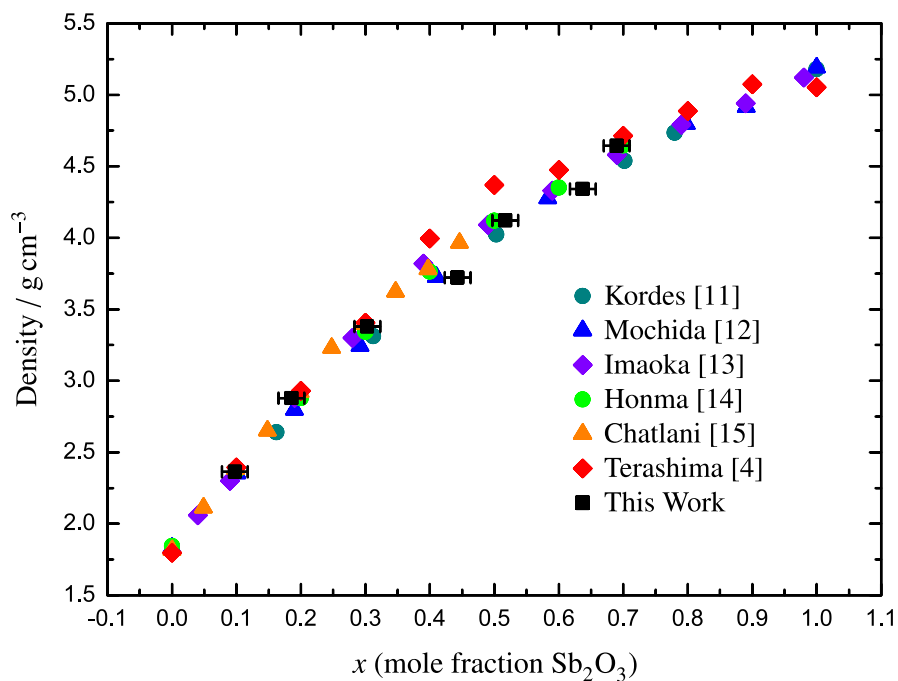


Figure 5-4 A comparison of the measured densities for the antimony borate glasses with values reported in the literature [4, 11–15], using the glass compositions determined from NMR by Holland *et al.* [1]. Density error bars are smaller than the symbols plotted.

Holland *et al.* [1] also reported for each sample the percentage of Sb present as Sb^{5+} , derived from Mössbauer data (Fig. 5-1). The presence of Sb^{5+} means that the formula $x\text{Sb}_2\text{O}_3 \cdot (1-x)\text{B}_2\text{O}_3$ is somewhat inaccurate, which will affect the compositions derived from the NMR data (since the calculated mass of antimony oxide would include more oxygen than otherwise). However, this only reduces x by 0.001 to 0.003, making a negligible difference to the neutron diffraction analysis.

5.4 Neutron diffraction

5.4.1 Total correlation functions

Neutron diffraction data on the antimony borate samples were obtained by Holland *et al.* [1] on the GEM diffractometer [16] at the ISIS pulsed neutron source. Vanadium cans of diameter 8.3 mm and wall thickness 25 μm were used to hold the samples [17]. The signal-to-noise ratio of the data was sufficient to allow a Q_{max} of 40 \AA^{-1} for the Fourier transform, and the total correlation functions are shown in Figures 5-5 and 5-6.

The low- r peaks in $T(r)$ are well-defined and can be attributed to individual atom-atom correlations in this region, using bond-valence calculations [19, 20] and by examining trends in peak intensities with composition. The first peak at $\sim 1.4 \text{ \AA}$ covers the first three- and four-coordinated B–O bond lengths at 1.371 \AA and 1.477 \AA , as calculated from bond-valence parameters, and decreases as the mole fraction of Sb_2O_3 increases. The small distortion at the base of the peak on the high- r side ($\sim 1.60 \text{ \AA}$) has been attributed by Johnson *et al.* [9] to the difficulty in calibrating the instrumental Q scale at high- Q , and has also been observed more recently by Hannon *et al.* [10] in data from the D4 diffractometer [21] at the Institut Laue-Langevin, Grenoble, and from the LAD diffractometer [22] at the ISIS pulsed neutron source. Although GEM might be expected to be better calibrated, it is conceivable that the same problem still persists and so, since this feature appears to be independent of composition, it is not considered further in this work.

The second peak, at $\sim 1.98 \text{ \AA}$, grows with increasing x and arises from the first Sb–O correlation; the shortest Sb–O distance in crystalline Sb_2O_3 (in both senarmontite [23] and valentinite [24] phases) is 1.977 \AA . The asymmetry in this peak at higher x is consistent with the other two Sb–O distances found in valentinite (2.019 \AA and 2.023 \AA),

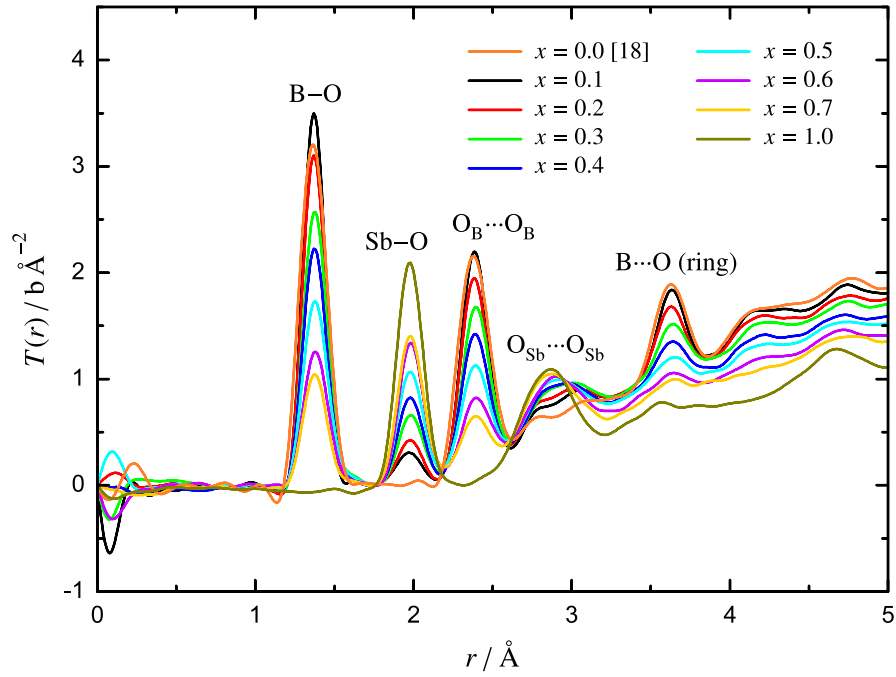


Figure 5-5 The total correlation functions $T(r)$ produced from the neutron diffraction data of the antimony borates [1] using the nominal x values with $Q_{\max} = 40 \text{ \AA}^{-1}$. Also shown are $T(r)$ from $\nu\text{-B}_2\text{O}_3$ [18] and $\nu\text{-Sb}_2\text{O}_3$ (q.v. §4.4.1)—note that these two datasets were processed with lower values of Q_{\max} (30 \AA^{-1} and 35 \AA^{-1} , respectively): this will result in wider peaks with reduced intensity compared to the antimony borates. Labels are the primary correlations giving rise to the peaks, secondary contributions are described in the main text.

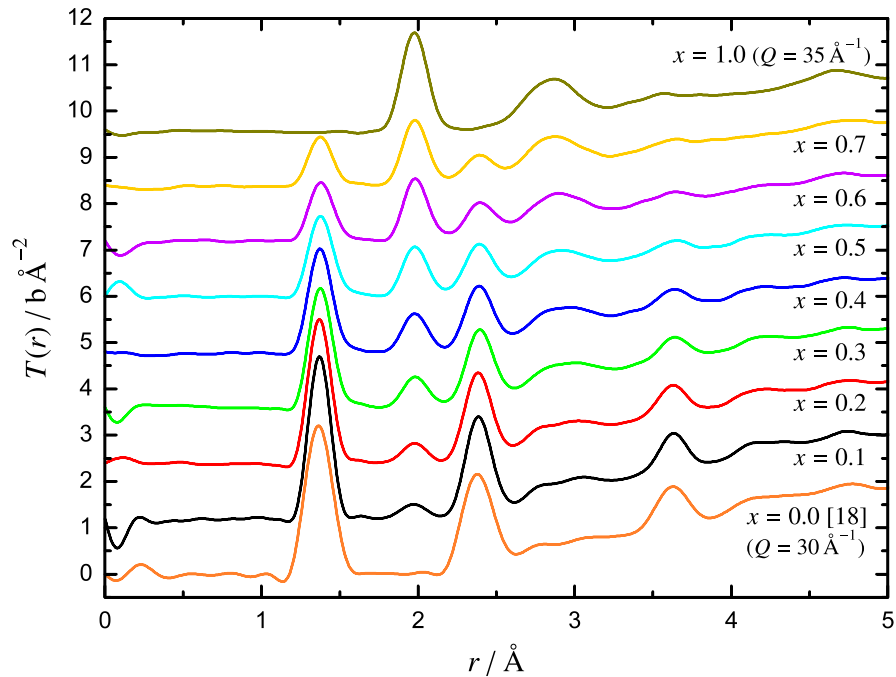


Figure 5-6 The $T(r)$ data from Figure 5-5 with each dataset offset by 1.2 b \AA^{-2} on the y-scale.

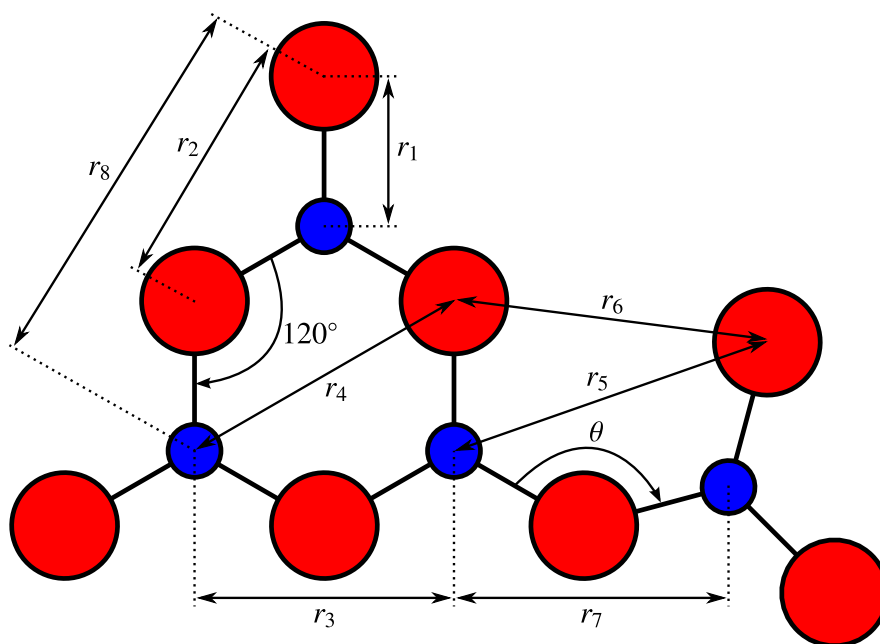


Figure 5-7 The interatomic distances within a $[\text{B}_3\text{O}_6]$ boroxol ring; also shown is an attached $[\text{BO}_3]$ unit (which might itself belong to a boroxol group) at an angle θ . Blue atoms are boron, red are oxygen.

as well as the slightly longer bond lengths in the $[\text{Sb}^{3+}\text{O}_4]$ pseudo-trigonal bipyramids found in Sb_2O_4 or the $[\text{Sb}^{5+}\text{O}_6]$ octahedra in Sb_2O_5 .

The third peak at $\sim 2.4 \text{ \AA}$ arises from $\text{O}_\text{B}\cdots\text{O}_\text{B}$ as well as $\text{B}\cdots\text{B}$ distances within and between boroxol rings [9, 25] (these are labelled r_2 , r_3 and r_7 respectively in Figure 5-7) and decreases as the amount of B_2O_3 present is reduced. The broader fourth peak at $\sim 2.8 \text{ \AA}$ primarily originates from the $\text{O}_\text{Sb}\cdots\text{O}_\text{Sb}$ distance in Sb_2O_3 , but is ill-defined because it also starts to overlap secondary correlations, such as the $\text{B}\cdots\text{O}$ distances across and between boroxol rings (r_4 and r_5 , respectively) and the nearest inter-ring $\text{O}\cdots\text{O}$ correlation (r_6). Finally, the last well-defined peak at $\sim 3.6 \text{ \AA}$ has been attributed to a $\text{B}\cdots\text{O}$ distance characteristic of boroxol rings (r_8), and decreases as the proportion of Sb_2O_3 increases.

From the positions of the $\text{B}-\text{O}$ and $\text{O}_\text{B}\cdots\text{O}_\text{B}$ peaks, the $\text{O}-\text{B}-\text{O}$ angle can be calculated. In $\nu\text{-B}_2\text{O}_3$, $r_{\text{OO}} = 2.380 \text{ \AA}$ which results in a bond angle (for three-coordinated boron) of 120.4° , implying a predominantly planar trigonal environment. The $\text{O}_\text{B}\cdots\text{O}_\text{B}$ distance in the antimony borates appears to shift gradually to higher r with increasing x , but this may be due more to a growing contribution from the $\text{O}_\text{Sb}\cdots\text{O}_\text{Sb}$ correlation than from an actual change in the borate units. The peak arising from $\text{O}_\text{Sb}\cdots\text{O}_\text{Sb}$ is

quite broad, and appears to change smoothly from the $x = 0.0$ to $x = 1.0$ peak-shapes with composition. Whilst this is not useful for determining an accurate value for the O–Sb–O angle due to the number of overlapping correlation functions, it is reasonable to say that it is close to the average value of 93.1° observed in ν -Sb₂O₃ (q.v. §4.4.1).

It is curious to note the prominence of the ‘B···O (ring)’ peak at ~ 3.6 Å, which persists throughout the compositional range studied. This peak (arising from the distance r_8 in Figure 5-7) will persist in a [BO₃] network without B₃O₆ groups, but will be significantly broader due to the removal of the constraint on the B–O–B angle ($= 120^\circ$) caused by the rings; however, the width of the measured peak does not appear to vary with composition. Whilst the formation of boroxol rings is to be expected at low x for a network mainly consisting of planar trigonal [BO₃] units (for example, such rings predominate in ν -B₂O₃ [9, 10, 25]), once a homogeneous network of borate and antimony oxide units becomes possible, it might be expected that such extended structures would disappear. In the NMR study of Holland *et al.* [1], it was noted that the two [BO₃] sites resolvable at low x (for units within and outside the boroxol group) became increasingly similar as more Sb₂O₃ was added to the system, until $x \geq 0.5$ where it was almost as effective to fit a single [BO₃] contribution to the data. This is consistent with the persistence of the boroxol breathing mode peak in the Raman data up to $x = 0.5$ (q.v. §5.2). For a straight mixture of trigonal planar [BO₃] units and [SbO₃] trigonal pyramids, $x > 0.5$ is also the point where it is no longer possible to terminate all Sb–O pairs with a [BO₃] unit. The persistence of the 3.6 Å peak in the neutron data could therefore indicate that there is a degree of heterogeneity that limits the intermingling of the B₂O₃ and Sb₂O₃ glass networks, with small clusters of boroxol rings persisting in boron-rich regions.

By scaling the total correlation function of each sample by the calculated B–O partial correlation coefficient (Fig. 5-8), it becomes apparent that there is an asymmetrical broadening of the first B–O peak, the extent of which approximately correlates with increasing x (this can also be seen by the reduction in peak height as part of the peak area is moved to higher r). This is consistent with the trend in N_4 ratios reported by Holland *et al.* [1] and the longer bond lengths to be expected of such units. A similar scaling of $T(r)$ by the Sb–O partial correlation coefficients (Fig. 5-9) shows a greater consistency in the Sb environment between the samples, with the exception of the $x = 0.1$

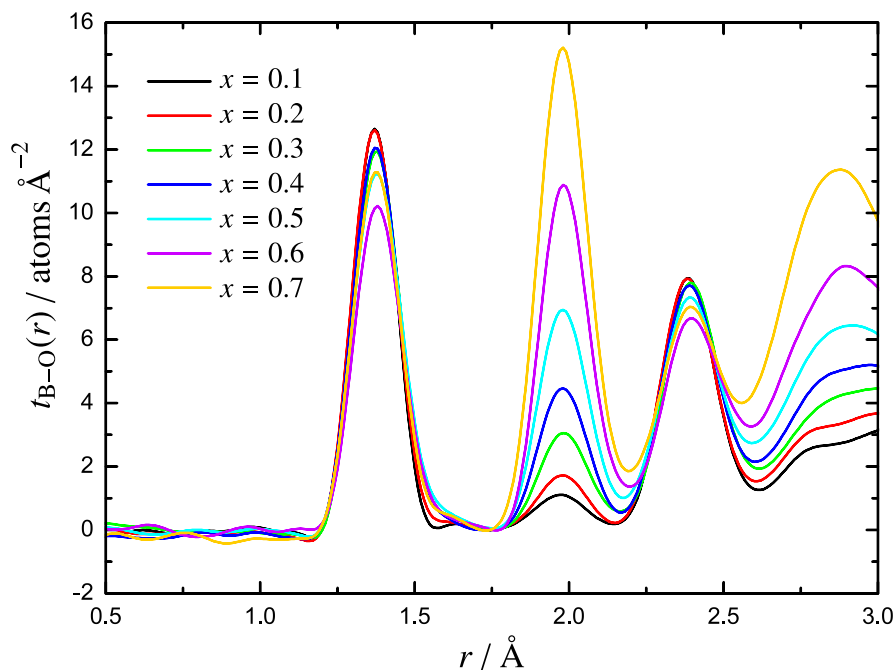


Figure 5-8 The weighted total correlation function for the antimony borates, obtained by dividing $T(r)$ by the B–O partial correlation coefficient. x values used are from the nominal batch compositions.

glass. This discrepancy is most readily explained by an underestimation of the actual Sb_2O_3 content: since the Sb–O coefficient is already so small, even a slight change in composition will have a large effect on the scaling of the correlation function.

5.4.2 Peak-fitting

Table 5-2 shows the details of a one-peak fit to the first B–O correlation in $T(r)$. Although the low- x coordination numbers are reasonable, at higher x (in particular at $x = 0.6$) the value is much lower than expected. Examining the residual of the fit (Fig. 5-10a) shows that the oscillations remaining are greater than those present in the short- r region preceding the first peak, indicating that a single-peak fit is inadequate. This is consistent with the presence of $[\text{BO}_4]$ units indicated by NMR [1].

By fitting two peaks to the first B–O correlation, better fits are produced, at least in terms of the residual, as demonstrated in Figure 5-10b. However, attempting to fit two peaks to the $x = 0.1$ and $x = 0.2$ samples resulted in unreasonable fits, suggesting that the second peak, if present, is too small to be accurately modelled. Where two-peak fits were possible, average bond lengths were constrained at 1.371 Å and 1.477 Å, as calculated from bond-valence parameters [19, 20] for three- and four-coordinated

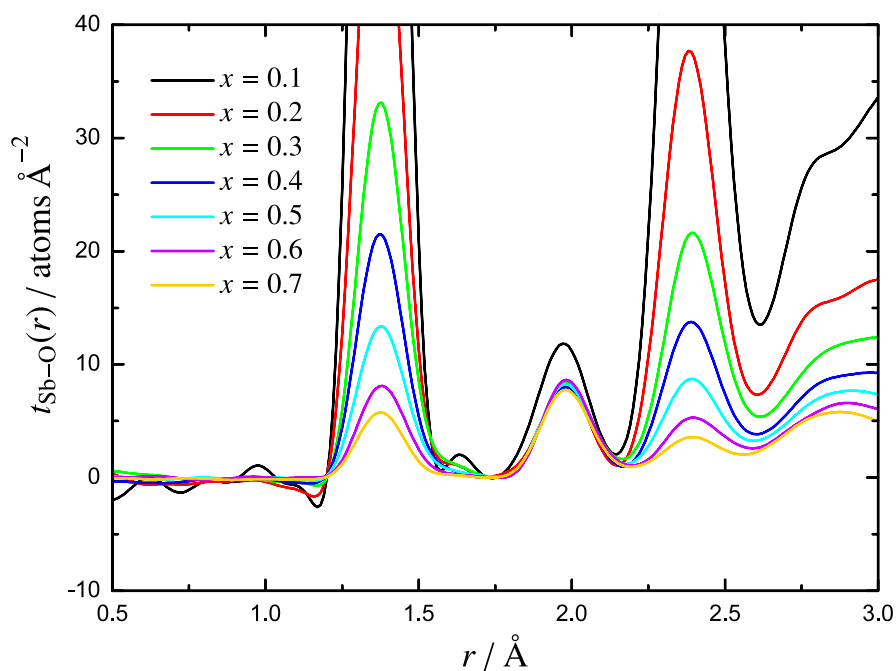


Figure 5-9 The weighted total correlation function for the antimony borates, obtained by dividing $T(r)$ by the Sb–O partial correlation coefficient. x values used are from the nominal batch compositions.

Table 5-2 B–O coordination numbers obtained from a one-peak fit of the first $T(r)$ peak of the antimony borate samples; average bond lengths and RMS deviations are also given. Errors quoted are the statistical errors from fitting the peaks.

x (nominal)	r_{BO}	$\langle u_{\text{BO}}^2 \rangle^{1/2}$	n_{BO}
0.1	1.371(1)	0.045(2)	2.92(5)
0.2	1.371(1)	0.049(1)	3.02(2)
0.3	1.378(1)	0.052(1)	2.96(3)
0.4	1.376(1)	0.053(1)	3.02(2)
0.5	1.380(1)	0.057(2)	2.92(5)
0.6	1.382(2)	0.057(3)	2.65(6)
0.7	1.377(1)	0.053(2)	2.83(4)

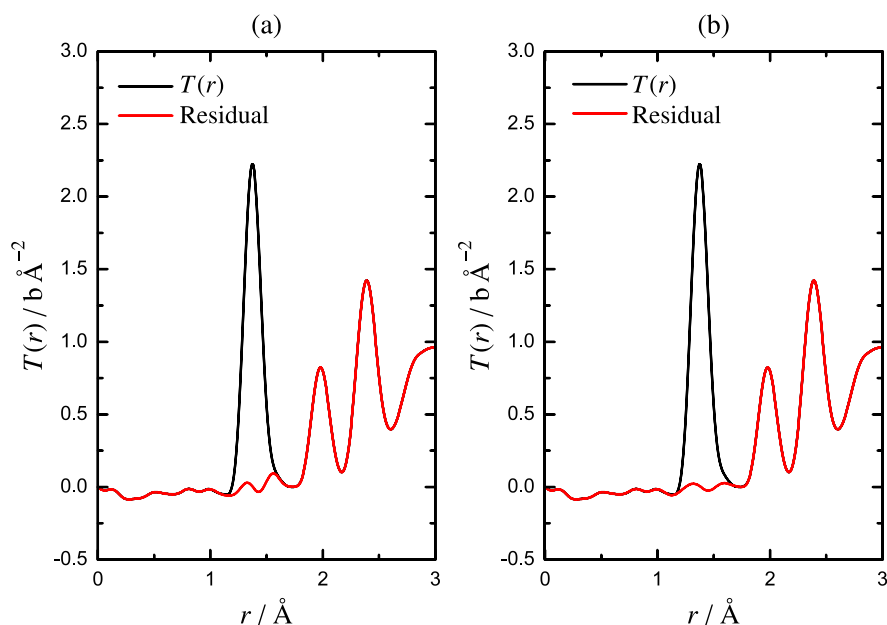


Figure 5-10 The residuals of (a) single- and (b) double-peak fits to the first B–O correlation for the $x = 0.4$ (nominal composition) antimony borate sample.

boron, respectively—it is worth noting that the earlier single-peak fit (with the bond length unconstrained) obtained the three-coordinated boron distance for $x = 0.1$ and $x = 0.2$. The coordination numbers calculated from the fits are given in Table 5-3. Note that the errors displayed for the total n_{BO} are from single-peak fits; due to the small distortion on the greater- r side of the peak mentioned earlier, the error on the second B–O peak—and consequently, also the error on the first peak—are exaggerated. Therefore, the error from the single-peak fit is deemed to be a more realistic measure of uncertainty for the overall coordination number.

Although fitting B–O with two peaks has improved the residual, the total coordination numbers obtained have not significantly changed, aside from an increased error due to the disparity in size between the two peaks fitted. Notably, the coordination number of the $x = 0.6$ sample is still too low: this may indicate that the composition that has been used for the analysis is incorrect. Underestimating the proportion of Sb_2O_3 in the sample would result in coordination numbers that are too low for B–O and too high for Sb–O, due to the use of inaccurate partial correlation coefficients. Since the quantitative NMR of Holland *et al.* [1] (Table 5-1) indicated a significantly higher x value for this sample, it seems prudent to re-examine the diffraction data using the alternate compositions, despite the discrepancies with the densities noted in §5.3.

Table 5-3 B–O coordination numbers obtained from a two-peak fit of the first $T(r)$ peak of the antimony borate samples. Also shown are calculated coordination numbers from the N_4 values provided by Holland *et al.* [1]. Errors quoted are the statistical errors from fitting the peaks, except for the total n_{BO} , where the errors from a single-peak fit were deemed more realistic (see main text).

x (nominal)	$n_{\text{BO}(1)}$	$n_{\text{BO}(2)}$	Total n_{BO}	n_{BO} (NMR [1])
0.1	2.92(5)	–	2.92(5)	3.01(1)
0.2	3.02(2)	–	3.02(2)	3.05(1)
0.3	2.66(6)	0.33(11)	2.98(3)	3.09(1)
0.4	2.76(5)	0.31(10)	3.07(2)	3.12(1)
0.5	2.52(7)	0.49(8)	3.01(5)	3.13(1)
0.6	2.26(12)	0.42(21)	2.68(6)	3.13(1)
0.7	2.59(5)	0.28(5)	2.88(4)	3.10(1)

Table 5-4 B–O coordination numbers obtained from a two-peak fit of the first $T(r)$ peak of the antimony borate samples, using x values measured by Holland *et al.* [1]. Also shown are coordination numbers calculated from the N_4 values obtained from the same source. Errors quoted are the statistical errors from fitting the peaks, except for the total n_{BO} , where the errors from a single-peak fit were deemed more realistic (see main text).

x (NMR [1])	$n_{\text{BO}(1)}$	$n_{\text{BO}(2)}$	Total n_{BO}	n_{BO} (NMR [1])
0.097	2.89(3)	–	2.89(3)	3.01(1)
0.185	3.09(2)	–	3.09(2)	3.05(1)
0.302	2.66(3)	0.37(3)	3.03(2)	3.09(1)
0.442	2.81(5)	0.29(5)	3.10(4)	3.12(1)
0.516	2.65(6)	0.44(5)	3.09(4)	3.13(1)
0.638	2.47(5)	0.50(4)	2.97(4)	3.13(1)
0.691	2.68(6)	0.30(5)	2.98(5)	3.10(1)

Table 5-4 shows the parameters derived from two-peak fits to the data when analysed using the NMR x values. As previously, peak positions were fixed and only a single peak could be fitted to the samples at $x \leq 0.2$. With this analysis coordination numbers are more consistent between samples, but still too imprecise to compare with those calculated from NMR. This does not necessarily indicate that the compositions are still incorrect: the relatively small variation in N_4 between the samples combined with the low number of $[\text{BO}_4]$ units overall may simply mean that neutron diffraction is less suitable than NMR for accurately determining B–O coordination in these samples. If the compositions are still inaccurate however, this should be evident in the coordination numbers obtained by fitting the first Sb–O peak.

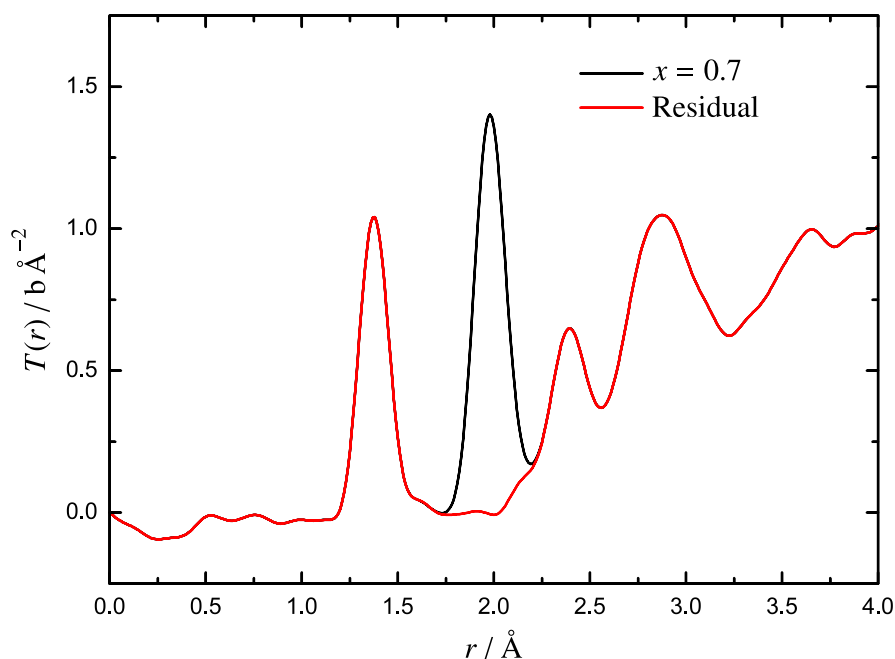


Figure 5-11 The residual of a single-peak fit to the first Sb–O correlation for the $x = 0.7$ (nominal composition) antimony borate sample.

As with B–O, the Sb–O correlation was first fitted with a single unconstrained peak. Whilst these fits gave reasonably consistent coordination numbers (~ 3.10 , using nominal x values) it became apparent from the residual that a second smaller peak at greater r was also present (Fig. 5-11): as a result, two peaks were instead fitted where possible. The two-peak fits were constrained by requirements for positive peak areas and identical RMS deviations, in order to produce sensible peaks (the second constraint is an approximation, since longer bond lengths should result in weaker bonds and higher deviations for the same pair of atoms). Table 5-5 shows the parameters resulting from data analysed with both nominal x values and those derived from NMR. Although two peaks could only be distinguished for $x \geq 0.4$, the noticeable increase in $r_{\text{SbO}(1)}$ for the $x = 0.3$ sample suggests that the second peak is still present at low x .

From these coordination numbers it is evident that some of the x values derived from NMR are less appropriate than the nominal compositions: for example, $x = 0.44$ results in a total coordination number of 2.76(5), whereas a value of 3.00 or greater is expected, based on a network of $[\text{Sb}^{3+}\text{O}_3]$ trigonal pyramids with some more highly-coordinated units arising from the presence of Sb^{5+} . It is also notable that, when using the NMR-derived compositions of $x = 0.44$ and $x = 0.64$ the densities of these two samples do not agree with values published previously in the literature (*q.v.* §5.3). However, in most

Table 5-5 Sb–O coordination numbers obtained from two-peak fits of the second peak present in the $T(r)$ of the antimony borate samples, using both nominal x values and those from NMR [1]. Errors quoted are the statistical errors from fitting the peaks.

x (nominal)	$r_{\text{SbO}(1)}$ (Å)	$n_{\text{SbO}(1)}$	$r_{\text{SbO}(2)}$ (Å)	$n_{\text{SbO}(2)}$	Total n_{SbO}
0.1	1.972(1)	4.73(2)	–	–	4.73(2)
0.2	1.978(1)	3.13(1)	–	–	3.13(1)
0.3	1.982(1)	3.20(1)	–	–	3.20(1)
0.4	1.973(1)	2.73(3)	2.086(5)	0.43(3)	3.15(7)
0.5	1.974(1)	2.86(2)	2.101(3)	0.48(2)	3.34(3)
0.6	1.978(1)	2.99(1)	2.126(3)	0.48(1)	3.46(3)
0.7	1.978(1)	2.89(1)	2.147(3)	0.32(1)	3.21(1)
x (NMR [1])	$r_{\text{SbO}(1)}$ (Å)	$n_{\text{SbO}(1)}$	$r_{\text{SbO}(2)}$ (Å)	$n_{\text{SbO}(2)}$	Total n_{SbO}
0.097	1.973(1)	5.33(2)	–	–	5.33(2)
0.185	1.974(1)	3.54(2)	–	–	3.54(2)
0.302	1.985(1)	3.31(2)	–	–	3.31(2)
0.442	1.973(1)	2.36(3)	2.085(4)	0.39(2)	2.76(5)
0.516	1.971(1)	2.67(2)	2.084(3)	0.53(2)	3.20(5)
0.638	1.978(1)	2.81(2)	2.124(4)	0.45(1)	3.25(3)
0.691	1.978(1)	3.13(1)	2.152(2)	0.33(1)	3.46(1)

cases it is not evident which of the two compositions—nominal or NMR-derived—is more representative of any individual glass sample.

5.4.3 Sample compositions and structural trends

Sb–O coordination numbers can be predicted from the Mössbauer spectroscopy measurements of Holland *et al.* [1] using two models: in the first all Sb^{5+} is treated as occurring as $[\text{Sb}^{5+}\text{O}_6]$ octahedra in a network that otherwise consists exclusively of $[\text{Sb}^{3+}\text{O}_3]$ trigonal pyramids; in the second model, the $[\text{Sb}^{5+}\text{O}_6]$ octahedra are matched by an equivalent number of $[\text{Sb}^{3+}\text{O}_4]$ pseudo-trigonal bipyramids—this latter model is similar to a mixture of crystalline Sb_2O_3 and Sb_2O_4 . The values calculated for both models are shown in Table 5-6; neither model is entirely consistent with the coordination numbers obtained from either the nominal or the NMR-derived compositions. This may indicate that the Mössbauer data is inaccurate, or that neither the nominal nor NMR-derived x values are representative of the actual glass compositions.

Since the NMR data of Holland *et al.* [1] showed clearly separated peaks from the $[\text{BO}_3]$ and $[\text{BO}_4]$ contributions, the resulting coordination numbers should be reason-

Table 5-6 The Sb–O coordination numbers measured from the neutron data (using both nominal and NMR compositions) compared with two models based on the Sb^{5+} values obtained from Mössbauer spectroscopy [1]: one model assumes all Sb^{5+} present occurs in $[\text{Sb}^{5+}\text{O}_6]$ octahedra in a network of $[\text{Sb}^{3+}\text{O}_3]$ trigonal pyramids, the other is similar but posits $[\text{Sb}^{3+}\text{O}_4]$ pseudo-trigonal bipyramids to occur in equal ratio with the Sb^{5+} octahedra (as in crystalline Sb_2O_4).

x (nominal)	n_{SbO} (nominal x)	n_{SbO} (NMR x)	n_{SbO} from Mössbauer Sb^{5+} [1]	
			With $[\text{Sb}^{5+}\text{O}_6]$	With $[\text{Sb}^{5+}\text{O}_6]$ and $[\text{Sb}^{3+}\text{O}_4]$
0.1	4.73(2)	5.33(2)	3.03(3)	3.03(4)
0.2	3.13(1)	3.54(2)	3.07(3)	3.09(4)
0.3	3.20(1)	3.31(2)	3.09(3)	3.12(4)
0.4	3.15(7)	2.76(5)	3.16(3)	3.21(4)
0.5	3.34(3)	3.20(5)	3.22(3)	3.30(4)
0.6	3.46(3)	3.25(3)	3.34(3)	3.45(4)
0.7	3.21(1)	3.46(1)	3.41(3)	3.55(4)

ably accurate and could be used as ‘target’ values for the neutron diffraction analysis. By adjusting x , re-processing the neutron data and re-fitting the B–O peak in $T(r)$, n_{BO} can be made to approximate the NMR value (actually slightly lower due to Fourier transforming over a finite Q -range). Table 5-7 shows an example of the values obtained by this ‘trial-and-improvement’ method for the (nominal) $x = 0.6$ sample: here $x = 0.675$ seems to be the most appropriate match to the NMR n_{BO} of 3.13(1). However, this composition results in a total Sb–O coordination number of 2.87(2) that is too low: $[\text{SbO}_3]$ trigonal pyramids would produce a value closer to 3.00, whilst the 11.3 % of the Sb present as Sb^{5+} , indicated by Mössbauer spectroscopy [1], is likely to increase this number further. The size of the error on n_{BO} also means that compositions several mol% Sb_2O_3 greater or lower could be equally viable choices, whilst attempting to narrow down the x value using n_{SbO} proves futile, since the actual value is unknown (beyond expecting it to be ~ 3.00 or greater). Thus it becomes apparent that, whilst this method of selecting sample compositions seems appealing, in practice it merely provides a considerable range of possible x values that cannot be easily distinguished from one another.

To obtain a reasonable set of data for further analysis, it is necessary to assign the most plausible composition to each sample. By examining a list of criteria based on reasonable predictions (such as the expected B–O and Sb–O coordination numbers

Table 5-7 Values obtained from peaks fitted to $T(r)$ for the nominal $x = 0.6$ sample, over a range of compositions chosen by ‘trial-and-improvement’ to approach the coordination number of 3.13(1) obtained from NMR [1], allowing for the reduction due to limited Q resolution. Errors quoted are the statistical errors from fitting the peaks, except for the total n_{BO} , where the errors from a single-peak fit were deemed more realistic (see main text).

x	$n_{\text{BO}(1)}$	$n_{\text{BO}(2)}$	Total n_{BO}	$n_{\text{SbO}(1)}$	$n_{\text{SbO}(2)}$	Total n_{SbO}
0.60	2.26(12)	0.42(21)	2.68(6)	2.99(1)	0.48(1)	3.46(3)
0.638	2.47(5)	0.50(4)	2.97(4)	2.81(2)	0.45(1)	3.25(3)
0.65	2.40(9)	0.55(10)	2.94(7)	2.66(2)	0.40(1)	3.07(4)
0.67	2.46(9)	0.58(10)	3.04(7)	2.58(1)	0.34(1)	2.92(2)
0.675	2.48(9)	0.59(10)	3.08(7)	2.52(1)	0.35(1)	2.87(2)
0.68	2.51(9)	0.60(11)	3.11(7)	2.49(1)	0.35(1)	2.84(2)

from NMR N_4 values and Mössbauer data), patterns evident in the data (for example, the second Sb–O peak position tends towards higher r with increasing x in both datasets) and comparisons with literature data (such as the density measurements shown earlier), the most likely x values for the samples can be chosen.

Using this set of x values, it is noticeable that the total Sb–O coordination number tends to a fixed value of ~ 3.25 (Fig. 5-12)—this is the same total coordination number found earlier for the Sb_2O_3 glass (*q.v.* §4.4.1). The notable exception is the $x = 0.1$ sample with a coordination number of 4.73(2), but whether this is actually representative of a higher coordination is unclear: it seems unlikely that Sb^{3+} would be able to form a highly coordinated arrangement (such as the octahedra formed by Sb^{5+} in Sb_2O_5 [26]) given the planar nature of the surrounding B_2O_3 matrix and in the absence of longer bond lengths (although these do appear at higher x ; Table 5-5).

It is also interesting to note that the contribution to the total coordination number from the second Sb–O peak does not vary much between samples and, in particular, does not rise uniformly with increasing x . A simple model that attributes the first peak to Sb^{3+} –O and the second to Sb^{5+} –O would suggest scaling the two coordination numbers by the antimony fractions derived from Mössbauer data (Fig. 5-1), but the relative invariance of the contribution from the second peak results in the proposed Sb^{5+} coordination progressing from 8.21 down to 2.32 over the range $x = 0.4$ to $x = 0.7$. Such radical changes with composition seem most unlikely, and thus suggests that either the Mössbauer data is inaccurate, or that the second peak is not exclusively due to Sb^{5+} .

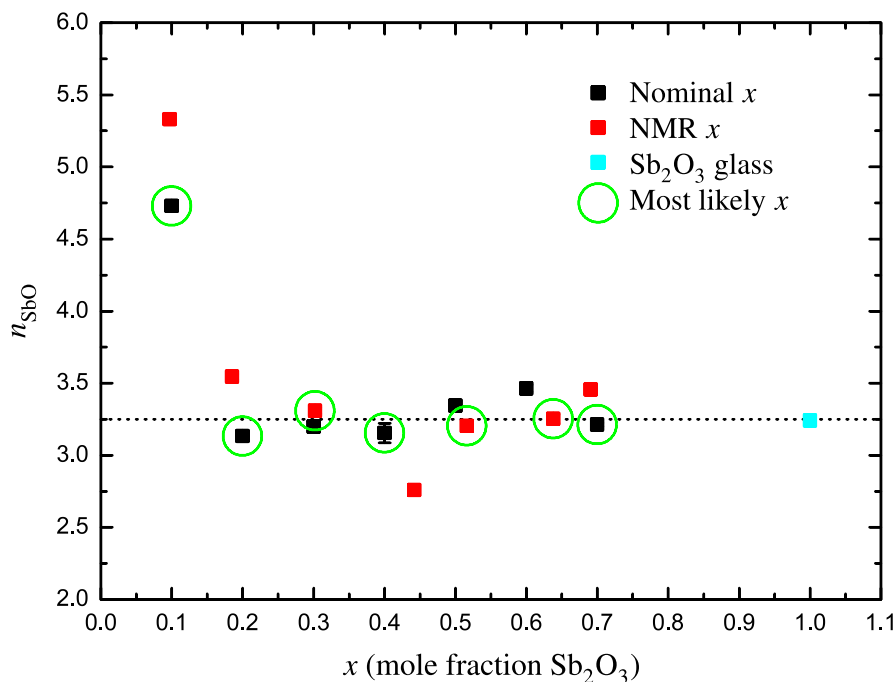


Figure 5-12 The total Sb–O coordination numbers for the antimony borate samples, as well as the value found previously for the Sb₂O₃ glass (*q.v.* §4.4.1). Numbers from both nominal and NMR x values are shown, and the values for the compositions judged most plausible are highlighted. Where not apparent, error bars are smaller than the symbols plotted.

As noted earlier, the position of the second Sb–O peak tends to move to greater r with increasing x , whilst the first peak position remains nearly constant (Fig. 5-13). The positive gradient for $0.1 \leq x \leq 0.3$ would therefore indicate that the second peak is probably also present at those x values, but is too small to be assigned a separate peak when fitting. However, this shift may also be an anomaly rather than an actual trend, since the $x = 1.0$ sample (the Sb₂O₃ glass discussed earlier; *q.v.* §4.4.1) shows that the position of the second peak has returned to the value at $x \approx 0.5$.

The position of the first peak is consistent with the ‘standard’ Sb–O distance of 1.98 Å observed in crystalline Sb₂O₃, and suggests that the antimony atoms are three-coordinated from the distance predicted by bond-valence calculations. When comparing the second Sb–O distance in the glass with the crystalline oxides however, only the longer bond lengths reported for the [Sb⁵⁺O₆] octahedra found in Sb₂O₅ [26] are of similar length. This may indicate that similar octahedra form in the borate glasses, although the shorter bond lengths observed in the Sb₂O₅-type octahedra (at 1.89 Å and 1.91 Å) are likely to be masked by the main [Sb³⁺O₃] peak at 1.98 Å and the amorphous

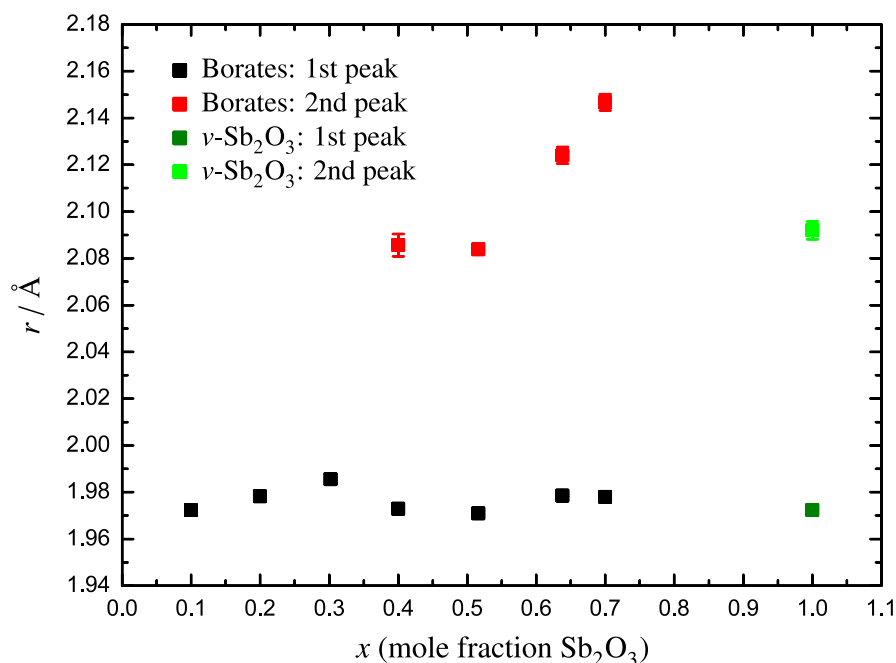


Figure 5-13 The positions of the Sb–O peaks for the antimony borate samples, as well as the values for the Sb₂O₃ glass (*q.v.* §4.4.1). The x values used are those judged to be most plausible. Where not apparent, error bars are smaller than the symbols plotted.

nature of the glass might be expected to allow the octahedra to relax to a more uniform bond length, such as the 2.01 Å predicted by bond-valence parameters, which is then too low to explain the second Sb–O peak. Perhaps a more plausible explanation for this feature is that of four-coordinated Sb³⁺, which bond-valence calculations would place at 2.079 Å, and could be considered as a relaxed form of the 2+2 pseudo-trigonal bipyramids found in Sb₂O₄ [27, 28]. Four-coordinated Sb⁵⁺ would be expected to have a bond length of 1.859 Å and therefore does not seem a likely explanation.

The total B–O coordination number peaks at $x \approx 0.5$ before dropping off sharply (Fig. 5-14). This is broadly similar to the N_4 values reported by other authors [1, 4, 6], but suggests a slightly more rapid decline in the proportion of [BO₄] units at high x —however, since coordination numbers calculated from neutron diffraction are usually underestimated, the difference from literature values is smaller than may be apparent in the figure. Furthermore, neutron diffraction is probably a less suitable technique than, for example, quantitative NMR, for the accurate detection of four-coordinated boron in such small quantities (as indicated by the error bars in Figure 5-14) and therefore, in the absence of further evidence, the literature values seem more believable.

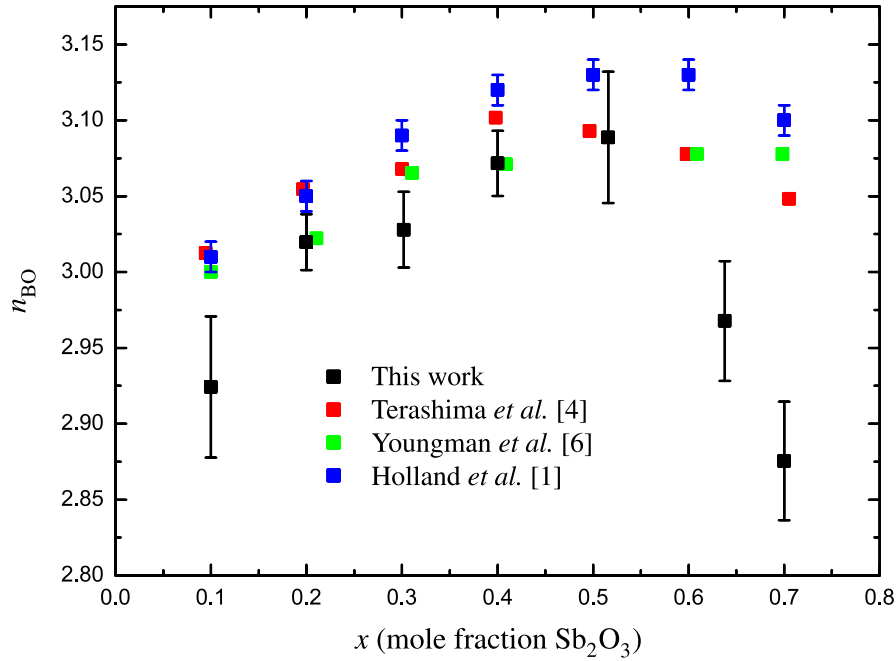


Figure 5-14 The total B–O coordination numbers for the antimony borate samples, compared with those calculated from the literature [1, 4, 6]. The x values used for the data from this work are those judged to be most plausible.

5.4.4 Simulating the total correlation function

Using neutron diffraction data from ν -B₂O₃ [18] and ν -Sb₂O₃ (*q.v.* §4.4.1), it is possible to draw a comparison between the measured total correlation function of an antimony borate glass and the simulated $T(r)$ for a stoichiometrically-equivalent mixture of the two end-members (Fig. 5-15) using the equation

$$T(r) = \frac{N_1}{N_1 + N_2} T_1(r) + \frac{N_2}{N_1 + N_2} T_2(r) \quad (5-1)$$

where N_i and $T_i(r)$ are the number of atoms in phase i and the total correlation function for a pure sample of phase i , respectively. This approach has previously been used by Hannon *et al.* [29] to simulate a lead aluminate crystal that contained some impurities. There are some flaws to this method, such as the absence of correlations between the atoms in the two phases, but the model should be reasonably accurate in terms of short-range order and thus highlight any changes due to formation of the binary glass. As might be expected, the B–O correlation is slightly narrower and sharper in the simulated $T(r)$, since ν -B₂O₃ does not contain any [BO₄] tetrahedra [9, 25]; the subsequent O_B...O_B peak is similarly narrow due to the absence of the longer oxygen-oxygen distance of the [BO₄] units. The first Sb–O correlation of the simulation also

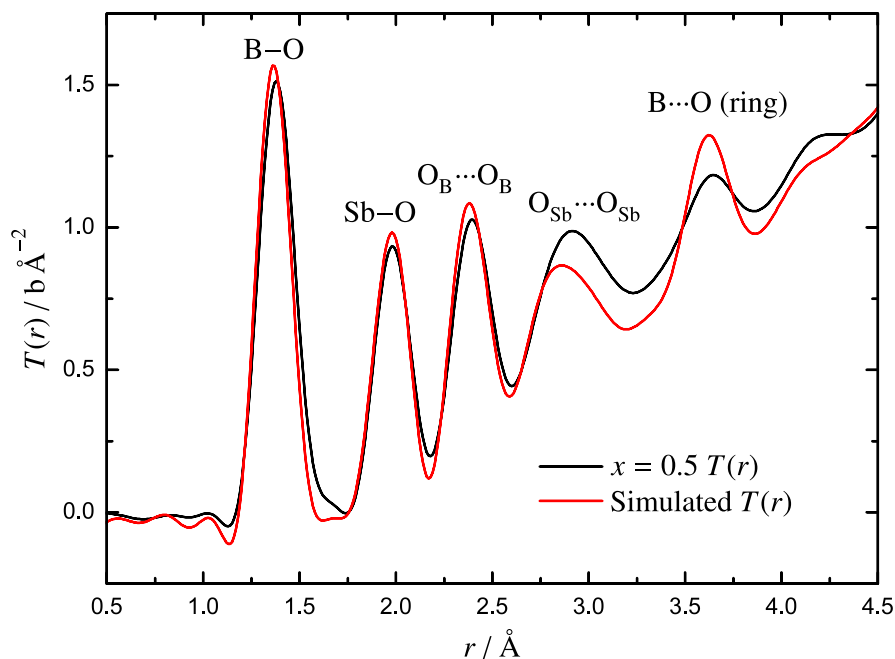


Figure 5-15 The $T(r)$ of the (nominal) $x = 0.5$ sample compared with one simulated by summing weighted ν - B_2O_3 [18] and ν - Sb_2O_3 (*q.v.* §4.4.1) total correlation functions. All datasets were Fourier transformed at $Q_{\max} = 30 \text{ \AA}^{-1}$. Labels are the primary correlations giving rise to the peaks, secondary contributions are described in the main text.

differs from the measured function, with the actual sample exhibiting a less intense main peak together with more intensity at greater r : this indicates that the proportion of more highly-coordinated antimony oxide units (probably $[Sb^{3+}O_4]$ pseudo-trigonal bipyramids) is greater in the binary borate glass than in the ν - Sb_2O_3 sample.

Most notably, the model considerably underestimates the intensity observed in the region beyond the $O_{Sb} \cdots O_{Sb}$ peak (approximately 2.8 \AA to 3.4 \AA). In the system end-members, this region is dominated by correlations in the B_2O_3 network (*q.v.* Fig. 5-5), specifically the $B \cdots O$ distances that lie across and between boroxol rings (r_4 and r_5 in Figure 5-7, respectively). However, as can be seen from the reduced intensity of the peak at 3.6 \AA , there are far fewer boroxol rings remaining in the glass system than the model predicts (consistent with the sharp reduction in the breathing mode peak in the Raman data, *q.v.* §5.2)—therefore, the intensity in the underestimated region must arise from another source. The quantities of $[BO_4]$ and $[SbO_4]$ units in the glass are too low to account for such a strong correlation. The most obvious explanation would seem to be an interaction between the B_2O_3 and Sb_2O_3 in the glass, for which the simulated $T(r)$ does not account.

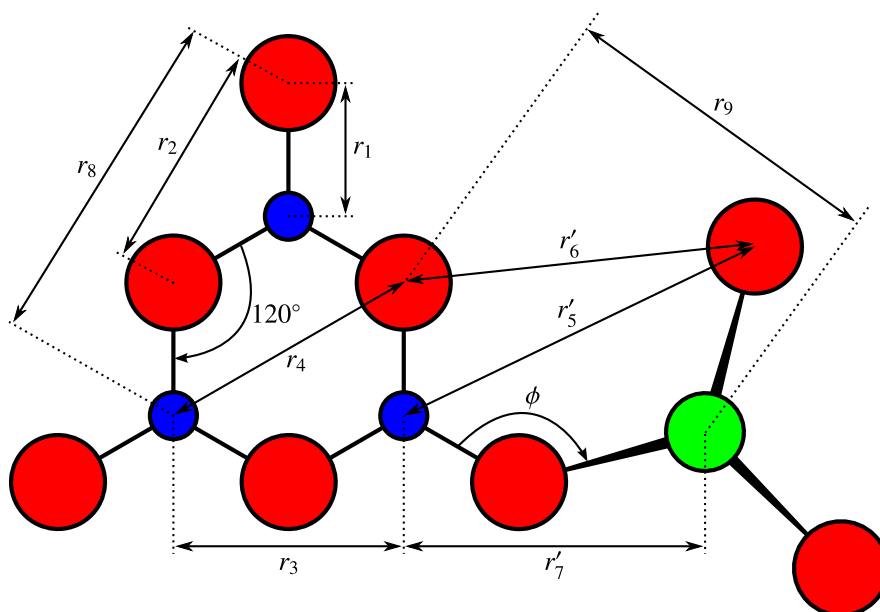


Figure 5-16 The interatomic distances within a $[\text{B}_3\text{O}_6]$ boroxol ring; also shown is an attached $[\text{SbO}_3]$ trigonal pyramid at an angle ϕ . Blue atoms are boron, red are oxygen, green are antimony. Note that the $[\text{SbO}_3]$ unit is not planar.

Figure 5-16 is a modification of the earlier diagram of a boroxol ring (Fig. 5-7) with an attached $[\text{SbO}_3]$ trigonal pyramid instead of a $[\text{BO}_3]$ triangle. In addition to the $\text{B}\cdots\text{Sb}$ correlation (r'_7), the presence of the larger antimony oxide unit gives rise to two new $\text{X}\cdots\text{O}$ distances: from the boron atom to the next-nearest oxygen (NNO) on the attached $[\text{SbO}_3]$ unit (r'_5) and similarly from the antimony atom to the NNO on the $[\text{BO}_3]$ triangle (r_9), as well as the $\text{O}_\text{B}\cdots\text{O}_\text{Sb}$ distance between these two oxygen atoms themselves (r'_6). The $\text{B}-\text{O}-\text{Sb}$ angle ϕ and the non-planar character of the $[\text{SbO}_3]$ unit permit these three new correlations to occupy a considerable range of distances. Therefore, the additional intensity observed after the $\text{O}_\text{Sb}\cdots\text{O}_\text{Sb}$ peak in the measured correlation functions may arise from any or all of the above.

The differences between the experimental and simulated total correlation functions in the ' $\text{O}_\text{Sb}\cdots\text{O}_\text{Sb}$ to $\text{B}\cdots\text{O}$ (ring)' region are prevalent throughout the compositional range studied (Fig. 5-17). This indicates that the $[\text{SbO}_3]$ units are introduced in a reasonably homogeneous distribution throughout the borate network, displacing the smaller $[\text{BO}_3]$ triangles and cleaving boroxol rings. However, as noted earlier in §5.4.1, the persistence of the boroxol ring peak at 3.6 \AA does indicate that $[\text{B}_3\text{O}_6]$ structures continue to be present up to $x = 0.7$, beyond the point where totally homogeneous mix-

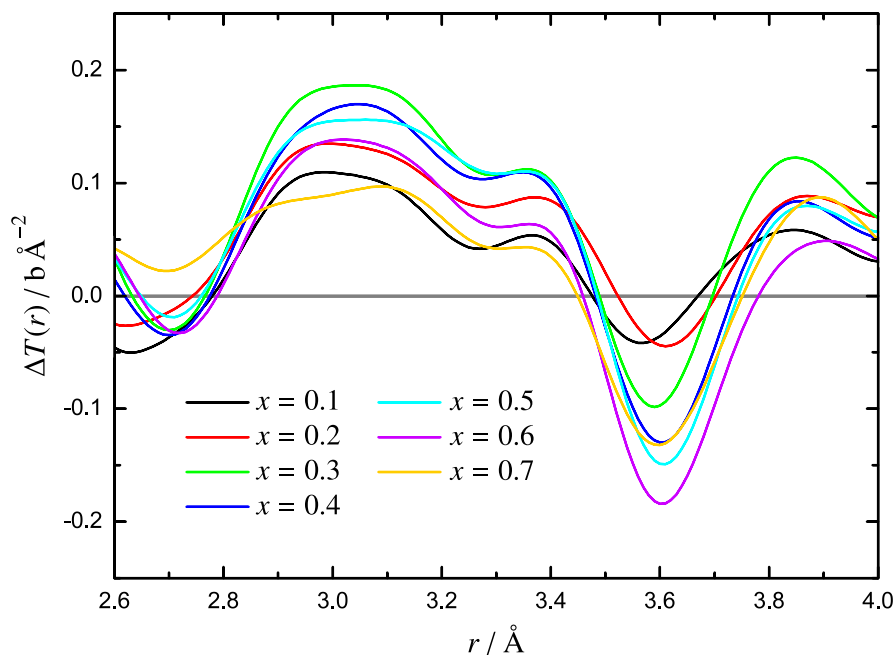


Figure 5-17 The difference between the experimental and simulated total correlation functions for the antimony borate glasses. Positive values indicate more intensity present in the actual experimental data than in the simulation, and conversely for negative values.

ing of the $[\text{BO}_3]$ and $[\text{SbO}_3]$ units becomes possible ($x = 0.5$). Therefore it appears that some Sb–O–Sb linkages are retained at high x , but this effect does not seem to induce a heterogeneous distribution of structural units in the glass at low x .

Further evidence to support this theory is offered by the boroxol ring peak, where the experimental $T(r)$ consistently exhibits lower intensity than the simulation. Whilst this is consistent with a model that does not consider interactions between the antimony oxide and borate units, a steady negative trend in $\Delta T(r)$ would be expected, whilst in fact $\Delta T(r)$ for $x = 0.7$ is less negative than the value at $x = 0.6$. This indicates that a large proportion of the antimony oxide units introduced between these two compositions have formed Sb–O–Sb links, rather than disrupt the remaining $[\text{B}_3\text{O}_6]$ rings.

5.4.5 Conclusions

Despite lacking accurate knowledge of the sample compositions, these results show with some certainty that the B_2O_3 in the glass system forms predominantly planar trigonal $[\text{BO}_3]$ units of bond length 1.371 \AA —borne out by the O–B–O angle of 120.4° calculated from this length and the $\text{O}_\text{B} \cdots \text{O}_\text{B}$ peak position—whilst the presence of a

second B–O peak at 1.477 Å (Fig. 5-10) and the total n_{BO} obtained for the samples (Fig. 5-14) confirm that a small proportion of $[\text{BO}_4]$ tetrahedral units also exist in the glass structure, the quantity increasing with composition up to $x \approx 0.5$ and falling thereafter, confirming the findings of previous authors [1, 4, 6]. The Sb_2O_3 present in the glass forms mainly $[\text{SbO}_3]$ trigonal pyramids, as in the two crystalline polymorphs of Sb_2O_3 , whilst the presence of a second Sb–O distance (first distinguishable at $x = 0.4$ at a distance of 2.08 Å, and moving to higher r with increasing x) together with the total Sb–O coordination number indicate the presence of additional antimony oxide units that are coordinated with more than three oxygen atoms.

The most plausible candidate for these units would appear to be $[\text{Sb}^{3+}\text{O}_4]$ pseudo-trigonal bipyramids of bond length 2.08 Å (as calculated from bond-valence parameters), which could be regarded as relaxed versions of the 2+2 units found in Sb_2O_4 . The Sb^{5+} content determined by Mössbauer spectroscopy [1] may be present as $[\text{Sb}^{5+}\text{O}_6]$ octahedra similar to those found in Sb_2O_4 and Sb_2O_5 , but relaxed to be closer to the bond-valence prediction of 2.01 Å for six-coordinated Sb^{5+} , which would also conceal the resulting correlation peak beneath the one corresponding to the $[\text{SbO}_3]$ trigonal pyramids. However, the total Sb–O coordination numbers obtained for the samples are not consistent with a large quantity of $[\text{SbO}_4]$ units: merely assigning all of the Sb^{5+} detected by Mössbauer spectroscopy to $[\text{Sb}^{5+}\text{O}_6]$ octahedra accounts for much of the measured values (*q.v.* Table 5-6).

There is also evidence that the antimony oxide units introduced into the borate network with increasing x initially distribute themselves homogeneously by breaking boroxol rings, but later retain some Sb–O–Sb connections, allowing B_3O_6 structures to persist long after a totally homogeneous mixing of the two glass networks becomes possible. This effect may be due to the presence of the more highly-coordinated $[\text{Sb}^{5+}\text{O}_6]$ octahedra which are more easily accommodated by the non-planar $[\text{SbO}_3]$ units than by displacing the planar $[\text{BO}_3]$ triangles.

5.5 Summary

A number of ^{11}B -enriched antimony borate glasses ($x\text{Sb}_2\text{O}_3 \cdot (1-x)\text{B}_2\text{O}_3$) previously studied by Holland *et al.* [1] were studied using various techniques, including EDX

analysis, Raman spectroscopy, density measurements and neutron diffraction. EDX data confirmed that the samples did not contain any substantial contaminants, whilst the Raman spectra supported previous findings [4, 6] as to a structure primarily consisting of boroxol rings being cleaved by the introduction of Sb^{3+} ions.

Density measurements largely agreed with the literature data when plotted against nominal compositions, but showed discrepancies for two samples when using the x values obtained by quantitative NMR [1]. Neutron diffraction data were ultimately analysed using both sets of compositions and x values were determined by a set of criteria based on predictions from other techniques and trends apparent in the data.

The B–O correlation was fitted with two peaks, at the distances expected for three- and four-coordinated boron, showing a maximum value of N_4 at $x \approx 0.5$ and falling thereafter, consistent with previous findings in the literature, whilst the O–B–O angle indicates that the three-coordinated boron is present predominantly as planar trigonal units: the distinctive peak at 3.6 Å in $T(r)$ suggests that these units are largely organised into boroxol rings as in $\nu\text{-B}_2\text{O}_3$. The total Sb–O coordination number remains fairly constant at ~ 3.25 throughout the compositional range studied, this total arising from fitting two peaks to the first Sb–O correlation. The peak positions indicate that a majority of the antimony occupies $[\text{SbO}_3]$ trigonal pyramids, with a minority of $[\text{Sb}^{3+}\text{O}_4]$ pseudo-trigonal bipyramids also present. Whether $[\text{Sb}^{5+}\text{O}_6]$ octahedra also occur is less clear, since the bond length is expected to be very similar to that of the $[\text{SbO}_3]$ trigonal pyramids, but this seems to be the only explanation for the structural role of the Sb^{5+} detected by Mössbauer spectroscopy.

Simulating the total correlation functions of the antimony borate system by combining weighted $\nu\text{-B}_2\text{O}_3$ and $\nu\text{-Sb}_2\text{O}_3$ data demonstrated that antimony oxide units initially mix homogeneously with the boroxol rings at low x , but as more Sb_2O_3 is added Sb–O–Sb linkages are retained—this may be due to the need to accommodate increasing numbers of $[\text{Sb}^{5+}\text{O}_6]$ octahedra in the network. This effect also means that boroxol rings persist in the glass structure long after the borate and antimony oxide networks could have mixed homogeneously.

References

- [1] D. Holland, A. C. Hannon, M. E. Smith, C. E. Johnson, M. F. Thomas and A. M. Beesley, *Solid State Nucl. Mag.* **26**, (2004), 172–179.
- [2] D. Holland, (personal communication) (2008).
- [3] E. R. Barney, *The Structural Role of Lone Pair Ions in Novel Glasses*, PhD Thesis, University of Warwick (2008).
- [4] K. Terashima, T. Hashimoto, T. Uchino, S.-H. Kim and T. Yoko, *J. Ceram. Soc. Jpn.* **104** (11), (1996), 1008–1014.
- [5] J. Goubeau and H. Keller, *Z. Anorg. Allg. Chem.* **272** (6), (1953), 303–312.
- [6] R. E. Youngman, S. Sen, L. K. Cornelius and A. J. G. Ellison, *Phys. Chem. Glasses* **44** (2), (2003), 69–74.
- [7] B. N. Meera and J. Ramakrishna, *J. Non-Cryst. Solids* **159**, (1993), 1–21.
- [8] G. D. Chryssikos, E. I. Kamitsos and W. M. Risen Jr., *J. Non-Cryst. Solids* **93**, (1987), 155–168.
- [9] P. A. V. Johnson, A. C. Wright and R. N. Sinclair, *J. Non-Cryst. Solids* **50**, (1982), 281–311.
- [10] A. C. Hannon, D. I. Grimley, R. A. Hulme, A. C. Wright and R. N. Sinclair, *J. Non-Cryst. Solids* **177**, (1994), 299–316.
- [11] E. Kordes, *Z. Phys. Chem.* **B43**, (1939), 173–190.
- [12] M. Imaoka, H. Hasegawa and S. Shindo, *J. Ceram. Soc. Jpn.* **77** (8), (1969), 263–271.
- [13] N. Mochida and K. Takahashi, *J. Ceram. Soc. Jpn.* **84** (9), (1976), 413–420.
- [14] T. Honma, Y. Benino, T. Komatsu, R. Sato and V. Dimitrov, *J. Chem. Phys.* **115** (15), (2001), 7207–7214.
- [15] S. Chatlani and J. E. Shelby, *Phys. Chem. Glasses-B* **47** (3), (2006), 288–293.
- [16] A. C. Hannon, *Nucl. Instrum. Meth. A* **551** (1), (2005), 88–107.
- [17] A. C. Hannon and D. Holland, (personal communication) (2007).

-
- [18] E. R. Barney, (personal communication) (2008).
- [19] N. E. Brese and M. O’Keeffe, *Acta Crystallogr. B* **47**, (1991), 192–197.
- [20] A. C. Hannon and J. M. Parker, *J. Non-Cryst. Solids* **274**, (2000), 102–109.
- [21] A. G. Clare, G. Etherington, A. C. Wright, M. J. Weber, S. A. Brawer, D. D. Kingman and R. N. Sinclair, *J. Chem. Phys.* **91**, (1989), 6380–6392.
- [22] W. S. Howells, A. K. Soper and A. C. Hannon, *Report RAL-90-041*, Tech. rep., Rutherford Appleton Laboratory (1990).
- [23] C. Svensson, *Acta Crystallogr. B* **31**, (1975), 2016–2018.
- [24] C. Svensson, *Acta Crystallogr. B* **30**, (1974), 458–461.
- [25] R. L. Mozzi and B. E. Warren, *J. Appl. Cryst.* **3**, (1970), 251–257.
- [26] V. M. Jansen, *Acta Crystallogr. B* **35** (3), (1979), 539–542.
- [27] P. S. Gopalakrishnan and H. Manohar, *Cryst. Struct. Commun.* **4**, (1975), 203–206.
- [28] J. Amador, E. Gutiérrez Puebla, M. A. Monge, I. Rasines and C. Ruiz Valero, *Inorg. Chem.* **27** (8), (1988), 1367–1370.
- [29] A. C. Hannon, E. R. Barney, D. Holland and K. S. Knight, *J. Solid State Chem.* **181**, (2008), 1087–1102.

Chapter 6

Antimony Silicate Glasses

6.1 Sample preparation and characterisation

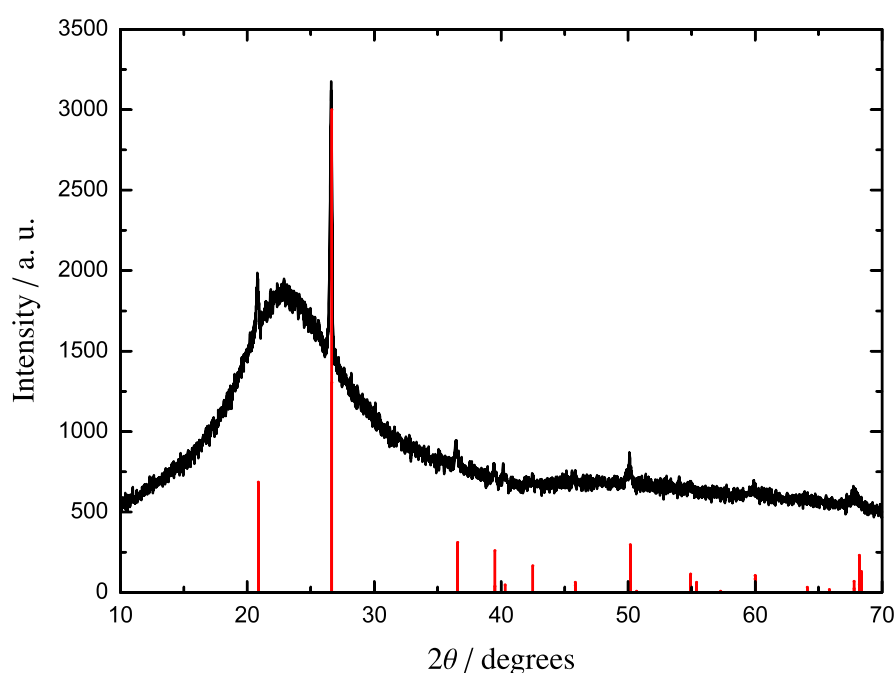
The antimony silicate glasses used in this work were prepared in collaboration with Mr Bruce Davies and Mr Martin Mee, final-year undergraduate project students at the University of Warwick. Mixtures of nominal composition $x\text{Sb}_2\text{O}_3 \cdot (1 - x)\text{SiO}_2$ with $x = 0.1, 0.3, 0.5, 0.55$ and 0.8 of Sb_2O_3 (99.6 %, Alfa Aesar) and Wacomsil quartz (SiO_2 , 99.9 %), were heated in lidded, fused quartz crucibles in a furnace to 1200°C (for $x = 0.8$ and $x = 0.55$), 1400°C (for $x = 0.5$ and $x = 0.3$) or 1600°C (for $x = 0.1$), and held at that temperature for (typically) 15 min until molten and well-mixed. The $x = 0.55$ and $x = 0.8$ melts were splat-quenched between two steel plates, whilst the remainder were air-cooled in the crucibles. For simplicity the nominal compositions are used throughout this work to identify the samples.

EDX of freshly-powdered samples was used to estimate the final glass compositions. Three measurements were obtained from different areas of each sample and an average was taken in an attempt to improve accuracy; the results are shown in Table 6-1. The two glasses with the lowest antimony content phase-separated on cooling: the phases in the $x = 0.3$ sample were manually separated and the one closest to the nominal composition was used for further analysis. Only a minority of the $x = 0.1$ preparation phase-separated, but this material was well-dispersed throughout the larger phase and so the two could not be divided into distinct samples.

X-ray diffraction confirmed that the $x = 0.3, 0.5, 0.55$ and 0.8 samples were fully amorphous within the limits of detection, but also that the $x = 0.1$ sample exhibited several crystalline peaks from α -quartz (Fig. 6-1). This was probably a result of the low temperature used—a limitation of the available equipment—since the melting point of silica is $\sim 1600^\circ\text{C}$ and too viscous a melt may not have mixed well with the antimony trioxide; it is probable that the crystals are present in the dispersed minority phase of

Table 6-1 The antimony silicate glass compositions as determined by EDX.

Nominal mol% Sb_2O_3 (± 0.5)	Individual mol% Sb_2O_3 measurements (± 2.0)			Mean mol% Sb_2O_3 (± 2.0)
	1st	2nd	3rd	
10.0	10.5	10.1	10.2	10.3
30.0	35.9	31.3	32.9	33.4
50.0	51.5	47.3	51.2	50.0
55.0	64.0	64.4	63.1	63.8
80.0	81.1	80.6	79.2	80.3

**Figure 6-1** The XRD pattern of the $x = 0.1$ antimony silicate glass, run for 16 h. Red lines are generated from the α -quartz crystal data of Machatschki [1], obtained from the ICSD [2]. Excepting the Bragg peaks, the broad amorphous hump is also typical of the other samples.

the sample noted above.

Glass transition temperatures for a range of antimony silicate glass samples prepared at the same time and in the same fashion as those described above were measured by Davies [3] and Mee [4] (Fig. 6-2). The values of T_g show a steady negative trend with decreasing SiO_2 content, similar to the behaviour of binary germanosilicate glasses [5]; this may indicate that a similar, nearly-random mixing of the two glass-forming networks [6] occurs in the antimony silicate system.

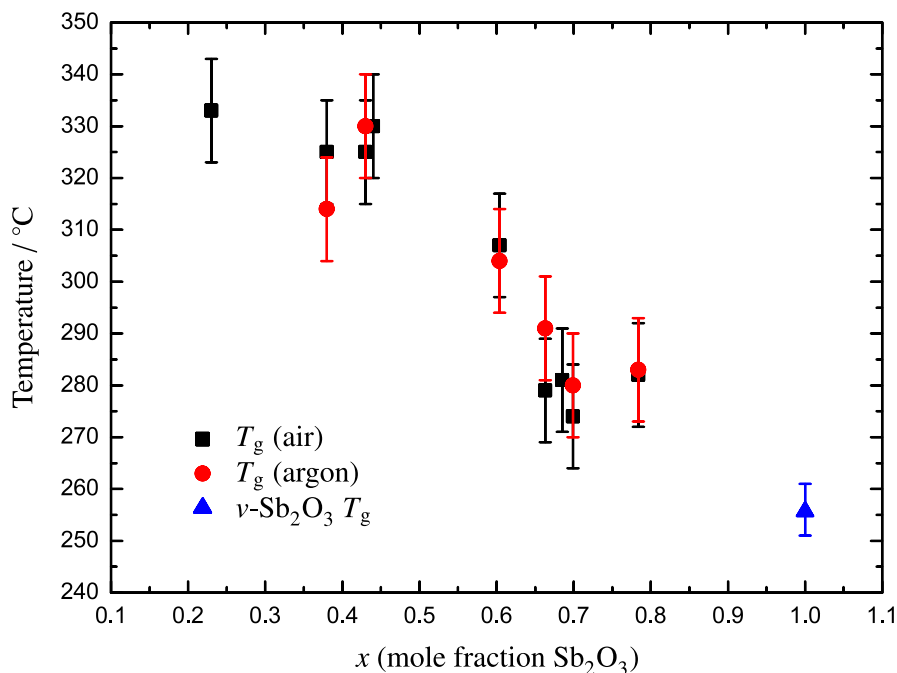


Figure 6-2 Values of T_g measured under air and argon for other antimony silicate glass samples [3, 4], contemporary with those studied in this work. Also shown is the glass transition temperature measured for the Sb_2O_3 glass (*q.v.* §4.2.1). The x values plotted for the antimony silicates are those determined by EDX analysis.

Mössbauer spectroscopy was also used to determine the ratio of Sb^{5+} to Sb^{3+} in the same range of contemporary samples (Fig. 6-3), together with cervantite (crystalline Sb_2O_4), which contains equal amounts of the two oxidation states [7, 8], as a reference; these measurements were performed by Dr Mike Thomas at the University of Liverpool. The cervantite measurement at 77 K confirmed that 50 % of the Sb in the crystal was Sb^{5+} , indicating that the results obtained for the glass samples at 77 K should be reasonably accurate, although f -factors were not determined.

To obtain estimates for the proportion of Sb^{5+} present in the glasses discussed in this work, values were interpolated from a line of best fit to the measured data, using the compositions determined by EDX (Table 6-1). The (nominal) $x = 0.55$ and $x = 0.8$ samples studied in this work were two of the samples measured by Mössbauer spectroscopy; for the former it is noticeable that it deviates considerably from the line when plotted with the EDX-derived composition, whereas the nominal value would place it much closer. This suggests that the EDX analysis is inaccurate. Of course, the presence of Sb^{5+} in the glass samples will make a difference to the compositions calculated from EDX measurements, since these presumed a straight mixture of SiO_2 with Sb_2O_3 .

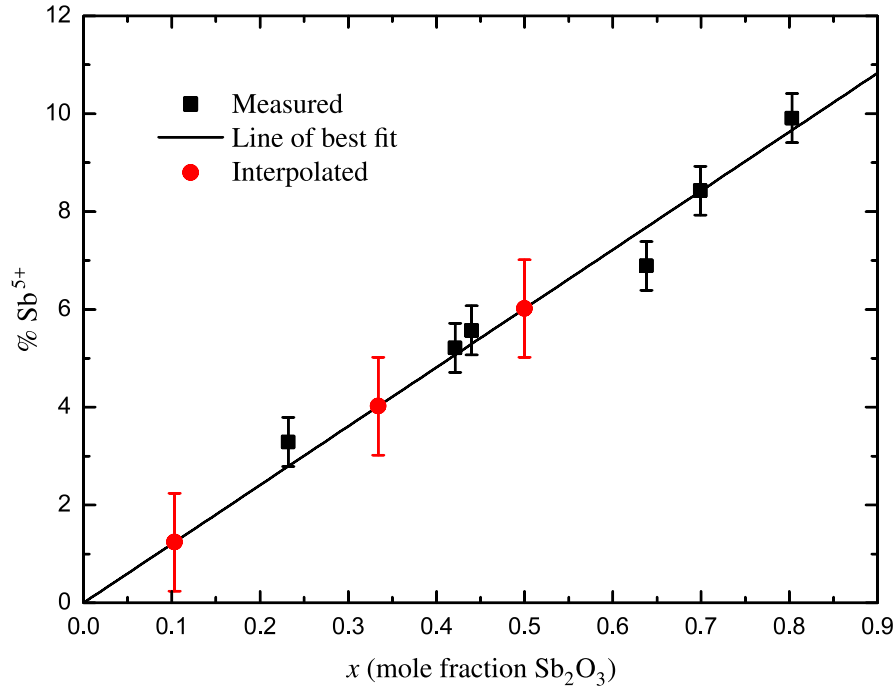


Figure 6-3 The percentage of Sb present as Sb^{5+} in the antimony silicate glasses used for neutron diffraction, interpolated from Mössbauer data measured by Dr Mike Thomas from the University of Liverpool on samples contemporary with those studied in this work. x values plotted are those determined by EDX analysis. Note that the $x = 0.638$ and $x = 0.803$ samples measured directly are also those investigated in this work.

However, this discrepancy is entirely negligible: re-analysing the EDX spectrum for the $x = 0.8$ sample assuming that *all* antimony atoms are present as Sb_2O_5 —ten times what the Mössbauer results indicate—results in an increase of only 3×10^{-4} in the value of x obtained. Therefore the reason for the apparent inaccuracy in the EDX analysis of the (nominal) $x = 0.55$ sample remains unclear.

6.2 Density measurements

The measured densities for the antimony silicate glasses are shown in Figure 6-4 compared with the values for vitreous silica and for the Sb_2O_3 glass (*q.v.* §4.3), as well as a line calculated by assuming that the molar volume increases linearly with x from the value for $v\text{-SiO}_2$ to that of the Sb_2O_3 glass. The measured values are higher than those reported previously by Datta *et al.* [9], probably because the samples in the earlier study were made by a sol-gel method, rather than melt-quenching, which is likely to have resulted in additional components (e.g. water, organics) entering the glass structure.

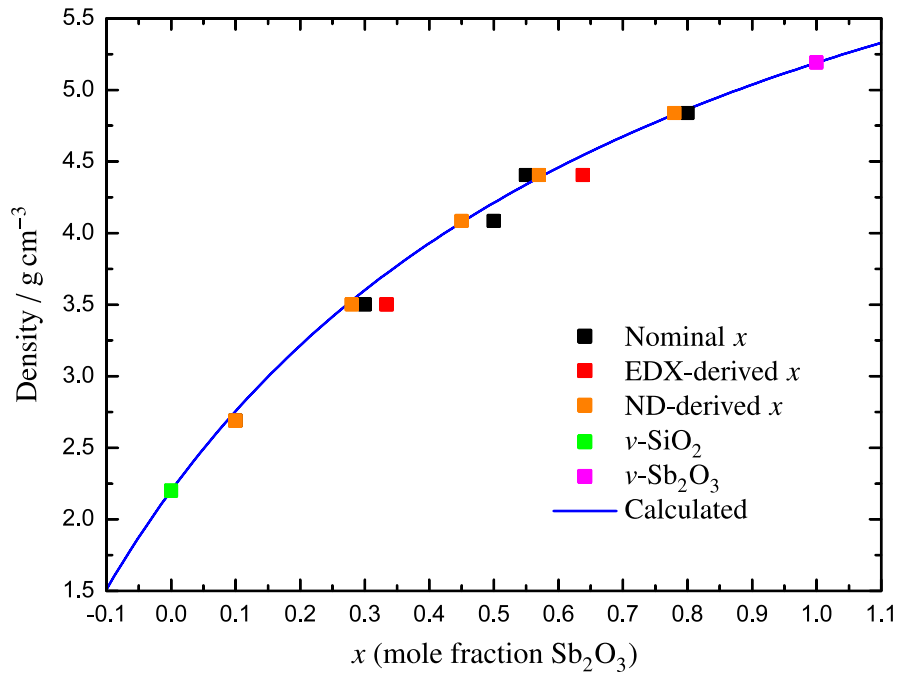


Figure 6-4 The densities measured for the antimony silicates, compared with the values for vitreous silica and for the Sb_2O_3 glass investigated earlier (*q.v.* §4.3). Also shown is a line calculated by assuming a linear increase in molar volume with composition. Error bars are smaller than the symbols used. Sample values from this work are plotted against nominal x , EDX compositions where there is a significant difference, and the x values determined in §6.3.3 from neutron diffraction data.

The measured densities show very good agreement with the calculated line (particularly when plotted against the compositions determined from neutron diffraction; *q.v.* §6.3.3), suggesting that the two glass networks appear to mix without significantly affecting each other, possibly indicating a degree of phase separation. However, only a single glass transition temperature was observed for each sample in studies of antimony silicate glasses contemporary with those examined here [3, 4] (*q.v.* §6.1), suggesting that phase separation has not in fact taken place.

6.3 Neutron diffraction

6.3.1 Total correlation functions

Neutron diffraction data were collected on the GEM diffractometer [10] at the ISIS pulsed neutron source. Vanadium cans of diameter 8.3 mm and wall thickness 25 μm were used to hold all of the samples except for the $x = 0.1$ glass, which required a

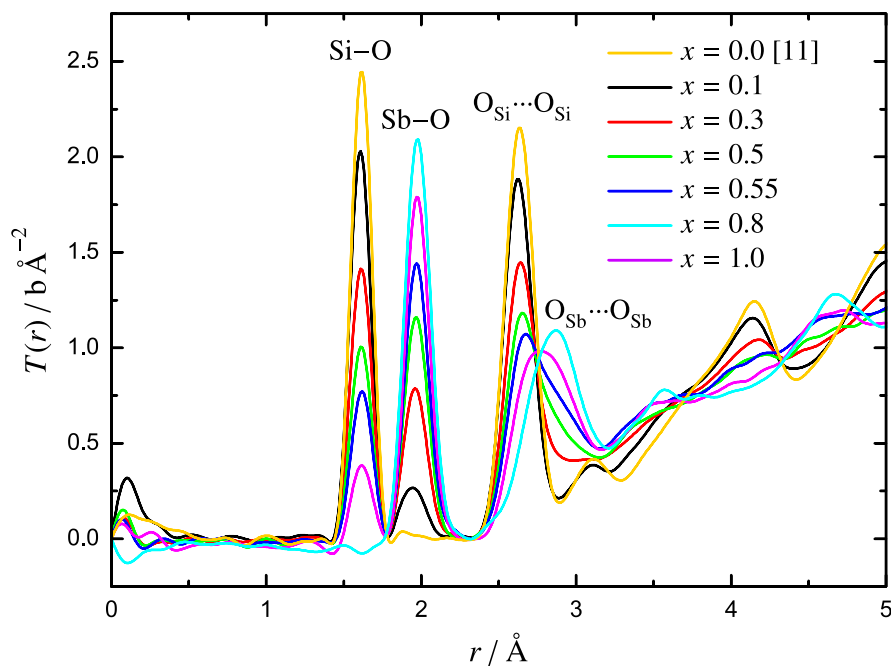


Figure 6-5 The total correlation functions $T(r)$ produced from the neutron diffraction data of the antimony silicates using the nominal x values. Also shown are data from vitreous silica [11] and from the Sb_2O_3 glass (*q.v.* §4.4.1), the latter processed with a lower Q_{max} of 35 \AA^{-1} : this will result in wider peaks with reduced intensity compared to the samples.

can of diameter 6.0 mm due to the limited quantity of material available. The signal-to-noise ratio of the data was sufficient to allow a Q_{max} of 40 \AA^{-1} for the Fourier transform, and the total correlation functions, obtained from the nominal batch compositions, are shown in Figures 6-5 and 6-6. Small Bragg peaks were noticeable in $S(Q)$ for the $x = 0.1$ sample, consistent with the XRD data found earlier (*q.v.* §6.1); since the crystal phase was identified as α -quartz, the Si–O coordination may tend towards 4.00, but as silicate glasses almost invariably consist of $[\text{SiO}_4]$ tetrahedra this is unlikely to make a significant difference to the neutron diffraction analysis.

The peaks in the total correlation functions are well-defined and can be readily assigned to specific atom-atom correlations. The first peak at $\sim 1.60 \text{ \AA}$ is the Si–O correlation, consistent with the distance for four-coordinated silicon (1.624 \AA) that can be calculated from bond-valence parameters [12, 13]. The second peak at $\sim 1.97 \text{ \AA}$ arises from Sb–O, as observed previously in the Sb_2O_3 glass (*q.v.* §4.4.1), whilst the third and fourth peaks at $\sim 2.62 \text{ \AA}$ and $\sim 2.86 \text{ \AA}$ arise from $\text{O}_{\text{Si}} \cdots \text{O}_{\text{Si}}$ and $\text{O}_{\text{Sb}} \cdots \text{O}_{\text{Sb}}$ correlations, respectively. As evident in Figure 6-5, peak areas also change with composition in line with these assignments.

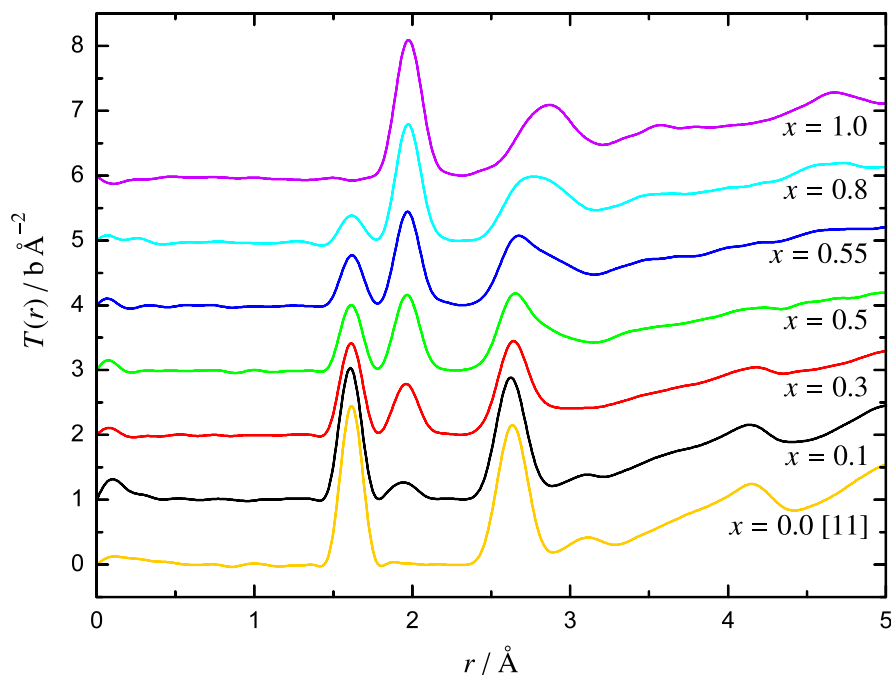


Figure 6-6 The $T(r)$ data from Figure 6-5 with each dataset offset by $1 \text{ b } \text{\AA}^{-2}$ on the y-scale.

Dividing $T(r)$ by the Si–O partial correlation coefficient yields a scaled $t_{\text{Si-O}}(r)$ correlation function that allows the Si–O environment to be directly compared between samples (Fig. 6-7). Since the presence of four-coordinated silicon in silicate glasses is well-established in the literature [14], and because the symmetrical shape of the peaks imply only a single coordination environment, it should be expected that the first Si–O peak will be invariant with composition—however, this is not the case. The variation in peak heights does not appear to follow an obvious pattern, which indicates that the most likely cause of the discrepancy is the use of incorrect compositions when processing the data (the $x = 0.8$ sample is most sensitive to this, due to the low value of the Si–O coefficient). However, the compositions determined earlier by EDX (*q.v.* §6.1) are also not entirely supported, since that data suggested that the values for the $x = 0.1$, $x = 0.5$ and $x = 0.8$ samples were at essentially the nominal values, whereas these three in fact show the greatest discrepancy in the scaled correlation function.

Scaling $T(r)$ by the Sb–O coefficient shows a similar disparity in the first Sb–O correlation (Fig. 6-8). However, in this case the cause is less obvious: a slight asymmetry to the peak on the greater- r side suggests two distinct bond length distributions are present, as previously observed for the Sb_2O_3 glass (*q.v.* §4.4.1), with the intensity

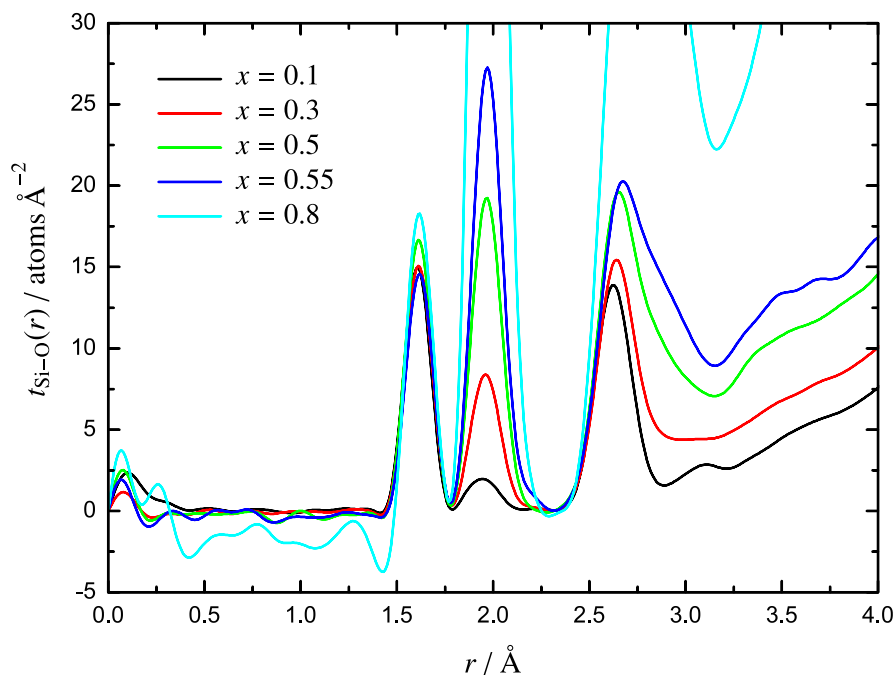


Figure 6-7 The weighted total correlation function for the antimony silicates, obtained by dividing $T(r)$ by the Si–O partial correlation coefficient. x values used are from the nominal batch compositions.

of the greater- r peak growing with increasing x . Whilst this might be expected to reduce the height of the combined peak as area is ‘transferred’ to the greater- r peak, the opposite is in fact observed, suggesting that either the overall antimony coordination is steadily increasing with composition, or that the wrong x values were used to process the data; given the evidence from $t_{\text{Si-O}}(r)$ in Figure 6-7, the latter explanation seems most likely.

6.3.2 Peak-fitting

A comparison of the residuals from fitting Sb–O with either one or two peaks (Fig. 6-9) confirms that a second, smaller peak is present at greater- r , although this feature is either not present or too small to be fitted for the $x = 0.1$ sample. Coordination numbers obtained from the fitted peaks support the conclusion that the wrong composition has been used for processing the data (Table 6-2): for example, n_{SiO} varies from 3.85(4) to 4.48(15) between samples, and even when approaching the expected number, as for the $x = 0.3$ glass, n_{SbO} then assumes a value of 2.73(3) that is considerably lower than that seen in the Sb_2O_3 glass (*q.v.* §4.4.1) or in the crystalline polymorphs of antimony

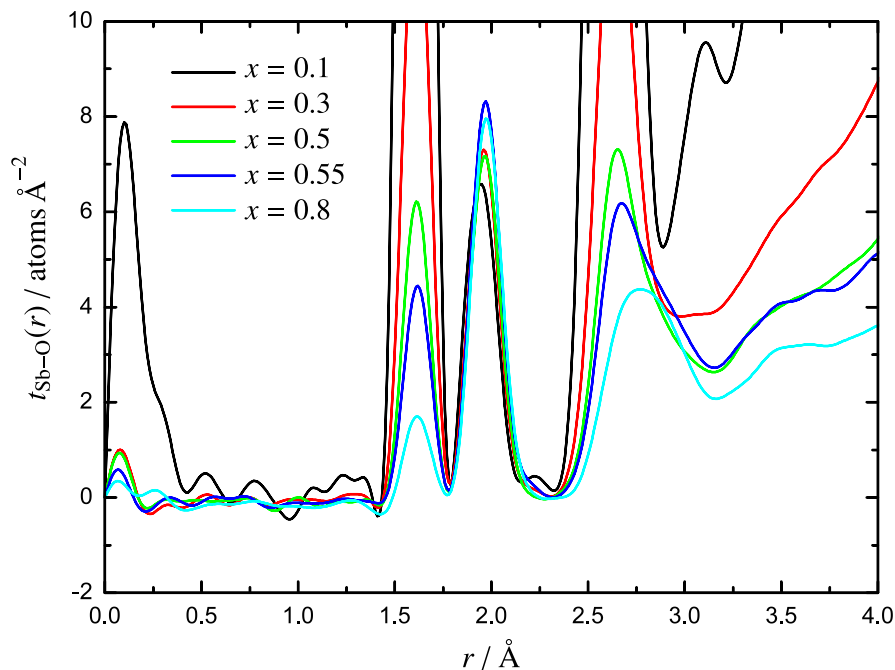


Figure 6-8 The weighted total correlation function for the antimony silicates, obtained by dividing $T(r)$ by the Sb–O partial correlation coefficient. x values used are from the nominal batch compositions.

Table 6-2 Coordination numbers and bond lengths obtained from peaks fitted to $T(r)$ of the antimony silicate samples, using nominal x values. Errors quoted are the statistical errors from fitting the peaks; note that the error on the total n_{SbO} is actually from a single-peak fit, since this is deemed more plausible (see main text).

x	r_{SiO} (Å)	n_{SiO}	$r_{\text{SbO}(1)}$ (Å)	$n_{\text{SbO}(1)}$	$r_{\text{SbO}(2)}$ (Å)	$n_{\text{SbO}(2)}$	Total n_{SbO}
0.1	1.607(1)	3.93(6)	1.947(8)	2.51(24)	–	–	2.51(24)
0.3	1.613(1)	4.02(2)	1.959(2)	2.57(8)	2.109(40)	0.15(8)	2.73(3)
0.5	1.613(1)	4.36(5)	1.950(12)	1.95(41)	2.030(15)	0.70(41)	2.66(3)
0.55	1.618(1)	3.85(4)	1.969(1)	2.92(5)	2.121(17)	0.21(4)	3.13(2)
0.8	1.619(2)	4.48(15)	1.966(5)	2.53(22)	2.062(19)	0.45(23)	2.99(2)

trioxide.

Note that the error on the total n_{SbO} is *not* the sum of the errors on $n_{\text{SbO}(1)}$ and $n_{\text{SbO}(2)}$, since this leads to unrealistic values. For example, for $x = 0.5$ the errors on each of the individual peaks are ± 0.41 leading to a value of ± 0.82 for the total n_{SbO} of 2.66. However, fitting a single peak to the Sb–O correlation gives $n_{\text{SbO}} = 2.65(3)$, albeit with a less satisfactory residual. This is because most of the error on the individual peaks in the two-peak fit arises from the relative uncertainty in assigning the area that either peak

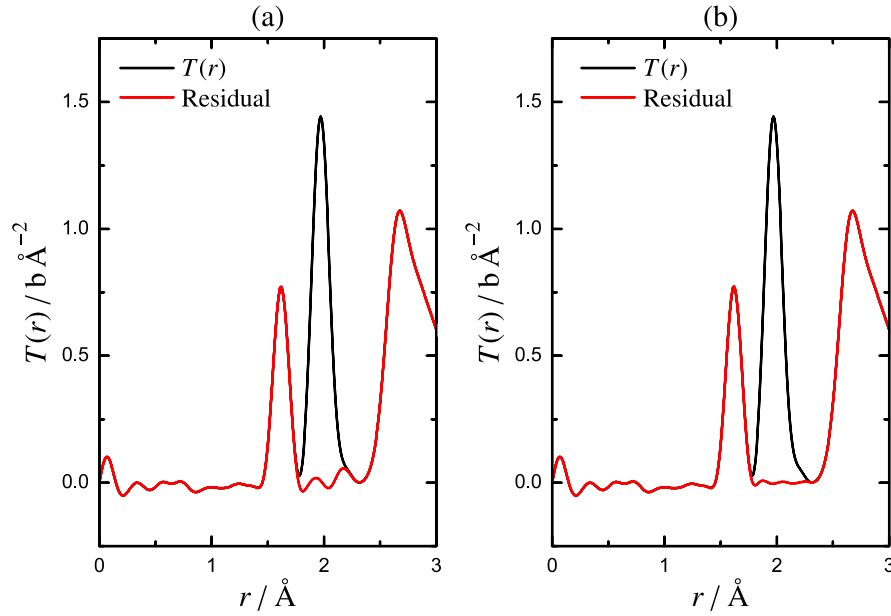


Figure 6-9 The residuals of (a) single- and (b) double-peak fits to the first Sb–O correlation for the $x = 0.55$ (nominal composition) antimony silicate sample.

could overlap; in practice if, for example, the coordination of the first peak were to be at the extreme positive end of the error range, $n_{\text{SbO}(2)}$ would tend towards an extremely low value to compensate, and vice versa. Therefore, the errors quoted throughout this chapter for the total n_{SbO} are in fact those arising from single-peak fits since they more accurately represent the actual uncertainty in the total coordination number.

Since the nominal x values appear to be largely unsuitable, the neutron data were next analysed using the compositions that were determined earlier from EDX measurements (Table 6-1). However, these compositions do not improve the coordination numbers obtained and generally make them worse (Table 6-3), indicating that the actual sample x values lie in the opposite direction.

6.3.3 Sample compositions and structural trends

In the absence of any other data that could suggest alternative x values, it is necessary to undertake a ‘trial-and-improvement’ method of determining the correct compositions. Based on the preponderance of evidence in the literature, it seems reasonable to assume that n_{SiO} will be ~ 4.00 , but since coordination numbers acquired from neutron diffraction are typically slightly lower than expected (due to the damping effect of

Table 6-3 Coordination numbers and bond lengths obtained from peaks fitted to $T(r)$ of the antimony silicate samples, using x values derived from EDX. Errors quoted are the statistical errors from fitting the peaks; note that the error on the total n_{SbO} is actually from a single-peak fit, since this is deemed more plausible (see main text).

x	r_{SiO} (Å)	n_{SiO}	$r_{\text{SbO(1)}}$ (Å)	$n_{\text{SbO(1)}}$	$r_{\text{SbO(2)}}$ (Å)	$n_{\text{SbO(2)}}$	Total n_{SbO}
0.103	1.608(1)	3.94(5)	1.950(8)	2.41(22)	—	—	2.41(22)
0.334	1.613(1)	4.18(2)	1.957(3)	2.21(11)	2.076(30)	0.19(11)	2.40(2)
0.500	1.613(1)	4.36(5)	1.950(12)	1.95(41)	2.030(15)	0.70(41)	2.66(3)
0.638	1.618(2)	4.76(10)	1.968(3)	2.49(8)	2.116(32)	0.19(8)	2.68(3)
0.803	1.619(2)	4.57(13)	1.967(5)	2.55(19)	2.065(18)	0.42(19)	2.97(2)

Fourier transforming over a finite Q -range) a value of ~ 3.95 should be achievable from the data, given the Q -space resolution and the capabilities of the instrument [15]. The Sb–O coordination is slightly harder to predict, since both Sb^{3+} and Sb^{5+} are present in some crystalline polymorphs at ~ 2.00 Å (e.g. Sb_2O_4), and the value was found earlier to be 3.24(4) for Sb_2O_3 glass (*q.v.* §4.4.1). However, it is reasonable to expect at least three oxygen atoms to be coordinated with each antimony atom at this distance, and thus to obtain an $n_{\text{SbO}} \geq 2.90$ from neutron diffraction.

From these criteria, the data was processed using different x values and fitted to obtain coordination numbers, until the most likely composition, to the nearest 1 mol%, was obtained (Table 6-4). Note that, of the compositions selected, only $x = 0.1$ does not offer a plausible n_{SbO} value. Although a lower x would improve this, it would at the same time reduce n_{SiO} which is already reasonable. Additionally, as noted in §6.1, the sample contained a small quantity of crystalline α -quartz that will also affect the analysis of the neutron data, since the antimony content of the residual glass will be underestimated. Therefore $x = 0.1$ was taken as the most useful value for the sample, given that the quartz content is undetermined.

From the values of n_{SbO} obtained by this method, it is clear that there is a slow increase in antimony coordination with composition (Fig. 6-10), consistent with the ‘ $x = 1.0$ ’ coordination number found earlier for the Sb_2O_3 glass (*q.v.* §4.4.1). Whilst this might indicate that the Sb^{5+} found to be present by Mössbauer spectroscopy (*q.v.* §6.1) is forming $[\text{Sb}^{5+}\text{O}_6]$ octahedra similar to those found in Sb_2O_4 and Sb_2O_5 , the total coordination number is too low for all Sb^{5+} to be six-coordinated (Table 6-5). Unfortunately the Sb^{5+} –O peak arising from $[\text{Sb}^{5+}\text{O}_6]$ units (2.009 Å) is not resolvable

Table 6-4 Coordination numbers obtained from peaks fitted to $T(r)$ of the antimony silicate samples, using x values obtained by ‘trial-and-improvement’: highlighted compositions are those selected to best fulfil the criteria. Errors quoted are the statistical errors from fitting the peaks; note that the error on the total n_{SbO} is actually from a single-peak fit, since this is deemed more plausible (see main text).

x	$r_{\text{SiO}} (\text{\AA})$	n_{SiO}	$r_{\text{SbO}(1)} (\text{\AA})$	$n_{\text{SbO}(1)}$	$r_{\text{SbO}(2)} (\text{\AA})$	$n_{\text{SbO}(2)}$	Total n_{SbO}
0.10 (nominal)	1.607(1)	3.93(6)	1.947(8)	2.51(24)	–	–	2.51(24)
0.103 (EDX)	1.608(1)	3.94(5)	1.950(8)	2.41(22)	–	–	2.41(22)
0.27	1.612(1)	3.91(1)	1.938(6)	2.08(19)	2.017(5)	0.99(19)	3.06(2)
0.28	1.613(1)	3.96(1)	1.957(3)	2.72(11)	2.080(26)	0.23(10)	2.95(2)
0.29	1.612(1)	3.98(1)	1.937(5)	1.88(14)	2.016(4)	0.93(14)	2.81(1)
0.30 (nominal)	1.613(1)	4.02(2)	1.959(2)	2.57(8)	2.109(40)	0.15(8)	2.73(3)
0.334 (EDX)	1.613(1)	4.18(2)	1.957(3)	2.21(11)	2.076(30)	0.19(11)	2.40(2)
0.44	1.613(1)	3.88(5)	1.952(12)	2.35(51)	2.034(20)	0.72(51)	3.06(3)
0.45	1.613(1)	3.95(4)	1.951(10)	2.26(39)	2.032(15)	0.71(40)	2.97(2)
0.46	1.613(1)	4.01(6)	1.947(12)	2.08(40)	2.030(14)	0.84(41)	2.92(3)
0.50 (nominal)	1.613(1)	4.36(5)	1.950(12)	1.95(41)	2.030(15)	0.70(41)	2.66(3)
0.55 (nominal)	1.618(1)	3.85(4)	1.969(1)	2.92(5)	2.121(17)	0.21(4)	3.13(2)
0.56	1.616(1)	3.87(4)	1.967(2)	2.83(7)	2.093(17)	0.25(7)	3.08(2)
0.57	1.617(1)	3.97(4)	1.966(2)	2.76(8)	2.089(17)	0.26(8)	3.02(2)
0.58	1.618(1)	4.12(3)	1.968(1)	2.72(4)	2.114(11)	0.23(3)	2.96(2)
0.638 (EDX)	1.618(2)	4.76(10)	1.968(3)	2.49(8)	2.116(32)	0.19(8)	2.68(3)
0.77	1.615(3)	3.77(19)	1.962(11)	2.49(45)	2.049(24)	0.59(46)	3.08(3)
0.78	1.617(2)	3.90(14)	1.969(5)	2.75(21)	2.072(27)	0.33(21)	3.07(2)
0.79	1.617(2)	4.12(12)	1.968(4)	2.69(18)	2.070(22)	0.35(18)	3.03(2)
0.80 (nominal)	1.619(2)	4.48(15)	1.966(5)	2.53(22)	2.062(19)	0.45(23)	2.99(2)
0.803 (EDX)	1.619(2)	4.57(13)	1.967(5)	2.55(19)	2.065(18)	0.42(19)	2.97(2)

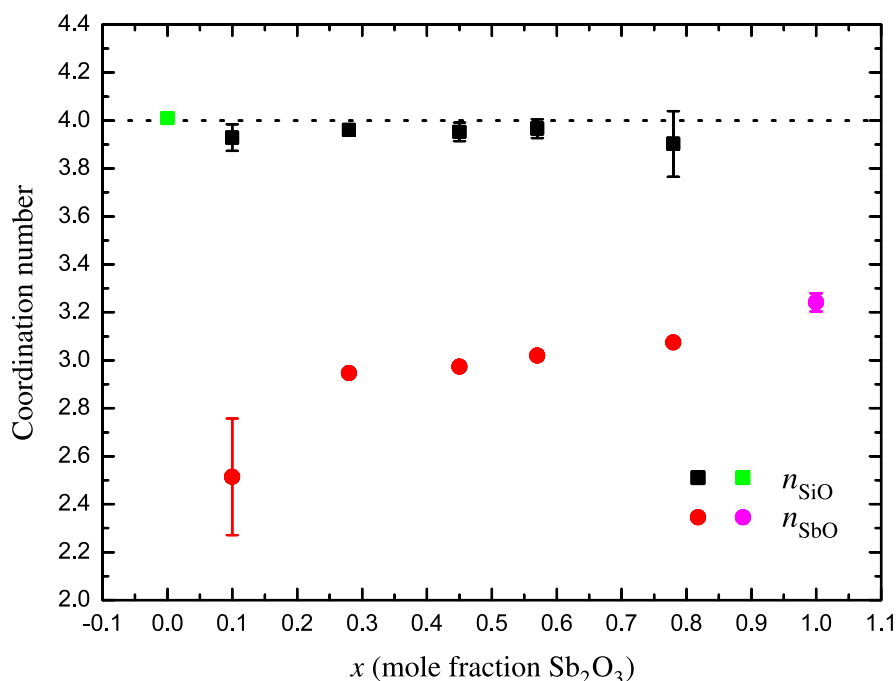


Figure 6-10 The total n_{SiO} and n_{SbO} obtained from the fits to the total correlation functions of the silicate glasses, using the x values obtained by trial-and-improvement. Also shown are coordination numbers from the Sb_2O_3 glass (*q.v.* §4.4.1) and an SiO_2 glass [11]. Where not apparent, error bars are smaller than the symbols plotted.

from the $\text{Sb}^{3+}\text{--O}$ peak of the $[\text{Sb}^{3+}\text{O}_3]$ trigonal pyramids (1.973 Å), so the coordination contribution from the octahedra (if present) cannot be determined. An alternative model might attribute the increased coordination to the presence of $[\text{Sb}^{3+}\text{O}_4]$ units, indicated by the second Sb–O peak at ~ 2.08 Å, the distance predicted by bond-valence calculations for four-coordinated Sb^{3+} —however, this does not then explain how the Sb^{5+} is incorporated in the glass structure ($[\text{Sb}^{5+}\text{O}_4]$ units are not possible, since four-coordinated Sb^{5+} should have a bond length of 1.859 Å, which is much too small).

There is a slight increase in the position of the first Sb–O peak with composition (Fig. 6-11), again tending towards that of the Sb_2O_3 glass (*q.v.* §4.4.1); it is unclear if a similar trend occurs in the position of the second peak due to the errors involved. The behaviour of the first peak is slightly different to that reported by Ellison and Sen [16], who observed that r_{SbO} remained fairly constant at 1.946(5) Å for $x < 0.7$, rising to 1.963(5) Å for $x \geq 0.7$; they also did not observe a distinct second Sb–O peak, although this may be due to limitations of the technique used (EXAFS).

The first two oxygen-oxygen correlations—arising from $\text{O}_{\text{Si}}\cdots\text{O}_{\text{Si}}$ at ~ 2.635 Å and

Table 6-5 The Sb–O coordination numbers measured from the neutron data (using ‘trial-and-improvement’ compositions) compared with two models based on the Sb^{5+} values obtained from Mössbauer spectroscopy (*q.v.* §6.1): one model assumes all Sb^{5+} present occurs in $[\text{Sb}^{5+}\text{O}_6]$ octahedra in a network of $[\text{Sb}^{3+}\text{O}_3]$ trigonal pyramids, the other is similar but posits $[\text{Sb}^{3+}\text{O}_4]$ pseudo-trigonal bipyramids to occur in equal ratio with the Sb^{5+} octahedra (as in crystalline Sb_2O_4).

x	n_{SbO}	n_{SbO} from Mössbauer Sb^{5+}	
		With $[\text{Sb}^{5+}\text{O}_6]$	With $[\text{Sb}^{5+}\text{O}_6]$ and $[\text{Sb}^{3+}\text{O}_4]$
0.10	2.51(24)	3.08(3)	3.10(4)
0.28	2.95(2)	3.13(3)	3.17(4)
0.45	2.97(2)	3.18(3)	3.24(4)
0.57	3.02(2)	3.21(3)	3.28(4)
0.78	3.07(2)	3.30(3)	3.40(4)

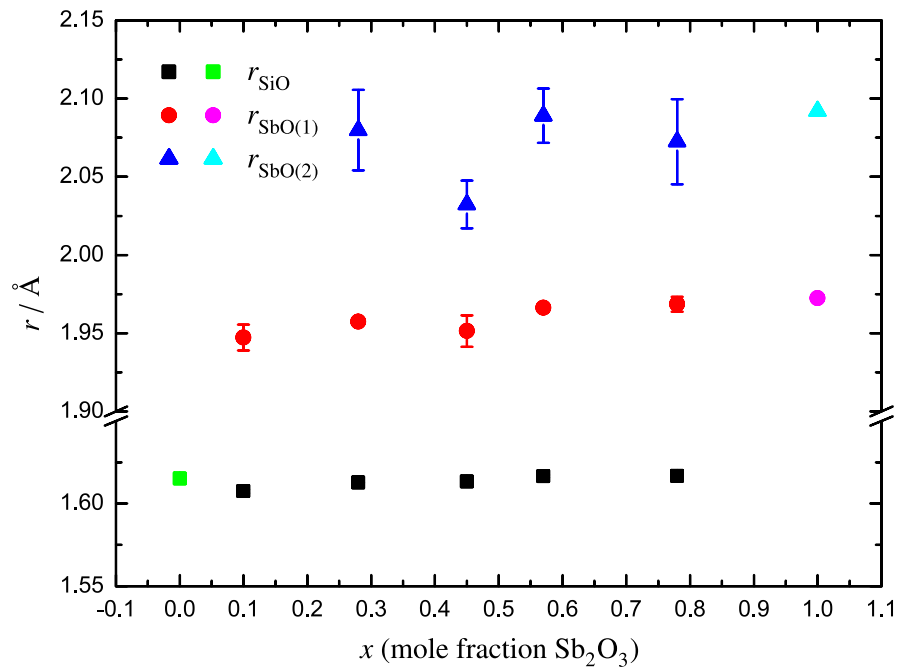


Figure 6-11 The positions of the peaks fitted to the total correlation functions of the silicate glasses, using the x values obtained by trial-and-improvement. Also shown are peak positions from an SiO_2 glass [11] and $\nu\text{-Sb}_2\text{O}_3$ (*q.v.* §4.4.1). Where not apparent, error bars are smaller than the symbols plotted.

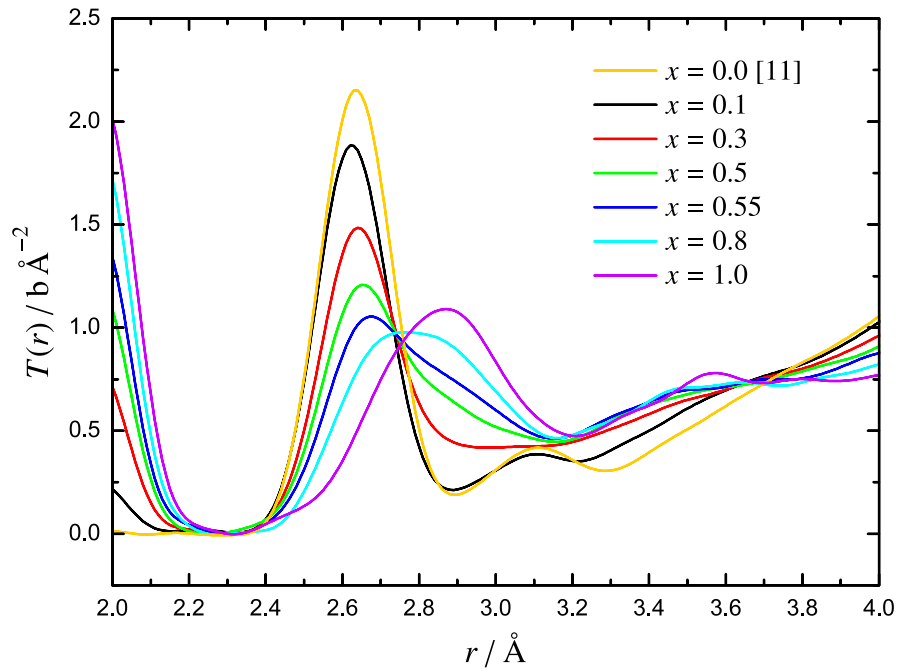


Figure 6-12 The total correlation functions of the silicate glasses, using the x values obtained by trial-and-improvement, showing the first $\text{O}_{\text{Si}}\cdots\text{O}_{\text{Si}}$ and $\text{O}_{\text{Sb}}\cdots\text{O}_{\text{Sb}}$ peaks (at ~ 2.635 Å and ~ 2.86 Å, respectively). Also shown are correlation functions from an SiO_2 glass [11] and $\nu\text{-Sb}_2\text{O}_3$ (*q.v.* §4.4.1), the latter processed with a lower Q_{max} of 35 Å $^{-1}$: this will result in wider peaks with reduced intensity compared to the other samples.

$\text{O}_{\text{Sb}}\cdots\text{O}_{\text{Sb}}$ at ~ 2.86 Å—overlap, and also cover the start of other correlations, such as the second $\text{Si}\cdots\text{O}$ and $\text{Sb}\cdots\text{O}$ peaks (Fig. 6-12); this makes peak-fitting difficult. However, there appears to be a smooth transition from the $\text{O}_{\text{Si}}\cdots\text{O}_{\text{Si}}$ distance in vitreous silica [11] to the $\text{O}_{\text{Sb}}\cdots\text{O}_{\text{Sb}}$ length found in the Sb_2O_3 glass; the $\text{O}_{\text{Si}}\cdots\text{O}_{\text{Si}}$ peak in the $x = 0.1$ sample is at a slightly smaller r than in $\nu\text{-SiO}_2$ but since r_{SiO} is also reduced, the O-Si-O angle is still the tetrahedral value of 109.5° . The O-Sb-O angle can be estimated from the Sb-O peak position and the apparent $\text{O}_{\text{Sb}}\cdots\text{O}_{\text{Sb}}$ distance of ~ 2.86 Å to be $\sim 93.7^\circ$, which is in good agreement with the average bond angle observed in the Sb_2O_3 glass (*q.v.* §4.4.1), whilst the continued broadness of the $\text{O}\cdots\text{O}$ peak for the $x = 0.8$ sample suggests that the large angular range of O-Sb-O previously observed in $\nu\text{-Sb}_2\text{O}_3$ (79.4° to 106.7°) is also present.

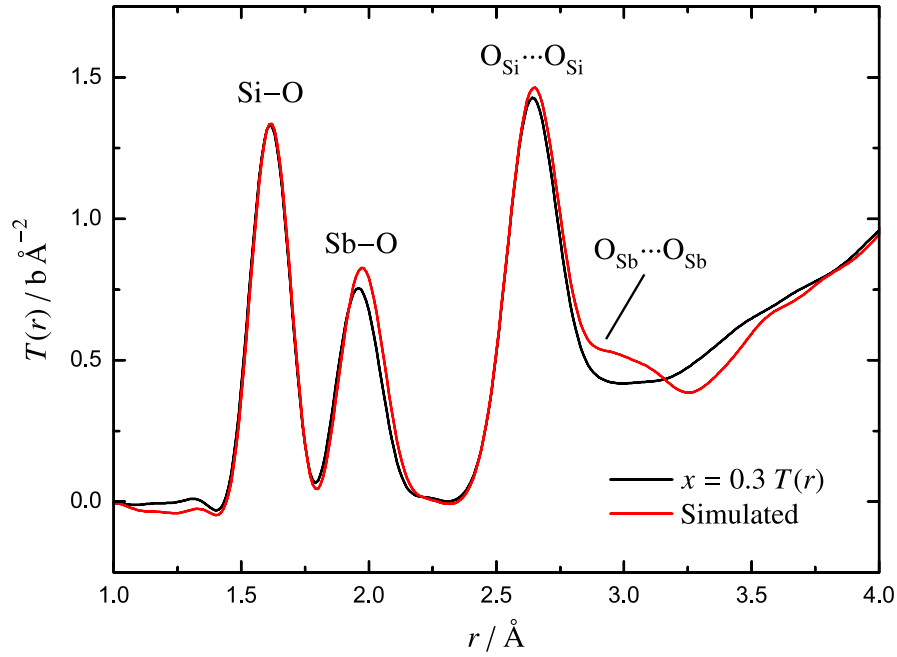


Figure 6-13 The $T(r)$ of the (nominal) $x = 0.3$ sample compared with one simulated by summing weighted ν -SiO₂ [11] and ν -Sb₂O₃ (*q.v.* §4.4.1) total correlation functions. All datasets were Fourier transformed at $Q_{\max} = 35 \text{ \AA}^{-1}$. Labels are the primary correlations giving rise to the peaks.

6.3.4 Simulating the total correlation function

Using the method previously employed for the antimony borate glasses (*q.v.* §5.4.4) a set of simulated total correlation functions for the antimony silicate glasses were generated from neutron diffraction data of ν -SiO₂ [11] and the Sb₂O₃ glass discussed earlier (*q.v.* §4.4.1). The comparison with the measured $T(r)$, analysed with the compositions obtained by ‘trial-and-improvement’, shows reasonable agreement (Fig. 6-13) but the simulation invariably overestimates the Sb–O correlation at greater r , suggesting that fewer of the more highly-coordinated antimony oxide units ([Sb³⁺O₄], [Sb⁵⁺O₆]) are present than in ν -Sb₂O₃. There is also a discrepancy in the region of the O_{Sb}...O_{Sb} correlation at $\sim 2.95 \text{ \AA}$, however this is probably due to the absence of correlations between the Sb₂O₃ and SiO₂ phases in the simulated $T(r)$ that should also be present at this distance. In general however, the close match between the two sets of correlation functions indicates that the two glass networks mix without much effect on each other, which agrees with the conclusions drawn earlier from the trend in T_g compared to binary germanosilicates (*q.v.* §6.1) and from the densities of the samples (*q.v.* §6.2).

6.3.5 Conclusions

Taken together, the trends in the Si–O, Sb–O and O···O correlations suggest that the antimony silicate glass structure incorporates the $[\text{SiO}_4]$ tetrahedra common to silicate glasses as well as the $[\text{SbO}_3]$ trigonal pyramids found in crystalline Sb_2O_3 . Higher-coordinated antimony oxide units are also present—as indicated by values of $n_{\text{SbO}} > 3.00$ —although whether these are $[\text{Sb}^{3+}\text{O}_4]$, similar to the 2+2 pseudo-trigonal bipyramids found in Sb_2O_4 , or $[\text{Sb}^{5+}\text{O}_6]$ octahedra, or some combination of the two, is unclear: the former is more in line with the coordination number measured, but does not explain the structural role of the Sb^{5+} measured by Mössbauer spectroscopy. Based on the relative invariance of the Sb–O bond lengths, it appears that the glass composition mainly affects the relative amounts of $[\text{SbO}_x]$ structural units present, without significantly influencing the internal geometry of the units themselves—in other words, both SiO_2 and Sb_2O_3 act as glass-formers in this system.

6.4 Summary

Five glasses in the $x\text{Sb}_2\text{O}_3 \cdot (1-x)\text{SiO}_2$ system were prepared and have been studied using various techniques, including laboratory X-ray diffraction, EDX analysis, Mössbauer spectroscopy, Raman spectroscopy, density measurements and neutron diffraction. EDX analysis indicated that the samples varied slightly from the nominal batch compositions, whilst XRD revealed that the sample with the highest SiO_2 content contained some α -quartz crystallites, probably present in an inseparable phase that was observed to form during glass-making. Mössbauer spectroscopy indicated a steadily increasing proportion of Sb^{5+} in the samples with increasing x , reaching 10 % of the antimony present in the glass at $x = 0.8$. Pycnometer measurements demonstrated that sample densities were as predicted by a linear increase in the molar volume with x from the density of SiO_2 glass to that of vitreous Sb_2O_3 , indicating that the two glass networks appear to mix without significantly affecting each other.

Analysis of the neutron diffraction data demonstrated that neither the nominal nor the EDX compositions were satisfactory for the majority of the samples, and so each dataset was re-processed using a range of x values to obtain the most probable composition (the primary criterion being an Si–O coordination number of ~ 3.95). This method,

which assumes that the SiO_2 in the system forms the standard $[\text{SiO}_4]$ tetrahedra found in other silicate glasses, produced Sb–O coordination numbers that rose with increasing x to a value of 3.07(2) when fitted with two peaks. This indicates the presence of $[\text{SbO}_x]$ units (where $x > 3$) in addition to the $[\text{SbO}_3]$ trigonal pyramids found in crystalline Sb_2O_3 , the most likely candidate being $[\text{Sb}^{3+}\text{O}_4]$ pseudo-trigonal bipyramids similar to those found in Sb_2O_4 . The role of the Sb^{5+} in the glass structure remains unclear, since n_{SbO} is too low for it all to form $[\text{Sb}^{5+}\text{O}_6]$ octahedra of the type found in Sb_2O_4 and Sb_2O_5 , and the proximity of the Sb–O peaks that would arise from $[\text{Sb}^{3+}\text{O}_3]$ and $[\text{Sb}^{5+}\text{O}_6]$ units preclude resolving the individual coordination contributions.

References

- [1] F. Machatschki, *Fortschr. Mineral.* **20**, (1936), 45–47.
- [2] Inorganic Crystal Structure Database, Chemical Database Service, Daresbury Laboratory (2009), <http://cds.dl.ac.uk/cds/cds.shtml>.
- [3] B. C. Davies, *Antimony Silicate Glasses: Structure and Phase Transitions* (2007), Final Year Project Report, University of Warwick.
- [4] M. Mee, *Antimony Silicate Glasses* (2007), Final Year Project Report, University of Warwick.
- [5] K. Nassau, R. A. Levy and D. L. Chadwick, *J. Electrochem. Soc.* **132** (2), (1985), 409–415.
- [6] L.-S. Du, L. Peng and J. F. Stebbins, *J. Non-Cryst. Solids* **353**, (2007), 2910–2918.
- [7] P. S. Gopalakrishnan and H. Manohar, *Cryst. Struct. Commun.* **4**, (1975), 203–206.
- [8] J. Amador, E. Gutiérrez Puebla, M. A. Monge, I. Rasines and C. Ruiz Valero, *Inorg. Chem.* **27** (8), (1988), 1367–1370.
- [9] A. Datta, A. K. Giri and D. Chakravorty, *J. Phys. Condens. Mat.* **4**, (1992), 1783–1790.
- [10] A. C. Hannon, *Nucl. Instrum. Meth. A* **551** (1), (2005), 88–107.
- [11] E. R. Barney, (personal communication) (2008).
- [12] N. E. Brese and M. O’Keeffe, *Acta Crystallogr. B* **47**, (1991), 192–197.
- [13] A. C. Hannon and J. M. Parker, *J. Non-Cryst. Solids* **274**, (2000), 102–109.
- [14] R. L. Mozzi and B. E. Warren, *J. Appl. Cryst.* **2**, (1969), 164–172.
- [15] A. C. Hannon, D. Di Martino, L. F. Santos and R. M. Almeida, *J. Phys. Chem. B* **111**, (2007), 3342–3354.
- [16] A. J. G. Ellison and S. Sen, *Phys. Rev. B* **67**.

Chapter 7

Conclusions and Future Work

7.1 Antimony oxide glass

The $T(r)$ of the antimony oxide glass, formed by roller-quenching molten Sb_2O_3 , exhibited two distinct Sb–O peaks at 1.972(1) Å and 2.092(4) Å, with coordination numbers of 2.99(2) and 0.25(2), respectively. The latter peak occurs at the distance predicted from bond-valence calculations for four-coordinated Sb^{3+} [1, 2]: if this entire peak is assigned to $[\text{Sb}^{3+}\text{O}_4]$ pseudo-trigonal bipyramids, then 6.3(5) % of the antimony present in the glass occurs in such units, and so the first Sb–O peak must arise from the remaining antimony. Since the antimony from the $[\text{SbO}_4]$ units is uncoordinated at $r_{\text{SbO}(1)}$, then some antimony oxide units with $n > 3$ must exist to compensate for the reduction, in order to attain the observed value of $n_{\text{SbO}(1)} \approx 3$ (if the first Sb–O peak arose entirely from $[\text{SbO}_3]$ trigonal pyramids, $n_{\text{SbO}(1)}$ would be ~ 2.81). The most likely candidate for these more highly-coordinated units are $[\text{Sb}^{5+}\text{O}_6]$ octahedra, which bond-valence indicates should have bond lengths of 2.009 Å, and that are found in crystalline Sb_2O_4 and Sb_2O_5 to have some slightly shorter bonds. To achieve the observed coordination number, 5.9(7) % of the antimony atoms in the glass would need to be Sb^{5+} . Given these proportions of Sb^{5+} and four-coordinated Sb^{3+} , the glass could be said to contain $\sim 12.4(4)$ mol% ‘ $v\text{-Sb}_2\text{O}_4$ ’.

From the measured peaks, two other structural models are also possible. For a system containing little or no Sb^{5+} , the presence of up to 27 % of the antimony in $[\text{Sb}^{3+}\text{O}_4]$ units with a 3+1 configuration—that is, three bonds at $r_{\text{SbO}(1)}$ and one longer bond at $r_{\text{SbO}(2)}$ —could account for the coordination numbers obtained from $T(r)$. $[\text{Sb}^{3+}\text{O}_4]$ units such as these are not found in the crystalline antimony oxides, but do occur in the Mayerová model of onoratoite [3]. The second model of the glass, allowing for greater quantities of Sb^{5+} , uses $[\text{Sb}^{5+}\text{O}_6]$ octahedra of the type found in crystalline Sb_2O_5 , which have a range of bond lengths. These would permit the Sb^{5+} to be three-

coordinated at $r_{\text{SbO}(1)}$ whilst the three remaining bonds at greater r would result in the second peak at $r_{\text{SbO}(2)}$. This model would account for up to 9 % of the antimony in the glass being Sb^{5+} , which appears to be the maximum amount consistent with the neutron data.

By comparison with the antimony oxychloride glass (see below), a model consisting of chains of $[\text{SbO}_3]$ trigonal pyramids interrupted by occasional $[\text{SbO}_4]$ units may be appropriate, with the $[\text{Sb}^{5+}\text{O}_6]$ octahedra (if present) paired with the $[\text{SbO}_4]$ pseudo-trigonal bipyramids, as in $c\text{-Sb}_2\text{O}_4$. Alternatively, a more disordered network of these units may also be possible, with the available data not serving to distinguish the two.

7.2 Antimony oxychloride glass

In the antimony oxychloride glass, prepared from crystalline onoratoite ($\text{Sb}_8\text{O}_{11}\text{Cl}_2$), all the antimony present was determined to be Sb^{3+} by Mössbauer spectroscopy. Therefore, based on the Sb–O distances observed in the $T(r)$ obtained from neutron diffraction, the principal network units are $[\text{SbO}_3]$ trigonal pyramids and $[\text{SbO}_4]$ pseudo-trigonal bipyramids, which is also the case in the crystalline material [3]. The exact arrangement of these units is unclear; two possible models—one based on the ‘ladder-like’ chains of antimony oxide units found in the Mayerová model of onoratoite [3] (possibly with some relaxation or breaking of bonds that might make the ‘ladders’ more chain-like), and the other of a more disordered antimony oxide structure with Sb–Cl distances closer to those predicted from bond-valence for three-coordination—do not appear to be distinguishable from each other using the available data.

7.3 Antimony borate glasses

The $x\text{Sb}_2\text{O}_3 \cdot (1-x)\text{B}_2\text{O}_3$ glass system, which was studied over the nominal compositional range of $x = 0.1$ to $x = 0.7$, appears to consist predominantly of $[\text{BO}_3]$ units that are largely arranged in boroxol rings (indicated by Raman spectroscopy, and as found in $\nu\text{-B}_2\text{O}_3$ [4–6]), with these being cleaved, at low x , by the introduction of $[\text{SbO}_3]$ trigonal pyramids homogeneously throughout the glass network. At higher x , there is evidence that some Sb–O–Sb links form, resulting in the persistence of $[\text{B}_3\text{O}_6]$ groups

to $x \geq 0.7$. The glass structure also contains some $[\text{BO}_4]$ tetrahedral units, up to a maximum $N_4 = 0.09(4)$ at $x = 0.5$, in agreement with the findings of previous authors [7–9]. Additionally, the Sb^{5+} found to be present in the glass by Mössbauer spectroscopy [9] probably occurs as $[\text{Sb}^{5+}\text{O}_6]$ octahedra (accommodating these units may be the reason for the formation of $\text{Sb}-\text{O}-\text{Sb}$ connections in the network at high x), whilst the position of a second, smaller $\text{Sb}-\text{O}$ peak in the glass $T(r)$ suggests that some $[\text{Sb}^{3+}\text{O}_4]$ pseudo-trigonal bipyramids also exist in the structure.

From an NMR study of $\text{GeO}_2-\text{B}_2\text{O}_3$ glasses, Baugher and Bray [10] showed that adding a glass-former to a borate network should not promote the formation of $[\text{BO}_4]$ units, and thus the increase in N_4 in the antimony borate glasses reported in the literature [7–9] should indicate that Sb_2O_3 does not act as a network former. However, the successful preparation of $\nu\text{-Sb}_2\text{O}_3$ described in this work would appear to indicate the opposite; a recent study of the tin borate glass system noted a similar dichotomy [11]. One possible explanation for this effect in the antimony borate system is that it is the influence of the Sb^{5+} on the network that causes $[\text{BO}_4]$ units to form, rather than the presence of the Sb_2O_3 .

7.4 Antimony silicate glasses

From the neutron diffraction of five $x\text{Sb}_2\text{O}_3 \cdot (1-x)\text{SiO}_2$ glasses of nominal compositions $x = 0.1$ to $x = 0.8$, it is apparent that the glass structure consists principally of $[\text{SiO}_4]$ tetrahedra and $[\text{SbO}_3]$ trigonal pyramids, with $n_{\text{SbO}} > 3.00$ indicating the presence of additional antimony oxide units with higher coordination. The amount of Sb^{5+} present in the glasses (as measured by Mössbauer spectroscopy) would suggest that these units are $[\text{Sb}^{5+}\text{O}_6]$ octahedra, although the coordination numbers obtained from neutron diffraction are too low for all of the Sb^{5+} to be accommodated in this fashion. Also, the occurrence of a second, smaller $\text{Sb}-\text{O}$ peak at slightly greater r than that of the $[\text{SbO}_3]$ units suggests that $[\text{Sb}^{3+}\text{O}_4]$ pseudo-trigonal bipyramids are also present, although these too would only add to the coordination number expected.

The densities measured for the samples are very similar to values calculated by assuming a linear increase in molar volume with x , from the density of $\nu\text{-SiO}_2$ to that of $\nu\text{-Sb}_2\text{O}_3$. This suggests that the two glass networks mix without significantly influenc-

ing each other, and this conclusion is further supported by a comparison of the neutron $T(r)$ with a simulated one obtained by summing weighted correlation functions from the two end-members of the system. This simulation did indicate however that the antimony silicates incorporate fewer high-coordination antimony oxide units ($[\text{Sb}^{3+}\text{O}_4]$, $[\text{Sb}^{5+}\text{O}_6]$) than the Sb_2O_3 glass. Thus, the exact nature of the antimony oxide structure in the silicate glass system remains somewhat unclear.

7.5 The behaviour of antimony oxide in a glass network

From the models described above for the various glass systems, the behaviour of Sb_2O_3 in a glass system can be quite clearly defined. In general, the oxide acts as conditional glass-former, where the presence of another glass-forming oxide or a modifier is necessary for glass-formation—however, the successful preparation of $v\text{-Sb}_2\text{O}_3$ by roller-quenching suggests that the oxide is in fact a glass-former, although it could be argued that there is still a modifying oxide present (the $\sim 12.4(4)$ mol% $v\text{-Sb}_2\text{O}_4$ indicated by one model). In any case, the structure of the antimony oxide network appears to be mostly unaffected by the presence and nature of a second glass-former: $[\text{SbO}_3]$ trigonal pyramids form the basis of the network, with any Sb^{5+} from oxidation of the melt forming Sb^{5+}O_6 octahedra. $[\text{Sb}^{3+}\text{O}_4]$ pseudo-trigonal bipyramids are also present, possibly in order to ease the accommodation of the octahedra (where these occur) into the network, and there is evidence from the antimony borate system that the presence of these more highly-coordinated units instigates a degree of heterogeneity in the binary network.

The relative invariance of the Sb–O and O...O peak-shapes between the glass systems studied in this work appears to indicate that the internal geometries of the various antimony oxide units appear to be unaffected by the glass composition—for example, the average O–Sb–O angle appears to be quite constant at 93.1° —although the proportions of each type of $[\text{SbO}_x]$ unit present can be affected, as is particularly noticeable in the oxychloride sample (Fig. 7-1). The connectivity of the antimony oxide units in the oxychloride glass is also distinctly different from that of the other systems studied, due to the absence of Sb^{5+} and the associated octahedra, resulting in a network of just $[\text{SbO}_3]$ and $[\text{SbO}_4]$ units. This may suggest that the presence of chlorine in the melt

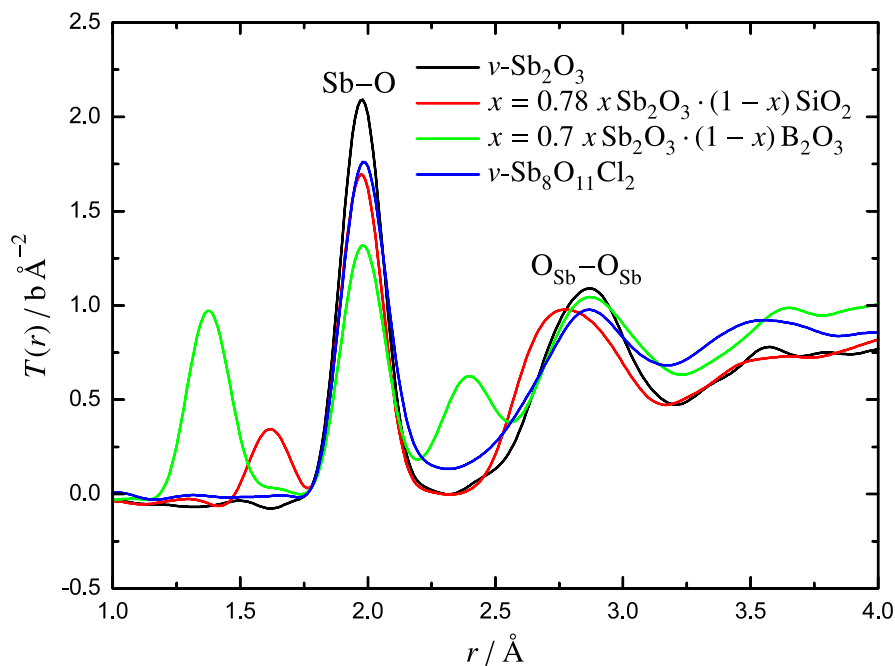


Figure 7-1 A comparison of the Sb–O and O_{Sb}...O_{Sb} peaks between the samples with the highest Sb₂O₃-content in the glass systems studied. All correlation functions were obtained using a Q_{\max} of 35 Å⁻¹.

somehow inhibits the oxidation of the antimony ions.

7.6 Future work

Due to time constraints, some measurements that might be useful in characterising the systems discussed in this work were not obtained, most notably Mössbauer spectroscopy of the ν -Sb₂O₃ sample. This would be useful to test the three models suggested for the glass, each of which indicates that a different amount of antimony is present as Sb⁵⁺ (*q.v.* §4.4.1, §7.1). If Sb⁵⁺ is present, then an attempt could be made to prepare ν -Sb₂O₃ by roller-quenching under reducing conditions, in order to determine whether or not a glass containing only Sb³⁺ can be formed. However, this might also cause Sb disproportionation, resulting in antimony metal being deposited on the crucible; the alternate approach, attempting to form a glass from Sb₂O₄ or Sb₂O₅ to see if the additional Sb⁵⁺ eases glass-forming, is impractical due to both oxides subliming instead of melting.

Another set of measurements that would be useful to obtain would be Raman spectra of the antimony silicate glasses: these should contain bands arising from the different

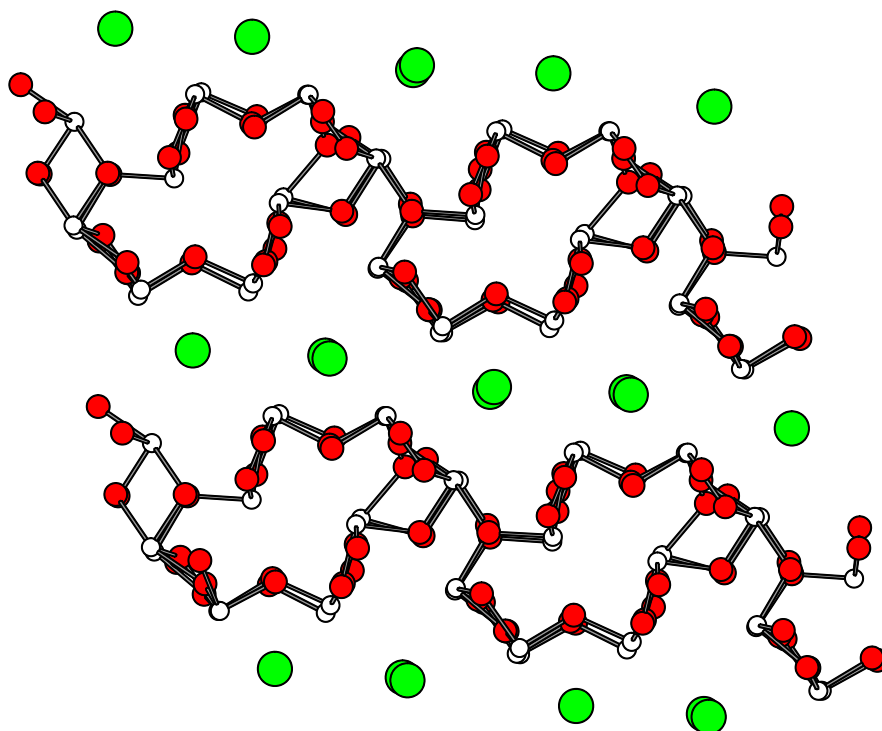


Figure 7-2 The Mayerová model of onoratoite ($\text{Sb}_8\text{O}_{11}\text{Cl}_2$). Oxygen atoms are lightly shaded, chlorine atoms are darker. The ‘tubes’ in each model are formed from four, edge-linked ‘ladders’ that extend into the page.

Q^n species [12], which will help to describe the connectivity of the SiO_2 network. ^{29}Si NMR would also provide complementary information on the Q^n groups, as demonstrated in the earlier studies of Davies [13] and Mee [14].

The data in this work indicated that the Mayerová model of onoratoite [3] is largely accurate (*q.v.* §4.4.2), but Rietveld refinement of the neutron diffraction data might still be useful to fine-tune the crystal structure, particularly with regard to the oxygen atoms, which are unlikely to be as clearly resolved in the previous X-ray study. Additionally, the chlorine coordinates in the crystallographic model (Fig. 7-2) may not be directly related to the actual atom positions: for example, the chlorine atoms may alternate randomly between being closer to one ‘plane’ of antimony oxide units or the other, or they may be so loosely bound that thermal oscillations (the study of Mayerová *et al.* [3] was conducted at 290(2) K) appear to give them an average position that is between the planes; a low-temperature neutron diffraction experiment could be used to detect the latter.

Reverse Monte Carlo (RMC) modelling could be applied to each of the neutron datasets obtained in this work to simulate the total structure factor $S(Q)$. Using a set of

Table 7-1 Neutron scattering lengths and atomic numbers for the elements present in the samples studied in this work. Where not listed as a specific isotope, the scattering length for the element at natural abundance is given.

Element or isotope	Neutron scattering length (fm)	Atomic number
¹¹ B	6.65	5
O	5.803	8
Si	4.1491	14
Cl	9.577	17
³⁷ Cl	3.08	
Sb	5.57	51

constraints that describe the basic structural units identified in the glasses, RMC could be used to generate a structural model that agrees quantitatively with the measured data. To achieve this, some refinements to the basic technique would be necessary to account for the steric effects of the antimony lone-pair, since atoms are typically modelled as being spherically symmetric. Information on the medium-range order of a glass system that could be extracted from an RMC model includes bond angle distributions, internal geometries of structural units (within the constraints applied to the model) and the degree of heterogeneity in the mixing of two glass-formers (e.g. Sb₂O₃ and SiO₂).

RMC modelling of the glass systems would benefit enormously from the addition of XRD data, since the different relative weightings of the atom-atom correlations (due to the scattering being proportional to atomic number, rather than scattering length) will produce a second structure factor with which the model must prove to be consistent. The total correlation functions obtained from the X-ray data would also be generally useful to characterise the antimony oxide units, due to the high atomic number of antimony compared to the other elements in the glasses (Table 7-1). A similar result, both for RMC modelling and analysis of $T(r)$, could be achieved for some samples by isotopic-enrichment: principally the antimony oxychloride glass, where the use of ³⁷Cl would significantly alter the weighting of the chlorine correlation functions obtained from neutron diffraction.

References

- [1] N. E. Brese and M. O’Keeffe, *Acta Crystallogr. B* **47**, (1991), 192–197.
- [2] A. C. Hannon and J. M. Parker, *J. Non-Cryst. Solids* **274**, (2000), 102–109.
- [3] Z. Mayerová, M. Johnsson and S. Lidin, *Solid State Sci.* **8**, (2006), 849–854.
- [4] R. L. Mozzi and B. E. Warren, *J. Appl. Cryst.* **3**, (1970), 251–257.
- [5] P. A. V. Johnson, A. C. Wright and R. N. Sinclair, *J. Non-Cryst. Solids* **50**, (1982), 281–311.
- [6] A. C. Hannon, D. I. Grimley, R. A. Hulme, A. C. Wright and R. N. Sinclair, *J. Non-Cryst. Solids* **177**, (1994), 299–316.
- [7] K. Terashima, T. Hashimoto, T. Uchino, S.-H. Kim and T. Yoko, *J. Ceram. Soc. Jpn.* **104** (11), (1996), 1008–1014.
- [8] R. E. Youngman, S. Sen, L. K. Cornelius and A. J. G. Ellison, *Phys. Chem. Glasses* **44** (2), (2003), 69–74.
- [9] D. Holland, A. C. Hannon, M. E. Smith, C. E. Johnson, M. F. Thomas and A. M. Beesley, *Solid State Nucl. Mag.* **26**, (2004), 172–179.
- [10] J. F. Baugher and P. J. Bray, *Phys. Chem. Glasses* **13** (2), (1972), 63–64.
- [11] A. C. Hannon, E. R. Barney and D. Holland, *Phys. Chem. Glasses* **50** (5), (2009), (in press).
- [12] P. McMillan, *Am. Mineral.* **69**, (1984), 622–644.
- [13] B. C. Davies, *Antimony Silicate Glasses: Structure and Phase Transitions* (2007), Final Year Project Report, University of Warwick.
- [14] M. Mee, *Antimony Silicate Glasses* (2007), Final Year Project Report, University of Warwick.